DEVELOPMENT AND MODELING OF A MINIATURE ELECTRO-HYDROSTATIC ACTUATOR FOR SMALL UAVS

TAN HAN RONG RONALD

(B.Eng.(Hons.).NUS)

A THESIS SUBMITTED

FOR THE DEGREE OF DOCTOR OF PHILOSOPHY

DEPARMENT OF MECHANICAL ENGINEERING

NATIONAL UNIVERSITY OF SINGAPORE

2015

DECLARATION

I hereby declare that the thesis is my original work and it has been written by me its entirety. I have duly acknowledged all the sources of information which have been used in this thesis.

This thesis has also not been submitted for any degree in any university previously.

Tan Han Rong Ronald

30 October 2015

ACKNOWLEDGEMENTS

I would like to acknowledge and thank the following:

- DSO National Laboratories for the financial support
- Superiors and colleagues at DSO National Laboratories for their support and encouragement
- A/Prof Gerard Leng for his advice, support and encouragement
- Management and staff at Chen Wee Precision Engineering Pte Ltd for their technical support
- Management and staff at Faulhaber Singapore for their technical support
- Family and friends for their love, encouragement and tolerance
- Last but not least, my wife for her love, support, encouragement and two beautiful children

TABLE OF CONTENTS

SUMMARY

This work developed a novel actuator to deflect the flight control surfaces of Unmanned Aerial Vehicles (UAVs). Demands on the performance and reliability of UAV actuators have grown along with the increasing importance of UAVs. There is thus a need for actuators that offer greater power density and multiple redundancies to increase operational life. Current state-of-the-art Electro-Mechanical Actuators (EMA) are not able to implement multiple redundancies without severely reducing their power density. While the implementation of multiple redundancies might address electrical failures, they actually increase the probability of mechanical failures in EMAs. Jamming between mechanical contacts within the EMAs can lead to catastrophic loss of the UAVs and there is still no means to mitigate such failures. Smart material actuators, which showed much promise in early development, were found to have inferior power density, while introducing new failure modes.

Miniature Electro-Hydrostatic Actuators (MEHA) offer a potential solution that will bring the high power density and ease of implementing multiple redundancies in hydraulic actuators from manned aircraft into UAVs. However, current miniature pump technologies have tight constraints on their allowable rotational speeds and maximum pressure, limiting the power density of MEHAs and making them uncompetitive against EMAs.

In this work, a novel MEHA concept was devised that combines the benefits of EMAs and EHAs. This concept is essentially a new class of actuator that is distinct from EMAs and hydraulic actuators. Like EMAs, it fits into the power-by-wire architecture of UAVs while offering the ease of implementing multiple redundancies and the ability to decouple the EMA from the control surface like hydraulic actuators. The analytical background and design process required to analyse and design the MEHA was developed in this work. A non-linear

dynamic model of the MEHA was also developed. Using the model, non-ideal effects were investigated and friction was identified as the most important factor affecting the MEHA's performance. The model was also used to study the MEHA's dynamic performance in both active-active and active-damped modes.

A prototype of the MEHA was fabricated and tested to determine its practical performance. It was shown to be able to deflect the design load to the required deflection angle, while possessing a high no-load speed. Testing of the prototype reveals that the alignment of the input pistons is a large contributor to the friction within the MEHA and highlights the importance of empirical testing to quantify friction. Both friction and leakage were quantified during tests. Tests of the MEHA prototype also showed that its step response agrees well with that predicted by the non-linear dynamic model.

The novel MEHA developed in this work offers a simple solution to increase the reliability of UAV actuators by allowing the implementation of multiple redundancies without severely sacrificing power density and dynamic performance. It is also a solution that mitigates the risk of mechanical jamming associated with EMAs, removing a source of catastrophic failure for UAVs. Beyond UAVs, the mitigation of mechanical jamming risk may increase the attractiveness of EMAs as a solution for 'more electric' manned aircraft. The tools and processes developed in the course of this work serve to ease the implementation of the MEHA, while insights gained in the process provide a base from which further development of the MEHA can progress.

LIST OF TABLES

LIST OF FIGURES

LIST OF NOTATIONS

A	Area of output piston, m^2
A_{ac}	Area of accumulator piston, m^2
A_{by}	Cross section area of bypass channel, m^2
A_p	Area of pump piston, m^2
A_{ip}	Area of input piston, m^2
A_o	Area of chamber port opening, m^2
AR	Aspect ratio
α	UAV Angle of Attack (AOA)
α_g	Gear pressure angle, radians
α_v	Volumetric coefficient of thermal expansion, 1/°C
B	Output shaft coefficient of viscous friction, $Nm/rad.s^{-1}$
B_0	Bulk modulus of hydraulic fluid, Pa
b	Gear width, m
b_v	Vane width, m
b_l	Breadth of lever arm, m
c	Speed of sound, m/s
C_{lossi}	Coefficient of leakage across pistons, m^3s^{-1}/Pa

c_{MAC}	Mean aerodynamic chord of length of flight control surface, m
$(C_N)_{surface}$	Normal force coefficient on flight control surface
δ	Flight control surface deflection, radians
Disp	Displacement of pump, m^3/rad
d_b	Pitch diameter of the gears on the ballscrew shaft
d_{by}	Diameter of bypass channel, m
d_c	Diameter of connecting channel, m
d_e	Pitch diameter of the gears on the electric motor shaft
d_p	Output piston diameter, m
d_{shaft}	Output shaft diameter, m
d_l	Hydraulic piston shaft diameter, m
d_i	Pitch diameter of the idler gears
$\varepsilon_{\gamma,e}$	Motor gear contact ratio
$\varepsilon_{\gamma,b}$	Ballscrew shaft gear contact ratio
σ_l	Stress in lever arm
σ_t	Gear tooth stress due to bending, Pa
E_m	Back EMF of electric motor, V
F	Output force of the control surface actuator, N

F_{max}	Maximum output force of the control surface actuator, N
F_b	Ballscrew output force, N
F_L	Force due to aerodynamic load, N
$F_{\Delta P,r}$	Force output from redundant hydraulic piston, N
F_{gear}	Force at gear contact, N
F_r	Force from redundant actuator, N
F_{rs}	Force from radial preload spring on AVP vane, N
F_o	Hydraulic piston output force, N
F_z	Axial force on AVP vane, N
f_{-3dB}	Bandwidth of flight control actuator, Hz
f_{bx}	Force acting through piston ball joint, N
f_d	Friction and viscous drag on piston, N
f_s	Spring force on piston, N
Gr	Gear train ratio
h_l	Height of lever arm, m
I	Load inertia, kg.m^2
I_a	Current supplied to electric motor, A
I_o	Output shaft inertia, kg.m^2

θ	Angle subtended by output piston line of action and lever arm, rad
θ_{1p}	Rotational position of driving gear, radians
θ_{2p}	Rotational position of driven gear, radians
θ_{m}	Electric motor rotor rotational position, radians
θ_{b}	Ballscrew shaft rotational position, radians
θ_{s}	Slope angle at a point within the transition segment, radians
J	Equivalent rotational inertia at motor of the output piston mass, kgm^2
J_{g}	Gear train total rotational inertia, kgm^2
J_{b}	Equivalent ballscrew shaft rotational inertia at motor, kgm^2
J_{bg}	Ballscrew shaft gear rotational inertia, kgm^2
J_{bg}	Ballscrew shaft rotational inertia, kgm^2
J_{i}	Idler gear rotational inertia, kgm^2
J_{ip}	Equivalent rotational inertia at motor of the input pistons mass, kgm^2
J_{m}	Electric motor rotational inertia, kgm^2
J_{load}	Load rotational inertia, kgm^2
J_{t}	Transmission rotational inertia, kgm^2
k_{ac}	Accumulator spring stiffness, Nm^{-1}
K_{aero}	Control surface hinge moment constant, Nm/rad

K_a	Gear application factor
K_B	Gear rim thickness factor
k_f	Coefficient of friction between the cam and vane
K_J	Gear geometry factor
K_m	Speed constant of electric motor, $rads^{-1}/V$
K_p	Flow resistance through port openings, $Pa/m.s^{-3}$
K_r	Flow resistance through bypass channel, $Pa/m.s^{-3}$
K_s	Gear size factor
K_t	Torque constant of electric motor, Nm/A
K_{ld}	Gear load distribution factor
K_m	Speed constant of electric motor, $V/rads^{-1}$
K_v	Gear dynamic factor
K_{vis}	Piston coefficient of viscous friction, $N/m.s^{-1}$
L	Ballscrew lead, $m/rads^{-1}$
l_l	Length of lever arm, m
la	Length of action on driving gear, m
l_b	Length of action on driven gear, m
l_{by}	Length of bypass channel, m

l_c	Length of connecting channel, m
l_s	Initial length of action of first gear teeth, m
l_2	Initial length of action of prior gear teeth, m
M	Mach number
m	Mass of output piston, kg
m_g	Module of gear, m
m_{nut}	Mass of ballscrew nut, kg
m_{ip}	Mass of input piston, kg
m_v	Mass of vanes, kg
N	Total reduction ratio
N_b	Number of teeth on ballscrew shaft gear
N_e	Number of teeth on motor shaft gear
N_i	Number of teeth on idler gear gear
$N_{surface}$	Normal force on a flight control surface, N
n	Efficiency of flight control actuator
P	Power, W
P_a	Pressure in accumulator circuit, Pa
P_A	Pressure in high (sign convention) pressure side of piston, Pa

P_B	Pressure in low (sign convention) pressure side of piston, Pa
$P_{A,ip}$	Pressure in high pressure side of piston at input piston bore, Pa
$P_{A,o}$	Pressure in high pressure side of piston at output piston bore, Pa
P_0	Pressure at which the hydrostatic chambers are filled, Pa
P_p	Pressure on piston, Pa
P	Pressure difference across input and output pistons, Pa
ΔP_{max}	Maximum pressure above the minimum accumulator pressure, Pa
ρ_1	Radial distance of meshing point from center of driving gear, m
ρ_2	Radial distance of meshing point from center of driven gear, m
ρ_a	Air density, kg/m^3
Q_A	Flow through port opening on high pressure (sign convention) side, m^3/s
Q_B	Flow through port opening on low pressure (sign convention) side, m^3/s
Q_{ac}	Net flow into accumulator circuit, m^3/s
Q_{el}	Leakage into accumulator circuit, m^3/Pa.s
Q_{il}	Leakage into across the output piston, m^3/Pa.s
Q_{max}	Maximum fluid flow rate, m^3/s
Q_p	Flow rate delivered by pump, m^3/s
Q_{ip}	Flow delivered by input piston, m^3/s

Q_{op}	Flow at the output piston, m^3/s
Q_{pr}	Flow rate through bypass channel, m^3/s
R_a	Electric motor resistance, Ω
r_1	Radius of driving gear, m
r_2	Radius of driven gear, m
r_{a1}	Outside radius of driving gear, m
r_{a2}	Outside radius of driven gear, m
r_{b1}	Root radius of driving gear, m
r_{b2}	Root radius of driven gear, m
r_{g1}	Pitch radius of driving gear, m
r_{g2}	Pitch radius of driven gear, m
r_{vcg}	Radial distance of vane center of mass from rotation center, m
$S_{surface}$	Area of flight control surface, m^2
s_a	Safety factor in accumulator spring compression
T	Hinge moment on flight control surface, Nm
T_1	Torque on driving gear, Nm
T_2	Torque on driven gear, Nm
T_b	Load torque on ballscrew, Nm

T_e	Torque output of electric motor, Nm
T_f	Friction torque in electric motor and ballscrew, Nm
T_{min}	Minimum operating temperature of the MEHA, °C
T_{max}	Maximum operating temperature of the MEHA, °C
T_0	Temperature at which hydrostatic chambers are filled, °C
τ	Mechanical time constant of electric motor, s
μ	Dynamic viscosity of the hydraulic fluid, Pa.s
V	Volume of hydraulic fluid in output piston bore, m^3
V_s	Voltage supplied to electric motor, V
V_{ip}	Volume of hydraulic fluid in input piston bores, m^3
V_{i1}	Control volume of driving gear at gear pump outlet, m^3
V_{i2}	Control volume of driven gear at gear pump outlet, m^3
V_0	Original volume of the hydraulic chamber, m^3
V_{o1}	Control volume of driving gear at gear meshing point, m^3
V_{o2}	Control volume of driven gear at gear meshing point, m^3
v	Output velocity of control surface actuator, m/s
v_b	Linear velocity of the ballscrew nut, m/s
v_{by}	Velocity of flow in bypass channel, m/s

v_r	Velocity of redundant actuator, m/s
w_p	Width of pump, m
ω_1	Rotational speed of driving gear, rad/s
ω_2	Rotational speed of driven gear, rad/s
ω_m	Rotational speed of electric motor, rad/s
x	Output piston position, m
x_{max}	Stroke length of output piston, m
$x_{a,max}$	Stroke length of accumulator piston, m
x_{a0}	Minimum compression of accumulator spring, m
x_{AC}	Location of aerodynamic center on flight control surface, m
x_{aci}	Initial position of accumulator piston, m
x_r	Position of redundant hydraulic piston, m
x_{HL}	Location of hinge line on flight control surface, m
x_p	Piston displacement, m
x_{ip}	Input piston displacement, m

1. INTRODUCTION

1.1 Background

The actuation of UAV flight control surfaces has long been dominated by Electro-Mechanical Actuators (EMA). As a result of their initial intended use as low-cost expendable replacements for manned aircraft, UAVs were not designed with the robust and complex hydraulic actuator systems commonly found on manned aircraft. Flight control actuation systems in manned aircraft such as the F/A-18 are designed to withstand two electrical failures and one hydraulic failure at the same point, with the third failure causing the actuator to go into fail-safe mode [1, 2]. It is common for control actuators in manned aircraft to feature quad-redundant electrical and command connections, triple-redundant hydraulic power generation systems and tandem hydraulic actuators [3, 4]. In contrast, UAV actuators typically consist of an electrical motor with mechanical transmission to the output at the control surface. Thus, from the early days of UAV development, the reliability and performance of UAV actuators have been an important issue. The RQ-5 Hunter UAV developed by the Israeli Aircraft Industries (IAI) in 1989 for the US Army was terminated during the low-rate production phase following numerous losses in flight testing due to control actuator failures [5].

In recent years, there has been a change in the design philosophy behind UAVs as they assumed more important roles and new roles have been enabled by the use of UAVs. In combat, while the pioneer generation of UAVs replaced manned aircraft in relatively simple roles such as artillery spotting, new generations of UAVs are being tasked with persistent long-range surveillance and in some cases, termination of elusive targets. Some of these

roles would have been impracticable with manned aircraft. The sophistication and cost of UAV payloads have increased with the many new roles that they now have to perform. These include advanced radio and satellite communications systems that enable long range operation with the operators half a world away, and high-tech radar and optical sensor systems that allow for long-range surveillance. It has also become increasingly common for UAVs to carry explosive ordnance. The point where UAVs are no longer considered expendable has long been passed. Current UAVs typically fly out of remote bases and operated over mostly uninhabited regions and since there are no pilots or passengers on board, accidents rarely draw public attention. However, greater demands on UAVs increasingly mean that they have to fly over heavily populated areas, where any crash is likely to result in damage and injuries. In particular, small UAVs with Maximum Take-off Weight (MTOW) of less than 150kg have to operate frequently in close proximity to urban areas, making their reliability more critical. Small systems such as the Boeing RQ-21A (Figure 1-1) and IAI Harop (Figure 1-2) are designed to loiter for long periods over areas of interest that will most certainly include densely populated cities, with the Harop carrying a 23kg warhead while the RQ-21A is designed to be recovered aboard navy ship decks crowded with munitions and fuel. There have even been suggestions that safety requirements for UAVs should in fact be more stringent than those for unmanned aircraft. As a result, the demands on actuator performance and reliability for small UAVs have increased.

Figure 1-1: Boeing Insitu RQ-21A recovered aboard a ship [6]

Figure 1-2: Launch of the IAI Harop [7]

EMAs have several fundamental flaws that hamper their ability to deliver on these greater demands. Due to the numerous mechanical contacts in EMAs, wear of mechanical components limit the operational life of EMAs and jamming of the mechanical transmission is a real concern [8, 9]. Introducing multiple redundancies to boost the reliability of electromechanical actuators require elaborate mechanisms and specialised controllers to

prevent force fight between the main and redundant electric motors [1, 10, 11]. In fact, while multiple redundancies may address electrical failure modes, they actually introduce more mechanical contacts in their elaborate mechanisms, increasing the probability of mechanical jamming which will in turn jam the entire control surface [8]. It is also difficult or impossible to implement more than two levels of redundancies with current EMA redundancy schemes. The addition of mechanisms to implement EMAs has a detrimental effect on their dynamic performance due to the increase in inertia that the electric motors have to drive. The inability to decouple failed or dormant electric motors from the entire mechanical transmission means that they act as a load on the active motor, reducing the dynamic performance of the entire EMA. Despite attempts at introducing EMAs as actuators for control surfaces on manned aircraft [1], the probability of jamming, in addition to lower power density have prevented their widespread adoption as actuators for aircraft control surfaces.

Smart materials were once touted as a new generation of UAV actuators that promised improved reliability and compactness by embedment into flight control surfaces [12]. However, issues such as brittleness of the piezoelectric material and dielectric breakdown in humid environments have impacted their reliability [13], while the need for supporting structures and amplification mechanisms makes their power density inferior [14, 15, 16]. In the case of Shape Memory Alloys, they are simply unable to provide the dynamic performance required in UAV actuators [12].

Hydraulic actuators, with centralised power generation and long hydraulic lines, have long been employed in actuating manned aircraft control surfaces due to their high power densities and ease in implementation of multiple redundancies. In contrast to EMAs, the

output of hydraulic actuators can be decoupled from the pump and motor with a simple bypass valve to allow other hydraulic actuators to continue actuating the control surface. However, traditional hydraulic actuators require extensive hydraulic systems that do not fit well into the 'power-by-wire' architecture of small UAVs. Electro-Hydrostatic Actuators (EHA) are a relatively new evolution of hydraulic actuators at the forefront of implementing 'power-by-wire' architecture on manned aircraft such as the F-35 (Figure 1-3) that is only just about to enter service. It uses electric motors to generate hydraulic power closer to the control surfaces, thereby doing away with long hydraulic lines for a more compact solution while retaining many benefits of traditional hydraulic actuators [17, 18]. Large UAVs may well employ the same EHAs used in manned aircraft to meet more stringent reliability and safety requirements but for UAVs with MTOW of less than 150kg, existing EHAs are simply too bulky. Miniature Electro-Hydrostatic Actuators (MEHA) may offer a solution that can meet these increased demands in small UAV actuators. However, at the relatively low levels of power typically required for actuating UAV control surfaces, MEHAs tend to have lower power density than electromechanical actuators [19]. This can be attributed to the bulkiness of hydraulic equipment such as valves, manifolds and accumulators as well as the higher leakage rates and lower pressure rating in miniature hydraulic components. Coupled with the low pressure and input rotational speed limits of current miniature pumps, MEHAs with current miniature pump technologies are uncompetitive against EMAs in the power levels required for UAVs.

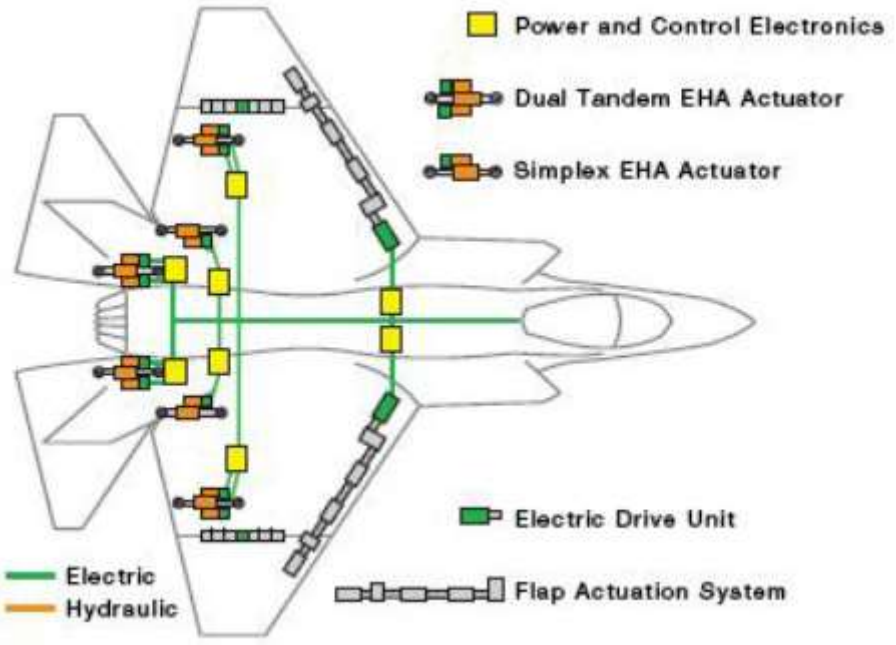

Figure 1-3: Lockheed Martin F-35 EHA flight control system [4]

This work explores and develops a novel Miniature Electro-Hydrostatic Actuator (MEHA) that is distinct from conventional EHAs. It combines the high power density of EMAs at the relatively low power levels required by UAVs with the ability of EHAs to decouple the actuator output from the electric motor in case of mechanical jamming and to transmit power efficiently. It also retains the compatibility of EMAs with the 'power-by-wire' architecture of UAVs and the ability of EHAs to fail to a damped mode so that parallel MEHAs can continue actuating the aircraft's control surfaces. As a result of the MEHA's unique integration of electromechanical and hydraulic power systems, parametric studies are needed to optimise the overall actuator as well as the individual power stages in order to meet realistic dynamic performance requirements while maximising power density. Simulation models are required to aid the optimisation studies for the overall actuator as well as to study the effects of non-linearities such as friction, flow restriction and leakage on its dynamic performance. The performance of the MEHA in 'active-active' mode with parallel MEHAs operational and in 'active-damped' mode where a parallel MEHA has failed

also has to be studied with these models. To study the impact of the MEHA's design parameters and to generate the input data for the simulation models, experimental investigations of the MEHA's components and theoretical analyses are needed. The models, parametric studies, analyses and experimental data will aid the design of the MEHA for any future application. Theoretical analyses of the MEHA's sub-components are also needed to determine that the structural loads expected on these components are within safe limits for a realistic prototype. Prototyping of the MEHA is needed to prove the concept and validate the simulation models and theoretical analyses.

This work has been reported in a DSO National Laboratories report titled 'INP report: Design and analysis of the Miniature Electro-Hydrostatic Actuator (MEHA)'.

1.2 Objectives

The main aim of this study is to develop a novel Miniature Electro-Hydrostatic Actuator (MEHA) for small UAV applications that enables the decoupling of an EMA from the output in the event of a failure or while in dormant mode, and that is able to transmit power efficiently to the output. The MEHA should have better power density and dynamic performance over the current state-of-the-art dual redundant EMAs for UAVs. The specific objectives of this work are to:

- Conceptualise the MEHA to allow for the decoupling of the EMA from the output using a closed hydrostatic circuit
- Develop the analytical equations for the design and analysis of the MEHA
- Study the interactions between the individual power stages and optimise the overall MEHA as well as the different power stages for dynamic performance and power density by developing simulation models and conducting parametric studies

- Investigate the flow restriction within the channels of the MEHA's closed hydrostatic circuit and the flow through the bypass of a MEHA in damped mode for different MEHA design parameters with numerical methods
- Develop models for the numerical parametric investigation of the MEHA to predict the effects of friction, flow restriction, damping and leakage on its dynamic performance
- Design, analyse and fabricate a prototype of the MEHA to obtain experimental data for friction and leakage, and to validate the theoretical analyses and simulation models

1.3 Scope of study

This research is focused on the study and development of a novel Miniature Electro Hydrostatic Actuator (MEHA) for application in small UAVs with Maximum Take-Off Weight (MTOW) of less than 150kg and length of less than 2.5m.

It is assumed in this work that a power-by-wire flight control system architecture is employed in UAVs (as is generally true) and that electric motors are used to generate mechanical power. This research will not delve into the specifics of motor design.

1.4 Thesis outline

This dissertation consists of six chapters, which are organised in the following manner.

Chapter 1 introduces the background and motivation of this study. It also states the study's objectives and scope, in addition to outlining the organisation of the thesis.

Chapter 2 reviews the fundamentals and current state-of-the-art in UAV actuators. It will also establish the benchmarks that will be used for comparison with the MEHA. The current

state-of-the-art in hydraulic pumps for EHAs and their limitations in miniaturisation will also be studied.

Chapter 3 describes the MEHA concept in detail before developing the theoretical background of the MEHA. It also details the development of the simulation models to be used in the study of the MEHA.

Chapter 4 presents the design and fabrication of the MEHA prototype. It details the parametric study of the MEHA's design parameters and the optimisation of the overall MEHA as well as of its individual power stages.

Chapter 5 reports on the analysis of the MEHA prototype for this work. The structural analysis of the prototypes components is first reported. This is followed by investigations on the flows in the closed hydrostatic circuit's channels and through the bypass with numerical analysis. The simulation of the MEHA prototype with non-linear effects and its predicted step response are next reported. Lastly, an analysis of the accuracy and stiffness of the prototype is conducted.

Chapter 6 presents the experimental results obtained from testing of the MEHA prototype. The experimental setups to characterise and study the prototype are also described.

Chapter 7 concludes the study and recommends areas for further work.

2. BACKGROUND

In this chapter, the fundamental background in UAV actuators is first reviewed. Electro-Mechanical Actuators (EMA) are then evaluated in terms of their performance and reliability, and benchmarks used for comparison in this study are established. Smart material actuators are also evaluated. The fundamentals of Electro-Hydrostatic Actuators (EHA) are studied to understand the benefits it offers manned aircraft and how it relates to UAVs. Different types of miniature hydraulic pump technologies are then evaluated to understand their limitations in being able to realise Miniature Electro-Hydrostatic Actuators (MEHA) as UAV actuators.

2.1 UAV control surface actuators

In this sub-section, the characteristics of the load on UAV control surfaces and that of actuators that use electric motors to generate mechanical power are reviewed.

UAV actuators deflect the control surfaces against aerodynamic forces to control the attitude of the UAV. Aerodynamic loads on a deflected control surface are a function of both the UAV's Angle of Attack (AOA) and the deflection of the control surface. A full database of these loads and the resultant hinge moments at different AOA and surface deflection are usually predicted by Computational Fluid Dynamic (CFD) simulation. However, for ease of simulation, this work assumes that the AOA is negligibly small and that the hinge moment is simply a linear function of its deflection angle. This assumption was similarly used in previous work [20, 21]. A method for estimating aerodynamic loads by [22] is detailed in the following.

Depending on the Mach number, M and the aspect ratio of the control surface, AR, the normal force coefficient on the surface, $(C_N)_{surface}$ at the UAV's Angle of Attack (AOA), α and the deflection of the control surface, δ is found for $M^2 > 1 + \left(\frac{8}{\pi AR}\right)^2$,

$$|(C_N)_{surface}| = \left[\frac{4|\sin(\delta+\alpha)\cos(\delta+\alpha)|}{\sqrt{M^2-1}} + 2\sin^2(\delta+\alpha)\right] \quad 2\text{-}1$$

For $M^2 < 1 + \left(\frac{8}{\pi AR}\right)^2$,

$$|(C_N)_{surface}| = \left[\left(\frac{\pi.AR}{2}\right)|\sin(\delta+\alpha)\cos(\delta+\alpha)| + 2\sin^2(\delta+\alpha)\right] \quad 2\text{-}2$$

The normal force on a surface can then be computed from the area of the control surface, $S_{surface}$ and the air density, ρ_a by

$$N_{surface} = \frac{1}{2}\rho_a (Mc)^2 S_{surface} (C_N)_{surface} \quad 2\text{-}3$$

The location of the aerodynamic center, x_{AC} on the control surface at subsonic speeds is at the quarter mark of the mean aerodynamic chord from the leading edge, c_{MAC}

$$x_{AC} = 0.25 c_{MAC} \quad 2\text{-}4$$

At supersonic speed, x_{AC} varies with the Mach number and the aspect ratio of the control surface

$$x_{AC} = \frac{AR[M^2-1]^{\frac{1}{2}} - 0.67}{2AR[M^2-1]^{\frac{1}{2}} - 1} \quad 2\text{-}5$$

The hinge moment on a control surface, T is then found by

$$T = N_{surface}(x_{AC} - x_{HL}) \quad 2\text{-}6$$

The equations can be implemented easily in a program and the hinge moment can then be modelled as being linearly proportional to surface deflection with a constant torque slope, $\mathrm{K_{aero}}$ as seen in Figure 2-1 for different UAV speeds where

$$\mathrm{K_{aero}} = \frac{\mathrm{T_{max}}}{\delta_{\mathrm{max}}} \qquad 2\text{-}7$$

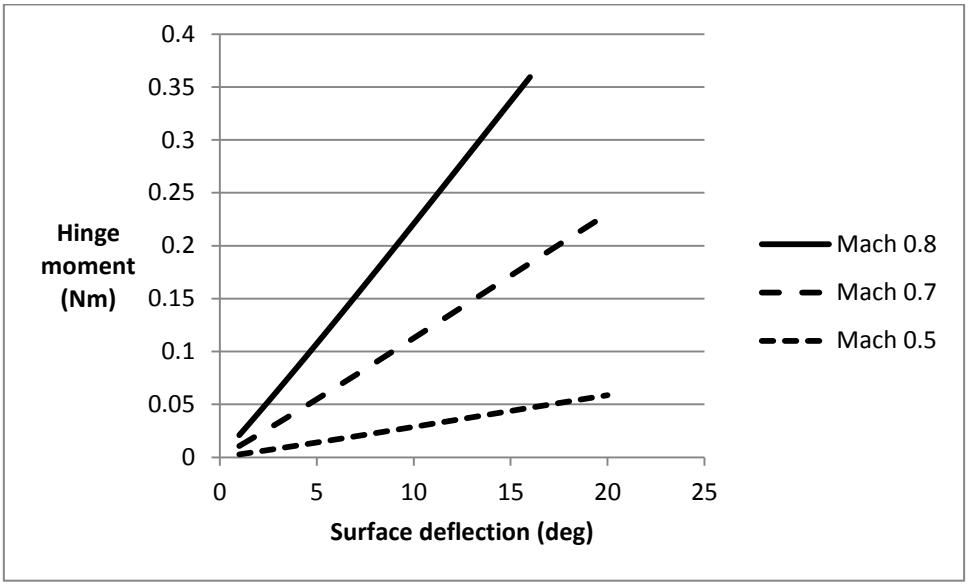

Figure 2-1: Hinge moment as a function of surface deflection at different air speeds at 0° AOA

Regardless of the machine in which the actuator is employed or the transmission that the actuator uses, the power transmitted across the transmission, P is constant, attenuated only by losses across the transmission accounted for by the efficiency term, n

$$\mathrm{P} = \mathrm{T}\dot{\delta} = n\mathrm{T_e}\omega_{\mathrm{m}} \qquad 2\text{-}8$$

Across the transmission, the torque at the input, $\mathrm{T_e}$ is increased to meet the load required at the actuator output, T, while speed at the input, ω_{m} is decreased to the speed at the output, $\dot{\delta}$. In the power-by-wire flight control system architecture typically found on UAVs, the power to actuate flight control surfaces is usually generated by electric motors near the

control surface. Electric motors are fundamentally a form of transmission that converts voltage, V_s and current, I_a at the power supply into torque, T_e and speed, ω_m at the motor

$$P = T_e \omega_m = V_s I_a \quad 2\text{-}9$$

Torque at the motor is related to the current input by the motor constant, K_t by

$$T_e = K_t I_a \quad 2\text{-}10$$

The relationship between the torque and rotational speed of an electric motor is typically linear. Along a constant gradient line joining the maximum stall torque and maximum no-load speed, the peak power output of the motor is at the point where its torque output is half of stall torque and where it is rotating a half the no-load speed. Thus, the peak power output of an electric motor is given by a quarter of the product of the no-load speed and stall torque.

Beside the power output, the dynamic performance is important for any UAV actuator. A UAV is essentially a closed loop control system (Figure 2-2) and its control surface actuators are the means by which its flight motion is controlled. In turn, the actuators are inner closed loop control systems which act to deflect the UAV's control surfaces to the commanded deflections. The frequency at which the gain of an open loop system is unity is also where the closed loop gain is 0.707 or -3dB and phase shifted by -45°. Defined as the bandwidth of the closed loop system, the gain of the closed loop will tend towards the open loop gain beyond this frequency. Knowing the bandwidth of the closed loop system will predict its response to a step input [23]. For most aircraft, control bandwidth is less than 1.6Hz [24, 25]. In order to avoid significant phase lag in the aircraft control loop, the actuator control loop bandwidth will have to be 5-10 times the aircraft's control bandwidth [26]. As most

UAVs are of a scale smaller than manned aircraft, their flight control and actuator bandwidths will have to be greater [27]. Bandwidth requirements established by researchers at Northrop Grumman Corporation (NGC) for a 30% scale model of a representative next-generation UAV have been reproduced in Table 2-1.

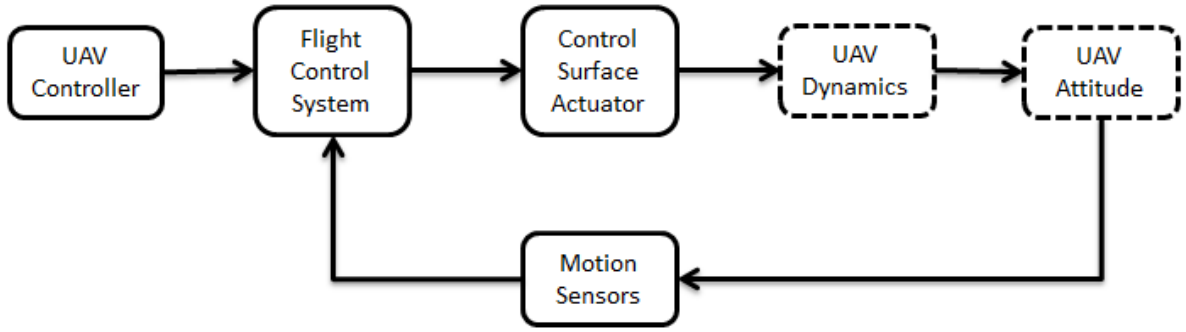

Figure 2-2: Block diagram of UAV attitude control loop

Table 2-1: Northrop Grumman Corporation (NGC) 30% scale UAV requirements [14]

Control surface deflection case	Requirement
Full deflection	±20° at 3Hz
Torque slope (outboard control surface)	0.17Nm/°

The bandwidth, f_{-3dB} of actuators that use electric motors to generate mechanical power is related to the mechanical time constant of the motor τ by

$$f_{-3dB} = \frac{1}{2\pi\tau} \qquad 2\text{-}11$$

The mechanical time constant is dependent on the motor's inertia, $\mathrm{J_m}$ and load inertia, $\mathrm{J_{load}}$ as seen at the motor through the leverage, N, of the actuator, in addition to the motor's resistance, $\mathrm{R_a}$ and constants $\mathrm{K_t}$ and $\mathrm{K_e}$.

$$\tau = \frac{\mathrm{R_a}\left(\mathrm{J_m}+\mathrm{J_t}+\mathrm{J_{load}}/\mathrm{N}^2\right)}{\mathrm{K_t K_m}} \qquad 2\text{-}12$$

With a large leverage between the actuator output and input, the load inertia as seen at the motor is negligible. Thus, given the same motor design parameters, the inertia of the

mechanical transmission has to be limited to achieve a minimum mechanical time constant and meet the bandwidth requirement of the actuator.

2.2 Electomechanical actuators

Electro-Mechanical Actuators (EMA) are the primary actuators used in the current state-of-the-art UAV flight control systems, thus it is appropriate to review and benchmark against this technology.

Gears are a mechanically simple method to transmit mechanical power. A gear with smaller diameter is directly attached to the electric motor to drive a larger diameter gear. Since the force, $\mathrm{F_{gear}}$ and velocity at where the gear teeth engage are the same, the torque, $\mathrm{T_1}$ on the smaller gear with radius, $\mathrm{r_1}$ is lower than the torque, $\mathrm{T_2}$ on the bigger gear with larger radius $\mathrm{r_2}$, while the rotational speed of the bigger gear, ω_2 is lower than that of the smaller gear, ω_1.

$$\mathrm{F_{gear}} = \frac{\mathrm{T_1}}{\mathrm{r_1}} = \frac{\mathrm{T_2}}{\mathrm{r_2}} \tag{2-13}$$

$$\mathrm{T_2} = \frac{\mathrm{r_2}}{\mathrm{r_1}}\mathrm{T_1} \tag{2-14}$$

$$\mathrm{T_1}\omega_1 = \mathrm{T_2}\omega_2 \tag{2-15}$$

A simple dual redundant EMA can be realised by having two motors each with a spur gear drive a common larger diameter gear. At any one time, only one motor can drive the common output gear, unless there is a high level controller synchronising both motors to rotate at exactly the same speed to prevent force-fight between them. If one of the motor is rotating at a slightly higher speed, the high stiffness of the gear teeth will lead to it driving the other slightly slower motor. A high level controller is also required to detect if the active

motor has failed so that the backup dormant motor can be activated [10]. While this redundancy scheme will be able to withstand the electrical failure of one of the motor and continue operating with the other motor, any mechanical jamming within the spur gear train or motor rotors will lead to the complete loss of the actuator.

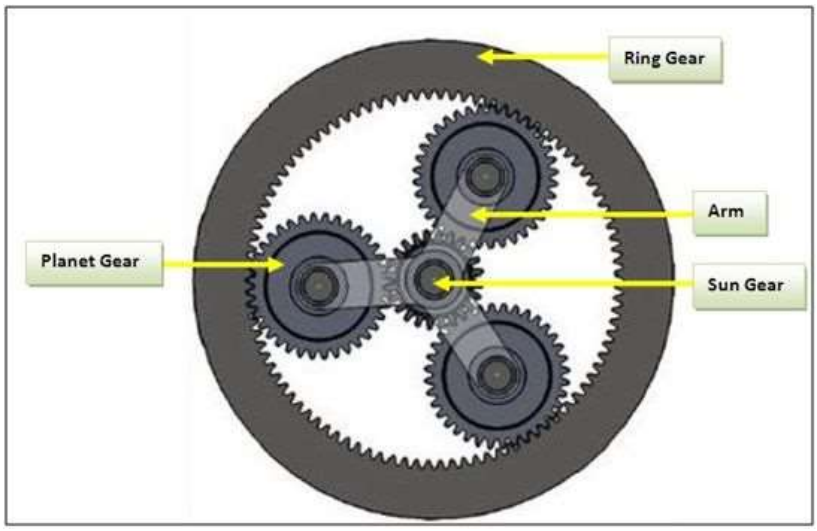

Figure 2-3: Planetary gear schematic [28]

Like spur gears, planetary gears (Figure 2-3) rely on contact between gear teeth to transmit mechanical power from the electric motor to the output and the different diameters of the gears provide the mechanical leverage. Planetary gears offer high leverage at high efficiency [29]. The unique geometry of planetary gears makes it attractive for implementing dual redundant EMAs [1, 30]. One of the motors drives the ring gear with internal teeth, while the other drives the sun gear. Both motors can be operated together in an 'active-active' 'velocity-summing' scheme to transmit power to the output during normal operation through the planet gears and the connecting arm but this will require the controller to actively monitor the current difference between motors to prevent force fight between them [31]. The use of planetary gears in the 'velocity-summing' scheme is well-established in the field of hybrid vehicle transmission [32]. In the event that one of the motor experiences a mechanical jam, the other motor can continue operating the actuator.

However, in the event an electrical failure or if the mechanical failure does not completely jam the faulty motor, the active motor will have to drive both the output and the faulty motor through the planetary gear. As a result, brakes on each motor and a fault detection controller are required to ensure that the faulty motor will be stopped fully in order for the remaining motor to continue operating [33]. The need for a gear train and brakes reduces the power density of such electromechanical actuators in addition to increasing the inertia seen at the driving motors, thereby reduce their dynamic performance.

Ballscrews are another commonly used mechanical transmission in UAV actuators. It consists of a precision-machined screw shaft and nut that has small steel balls between them. Rotation of the shaft translates into linear motion of the nut as the balls are rotated by the thread of the shaft against the helical raceway of the nut. A return path within the nut allows the balls to circulate within the raceway. The force, F generated by the ballscrew can be converted from torque at the shaft by the following formulas

$$\mathrm{T_e} = \frac{\mathrm{FL}}{2\pi n} \tag{2-16}$$

$$\mathrm{v} = \mathrm{L}\omega_\mathrm{m} \tag{2-17}$$

The force generated at the nut is usually converted to torque at the UAV control surface by a fork. Efficiency of the ballscrew, *n*, is high because contact between the nut and the shaft is through the balls. The lead of the ballscrew, L, is defined as the linear distance that the nut travels per revolution of the screw shaft, and it defines the amount of torque and rotational speed required at the electric motor for a given load requirement.

Ballscrews have also been used in dual redundant EMAs [11] in a 'force-summing' scheme. Similarly, the controller must actively monitor the motors to prevent force fight between

both parallel actuators. In the event of the failure of one of the motors, the remaining motor has to drive the actuator load and the inertia of the failed motor. Ballscrews are also used in dual redundancy schemes where there is a redundant motor winding to provide only dual electrical redundancy [34]. For some dual redundant EMAs utilising planetary gears, the carrier arm is connected to the ballscrew to convert the rotation motion into linear motion that is more compatible with linkages of control surfaces. In all cases, the ballscrew itself is a single point of mechanical failure, which will cause the loss of the entire actuator.

While these different dual redundancy schemes for EMAs are able to withstand electrical faults, the entire actuator and control surface will be jammed in the event that any part of the gear train is stuck. This catastrophic failure mode will lead to the loss of the aircraft and is one of the main reasons EMAs have not been adopted in manned aircraft [8, 9, 17, 35]. Even in the ideal situation where a UAV's design allows for multiple control surfaces controlling the same axis, the possibility that the EMA can be jammed in a particular deflection angle will still likely lead to catastrophic loss of the aircraft. Clutches can be installed to decouple the failed parts of the transmission but it will be tremendously bulky and heavy, making such a solution unsuitable for UAV actuators. If clutches and brakes are installed, the probability of their failure also has to be taken into account [33].

In order to meet the torque slope requirement in Table 2-1, a commercially available dual redundant electromechanical UAV servo actuator detailed in Table 2-2 was selected. However, it should be noted that this actuator is meant for the current generation of low-speed 450kg-class UAVs with lower dynamic performance requirements such as the Elbit Hermes 450 (Figure 2-4), hence the bandwidth of this actuator is insufficient to meet the representative requirements established in Table 2-1. Furthermore, the NGC 30%-scale UAV

is smaller with an overall length of 2.5m and wingspan of 2.8m compared to a length of 6.1 meter and a wingspan of 10.5m for the Hermes 450. This reflects the higher operating speed and dynamic pressure acting on the control surfaces of the NGC UAV. The torque slope of 0.17Nm/° for the 30% scale NGC UAV is based on it operating at a dynamic pressure of 180 lb/ft^2 or 8618.4 Pa [14]. From Equation 2-3, this is the dynamic pressure acting on the control surface while it is operating at M0.35 at sea level ($\rho_a = 1.225\ \mathrm{kg/m^3}$, $c = 340.29\ \mathrm{m/s}$) or M0.5 at 18000ft ($\rho_a = 0.698\ \mathrm{kg/m^3}$, $c = 318.5\ \mathrm{m/s}$). This is much higher than the maximum speed of 49 m/s for the Hermes 450 and as a result, a larger actuator normally used for larger UAVs has to be employed.

Figure 2-4: Elbit Hermes 450 UAV [36]

Table 2-2: Dual redundant electromechanical actuator benchmark [37]

	ERSA-0311	
Continuous load	4Nm	
Maximum torque	25Nm	
No load speed	160°/s	
Nominal load	Inertia	0.0015kgm^2
	Torque slope	0.2 Nm/°
	Bandwidth	3Hz ±4°
Stiffness	1.2°	
Useful stroke	±45°	
Positioning accuracy	±0.6°	
Operating temperature	-40 – 71°C	
Weight	0.875kg	
Nominal operating voltage range	24-32V	
Maximum current	4.5A	

2.3 Smart material actuators

In the quest for greater reliability and performance in UAV actuators, much work has been expended on a class of actuators collectively referred to as 'smart material' actuators. These have been envisioned as functional materials that can be used to cover a UAV's control surfaces or be embedded in them. These materials deform the external shape of the control surfaces upon command to control the attitude of the UAV. It was hoped that these materials could act as distributed actuators that will continue to allow for effective flight control of the UAV even if there was local failure in individual smart material units. In the literature, piezoceramics and Shape Memory Alloys (SMA) are the most extensively studied smart materials for UAV applications, and they will be reviewed for this research.

Lead zircontate titanate (PZT) is the most commonly used piezoceramic material for actuators. The crystalline domains of PZT are deformed when an electric field acts on permanent dipoles within the material, producing strains on the order of 0.1%. Essentially, the material is a capacitor that holds its position with little energy expenditure when a fixed voltage is applied. PZT have high specific power but its low strain usually requires that a means of coupling the material to produce useful mechanical work be included in the mechanism's design.

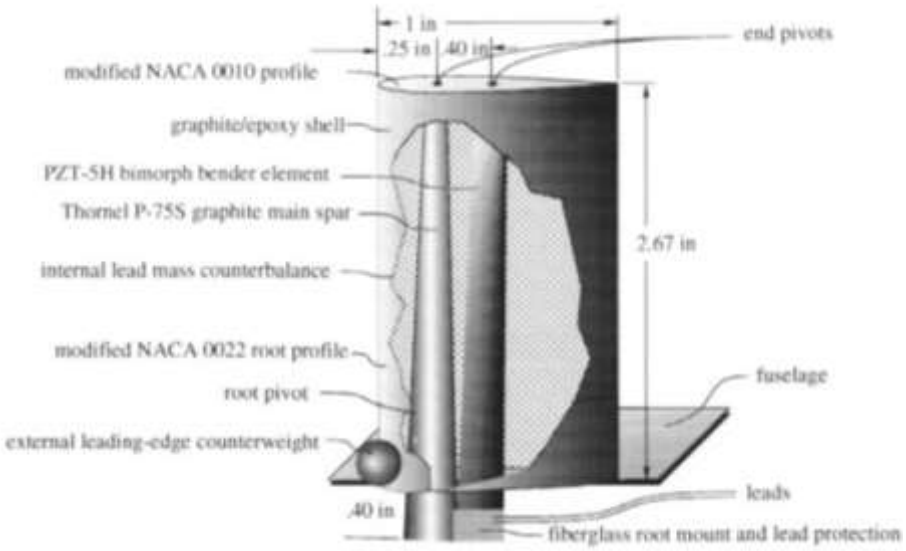

Figure 2-5: Flexspar wing internal structure for a TOW missile [15]

A 1996 study [15] incorporated a piezoceramic bimorph into the wings of a representative TOW missile (Figure 2-5), and deflections of the bimorph were used to deflect the wing. A bimorph is a means of increasing the deflection from piezoceramics by bonding two piezoceramic plates to either side of a plate of another material. Wind tunnel tests were conducted and deflections of +/- 14° at 0.1 to 100Hz were demonstrated. A team in the University of Delaware attempted to develop piezo-activated composite sandwich fins to improve projectile manoeuvrability [38]. The fins with piezoceramic patches on both surfaces are essentially a bimorph. A recent effort [16] employed Post-Buckled Precompressed (PBP) piezoelectric elements mounted within a transonic missile fin (Figure 2-6). PBP elements are piezoceramic bimorphs subjected to an axial force just short of buckling load, resulting in greater deflection when the piezoceramic plates on either side cause the bimorph to buckle.

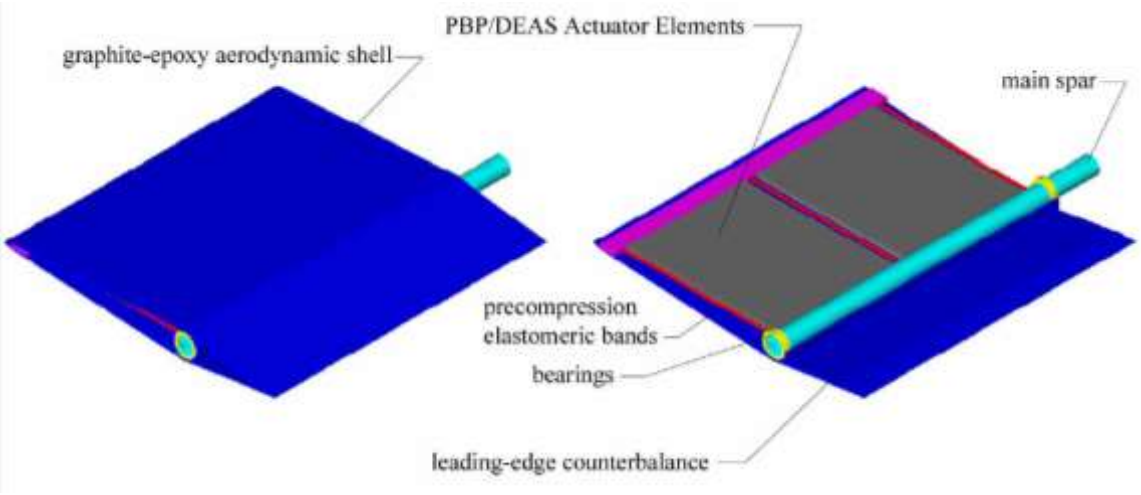

Figure 2-6: 15.2cm PBP-actuated control surface for a 113kg weapon [16]

In 2001, NASA's Smart Wing Phase II project used piezoelectric ultrasonic motors to rotate eccentuators that deflect ailerons on a representative UCAV (Figure 2-7) [39]. These ultrasonic motors use piezoceramics to rotate the output shaft, basically combining the high frequency small displacements of the material into useful rotational motion. In place of ultrasonic motors, the project also considered the use of stacks of piezoelectric material to pump hydraulic fluid to deflect the ailerons. Stacking the material is another means of combining the small strain of each layer into useful displacements. In a review [13], it was reported that piezo-actuators developed by EADS were capable of delivering 1000N force and 1.4mm stroke at a weight of 450g.

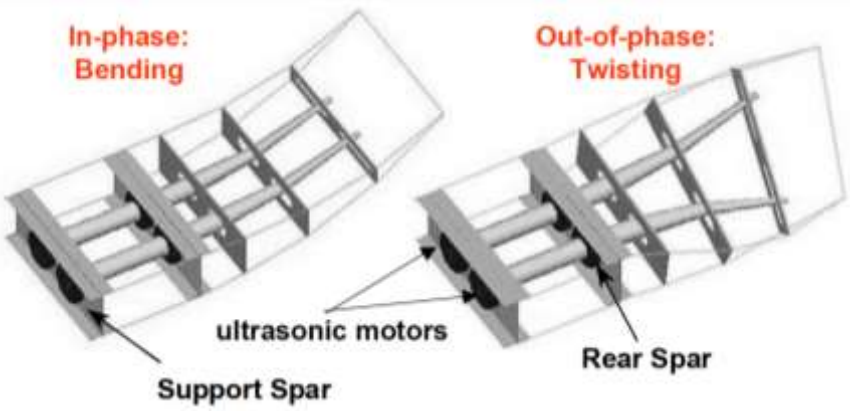

Figure 2-7: Ultrasonic motors driving eccentuators to deform control surfaces [39]

While the use of piezoceramic actuators to actuate flight surfaces has been demonstrated to be feasible, important reliability issues remain. The brittleness of piezoceramics has been a major obstacle for the University of Delaware team [38]. Dielectric breakdown of the piezoceramic actuators in high humidity conditions have also been reported to be serious areas of concerns [13]. Even for new piezo-based materials such as Macro Fiber Composites (MFC) that were devised by NASA to be tougher compared to conventional piezoceramics, 'harsh environments with extreme temperature, humidity, shock and vibration' continue to deter wide adoption [40]. The need for high voltages (and for ultrasonic motors, high frequency as well) require customised power electronics that are not widely available [41]. Advantages from reducing the size and weight of traditional electromagnetic actuators may also be greatly negated by the need for heavy and bulky power supply systems.

Shape Memory Alloys (SMA) are metals that exhibit a change in microstructure and mechanical properties as the temperature changes. At low temperatures, it has a martensite microstructure. Deformation of the material with a force will lead to the deformed shape being maintained after the force is removed. Heating the material to high temperatures causes its microstructure to change to austenite, and the material returns to its original undeformed shape. This is known as the Shape Memory Effect (SME).

SMAs are the next most investigated materials for flight surface actuation after piezoceramics. Exploitation of the SME characteristic have been attempted by numerous projects, with the most extensive being the Smart Wing Phase I by NASA [12]. The project used SMA torque tubes and SMA wires embedded on the top and bottom surfaces to twist and deflect the wing's trailing edge. While a wing twist of 4.5° and a deflection of 10° were achieved, the bandwidth achievable was limited due to the several seconds necessary for

the SMA tubes and wires to heat up through resistance heating and almost double the time to cool passively. It was estimated that even with active cooling, the maximum bandwidth achievable would be 1-2Hz, making it unsuitable for controlling operational aircraft.

Another study [42] employed SMA wires to deflect the wing's flap, an application where the bandwidth is less important. This project identified another issue with the use of SMA materials. SMA materials exhibit pseudoelasticity when it has an austenite microstructure after being heated to recover the original shape. A large force causes the material to deform by changing the material's microstructure to martensite through stress-induced transformation but the material transforms back to an austenite microstructure on removal of the force and recovers its original shape. This could cause the deflected flap to flutter when the cross section of the SMA material is insufficient or when the aerodynamic forces are great. The project overcame this problem with a SMA-actuated locking mechanism. In addition to potential issues with flutter, hysteresis, stress dependent response and the lack of a catch state make position control with SMA materials difficult. A lack of a catch state also requires continuous heating of the SMA wires to prevent transition to martensite, leading to high power consumption.

Without the discovery of new smart materials that operate on different principles, UAV actuators with electric motors as electrical to mechanical power converters will remain more competitive. Smart materials, in their current state-of-the-art, are not suitable for application as UAV actuators due to their inherent reliability issues in humid environments for piezoceramics and low bandwidth for SMAs. Importantly for UAV actuators, a comparison of actuator technologies during the Smart Wing project showed that smart

material actuators have inferior power densities compared to electric motor-based actuators [39].

2.4 Electro-Hydrostatic Actuators

Electro-Hydrostatic Actuators (EHA) are a relatively new class of hydraulic actuators that has only began to gain acceptance as manned aircraft flight control surface actuators recently. As part of the move to power-by-wire flight control system architecture and a 'more electric' aircraft, EHAs are gradually appearing in manned aircraft such as Lockheed Martin's F-35 (Figure 2-8). The attraction of EHAs for manned aircraft is obvious as it does away with the need for long high-pressure hydraulic lines that snaked throughout most present-day manned aircraft, while retaining the benefits of hydraulic actuation such as the ease of implementing multiple redundancies and high power densities.

Figure 2-8: F-35C control surface EHA [43]

Partially due to less stringent reliability requirements, UAVs have adopted power-by-wire flight control system architectures from the start. Initially thought of as simple, cheap and expendable replacements for manned aircraft, the need to minimise cost and complexity made power-by-wire and electromechancial actuators the natural choices for UAV flight

control systems. With the increase in reliability and performance demands for UAV actuators, EHAs can bring the benefits of hydraulic actuators to UAVs, while easily fitting into the power-by-wire architecture of UAVs.

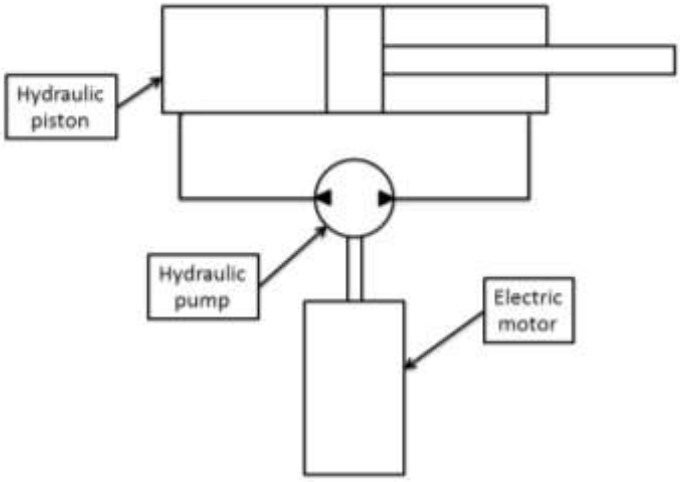

Figure 2-9: Schematic of an EHA

Fundamentally, EHAs (Figure 2-9) operate on the same principle of transmitting power through a fluid as other hydraulic actuators. The electric motor converts electrical power into mechanical power. The voltage, V and current, I_a supplied to the motor are related to the torque, T_e and speed, ω_m at its output by the motor constants K_t and K_m (Equation 2-10 is reproduced here)

$$T_e = K_t I_a \qquad 2\text{-}10$$

$$V = K_m \omega_m \qquad 2\text{-}18$$

The pump with a displacement, $Disp$ converts mechanical power into pressure, ΔP and flow, Q_p of the hydraulic fluid across it as it is driven by the motor

$$T_e = Disp \Delta P \qquad 2\text{-}19$$

$$Q_p = Disp \omega_m \qquad 2\text{-}20$$

This fluid power is converted back to mechanical power at the output, usually through a hydraulic piston with area, A that pushes and pulls a lever arm with a length, l_l to rotate the aircraft's control surface with a torque, T and rotational speed, $\dot{\delta}$

$$\mathrm{T} = \Delta \mathrm{P} \mathrm{A} \mathrm{l}_l \tag{2-21}$$

$$\mathrm{Q}_\mathrm{p} = \mathrm{A} \mathrm{l}_l \dot{\delta} \tag{2-22}$$

High pressure is the key to the high power density characteristic of hydraulic actuators. Conventional hydraulic actuators typically operate with maximum pressures at around 35MPa. For the same load output, a higher pressure reduces the required geometry of the hydraulic actuator and this in turn, reduces the flow rate of the hydraulic fluid and any associated power losses due to fluid flow. Thus, the miniaturisation of EHAs for UAV applications will necessitate the employment of high pressure. With the low torque available from small electric motors, input pumps for MEHAs will need to have very small displacements.

2.5 Miniature hydraulic pumps for MEHAs

Since pump technology for hydraulic actuators are an established field, it will be useful to review the state-of-the-art to understand their limitations for application in MEHAs. At a fundamental level, while operating at high pressures will improve the power density, MEHAs cannot be expected to operate at the pressure levels found in traditional hydraulic actuators. Manufacturing tolerances do not scale down linearly with the physical dimensions of a hydraulic actuator, thus leakage rates in MEHAs will be higher than that of typical hydraulic actuators and the maximum pressures that MEHAs can operate at will be lower. Seals can be added to reduce the leakage through pumps so that they can develop

higher pressure but this comes at a cost of increased friction which small electric motors will have to drive with their low torque capacity. Since the speed of electric motors is inversely related to the torque that it outputs, the presence of a large friction torque quickly reduces the maximum speed these miniature pumps can operate at. As a result, the power that can be delivered by MEHAs with such miniature pumps is low.

Gear pumps are an obvious first candidate for miniaturisation given its mechanical simplicity. An external gear pump consists of two meshing spur gears (Figure 2-10) that transport fluid from one side of the pump to the other using the spaces between the gear teeth and the casing, with the electric motor driving one of them. An internal gear pump has a small gear driving a larger external gear with internal teeth, with the fluid being transported in the space bounded by both gears. The meshing of the teeth at the center separates the inlet and the outlet. The simple geometry of external gear pumps makes them ideal for scaling down and the first attempts at producing pumps at micro-scale had started with gear pumps [44, 45, 46].

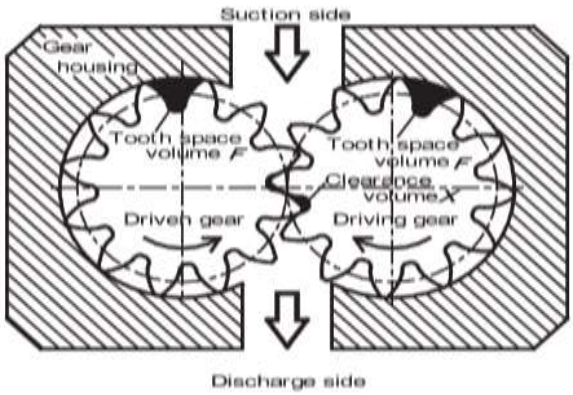

Figure 2-10: Gear pump schematic [47]

While the external gear pump may be mechanically simple in principle, its analysis is complex. The source of complexity is the volume enclosed by the contact of an earlier pair and the subsequent pair of teeth (Figure 2-11). This volume decreases initially as both gears

rotate to a minimum when the back side of the prior pair of teeth in contact is at the pitch point, before it starts increasing till the prior teeth in contact separates. This results in an increase in pressure in this volume initially and a subsequent decrease in pressure as the volume increases (Figure 2-11). This could cause damaging pressure peaks and cavitation within the pump. Thus, pressure relief grooves are usually machined into the faces of the pump in order to connect the volume between the teeth in mesh to the high pressure outlet initially, switching the connection of the volume to the low pressure inlet when the back side of the prior teeth pair passes the pitch point [48]. The low pressure inlet will be maintained at a pressure meant to prevent cavitation. This sequence of events during the meshing of the gear teeth results in a flow ripple that will be transmitted through the hydraulic circuit and it has to be modelled accurately to study its effects on the actuator output and hydraulic channel walls. In order to model the gear pump accurately, a method by [49] was adopted with modifications for easier computation.

Infinitesimal volume added to the control volume at the gear pump inlet, dV_i by the infinitesimal rotation, θ_p of the driving (subscript 1) and driven (subscript 2) gears (Figure 2-12) is a function of the pump width, w_p and gear radius, r_a

$$dV_{i1} = \frac{1}{2} w_p r_{a1}^2 d\theta_{1p} \quad 2\text{-}23$$

$$dV_{i2} = \frac{1}{2} w_p r_{a2}^2 d\theta_{2p} \quad 2\text{-}24$$

The infinitesimal volume removed from the control volume at the pump outlet, dV_o by the rotation of the driving and driven gears at the meshing point is similarly a function of the radial distance of the meshing point from the gear centres, ρ and pump width

$$dV_{o1} = \frac{1}{2} w_p \rho_1^2 d\theta_{1p} \quad 2\text{-}25$$

$$dV_{o2} = \frac{1}{2} w_p \rho_2^2 d\theta_{2p} \quad 2\text{-}26$$

Radial distance of meshing point from centers, ρ of driving (subscript 1) and driven (subscript 2) gears (Figure 2-12),

$$\rho_1^2 = l^2 + r_{g1}^2 - 2 r_{g1} l \sin\alpha \quad 2\text{-}27$$

$$\rho_2^2 = l^2 + r_{g2}^2 + 2 r_{g2} l \sin\alpha \quad 2\text{-}28$$

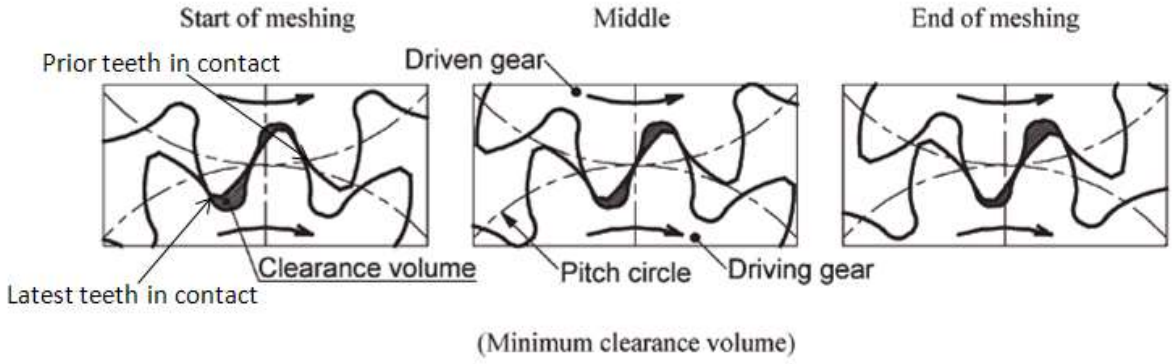

Figure 2-11: Meshing sequence in one mesh cycle [47]

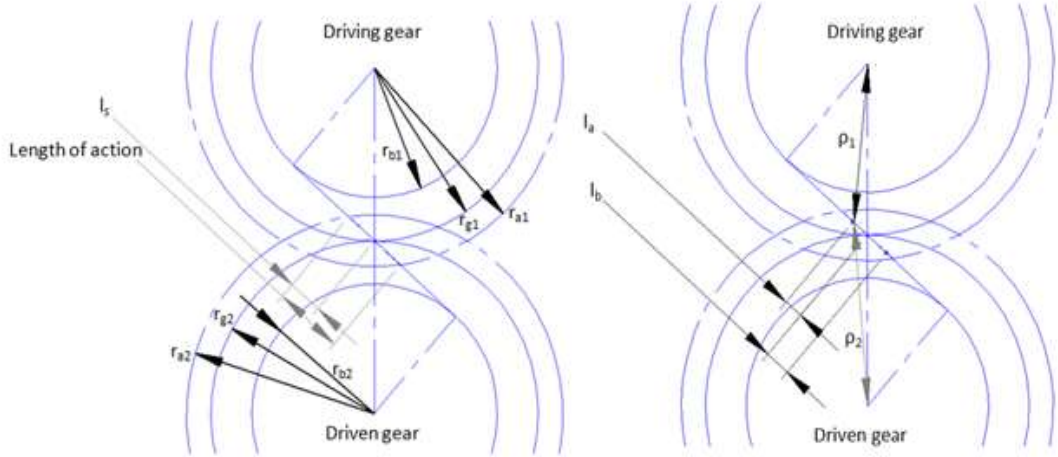

Figure 2-12: Gear pump lengths of action

With the substitution of ρ_1^2, ρ_2^2 and $\omega_{2p} = \frac{r_{g1}\omega_{1p}}{r_{g2}}$, the instantaneous flow rate generated by the gear pump is given by

$$Q_p = \frac{1}{2} w_p \omega_{1p} \left\{ (r_{a1}^2 - \rho_1^2) + \frac{r_1}{r_2} (r_{a2}^2 - \rho_2^2) \right\}$$

$$= \frac{1}{2} w_p \omega_{1p} \left\{ r_{a1}^2 - l^2 - r_{g1}^2 + 2 r_{g1} l \sin\alpha + \frac{r_{g1}}{r_{g2}} \left(r_{a2}^2 - l^2 - r_{g2}^2 - 2 r_{g2} l \sin\alpha \right) \right\}$$

$$= \frac{1}{2} w_p \omega_{1p} \left\{ r_{a1}^2 + r_{a2}^2 \frac{r_{g1}}{r_{g2}} - r_{g1}(r_{g1} + r_{g2}) - \left(1 + \frac{r_{g1}}{r_{g2}} \right) l^2 \right\} \quad \text{2-29}$$

While the instantaneous displacement, Disp can be found with

$$Disp = \frac{1}{2} w_p \left\{ r_{a1}^2 + r_{a2}^2 \frac{r_{g1}}{r_{g2}} - r_{g1}(r_{g1} + r_{g2}) - \left(1 + \frac{r_{g1}}{r_{g2}} \right) l^2 \right\} \quad \text{2-30}$$

All terms in the expression for the instantaneous flow rate are determined by the geometry of the gears, except for the instantaneous length of action l. As it is assumed that pressure relief grooves are present in the gear pump side walls, it implies that the volume removed from the control volume is dependent on the prior teeth pair in contact at the start of the meshing cycle, since the pressure groove near the inlet connects this volume to the inlet. Thus, from the start of the meshing cycle (Figure 2-13), $l = l_a$. Upon the back side of the prior teeth pair reaching the pitch point, the relief groove nearer to the outlet would have connected the trapped volume in the mesh of the gear teeth to the outlet and isolated it from the inlet, thus the volume removed from the control volume will then be dependent on the latest teeth that came into contact and $l = l_b$. The point in the meshing cycle where the back side of the prior teeth reaches the pitch point is also the point where the lengths of action of the prior and latest teeth contacts are equal i.e. $l_a = l_b$.

The instantaneous lengths of action [50] of the latest (subscript a) and prior (subscript b) teeth in contact is given as

$$l_a = l_s - r_{b1}\theta_1 \qquad 2\text{-}31$$

$$l_b = l_2 - r_{b1}\theta_1 \qquad 2\text{-}32$$

The initial length of action (i.e. the length of action when the gear teeth first comes into contact) [29] is found by

$$l_s = \sqrt{r_{a2}^2 - r_{b2}^2} - r_{g2}\sin\alpha \qquad 2\text{-}33$$

The initial length of action of the prior teeth that came into contact

$$l_2 = l_s - \pi m_n \cos\alpha \qquad 2\text{-}34$$

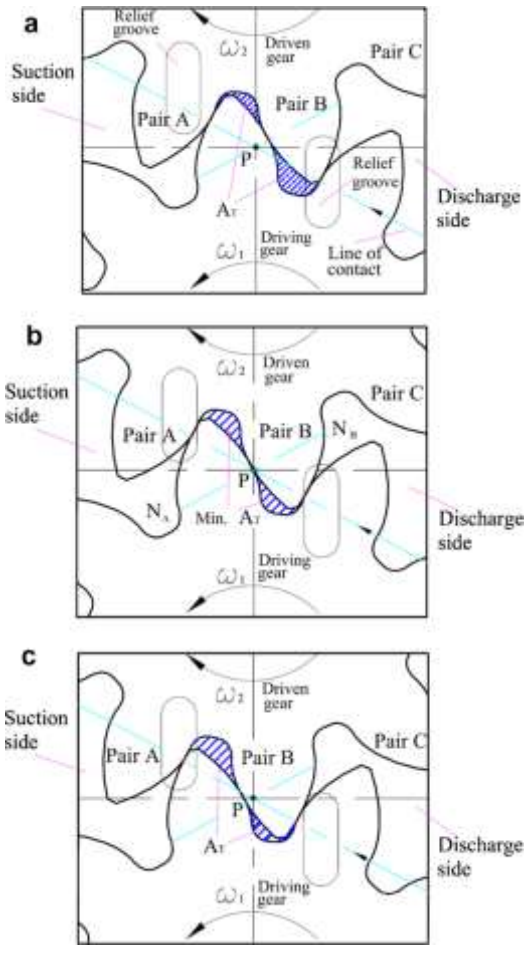

Figure 2-13: Pressure relief grooves in gear pump [50]

A pump for MEHA will require very small displacements and this is primarily achieved by reducing the width, $\mathrm{w_p}$ of the pump and radius, $\mathrm{r_{g1}}$ of the driving gear to reduce the gear pump displacement in Equation 2-30. Reducing the width and radius of the gear in a gear pump reduces the surface, σ_{Hlim} and tooth bending strengths, σ_{lim}, thus limiting the pressure and rotational speed of miniature gear pumps. The allowable bending and surface strengths of the gear are given by the following relationships [51]

$$\frac{\mathrm{F}_{gear}}{\mathrm{m_n w_p}} < \sigma_{lim} \qquad 2\text{-}35$$

$$\sqrt{\frac{\mathrm{F}_{gear}}{2\mathrm{r_{g1} w_p}}} < \sigma_{Hlim} \qquad 2\text{-}36$$

In addition, the gears are subjected to the pressure difference across the pump and this pressure load reduces the speed at which the gears' supporting bearings can operate at. Leakage across the face of the gears is a significant issue for all gear pumps and miniature gear pumps will have greater relative leakage with its manufacturing tolerances relative to pump dimensions being greater than that of conventional gear pumps, thus introducing another limiting factor on its maximum operating pressure. As a result, commercial miniature external gear pumps typically are limited to a maximum of 1.7MPa, 8000rpm and 5W [52]. As such, miniature gear pumps are simply unable to transmit the levels of power required for high performance UAVs. The inlets and outlets of gear pumps can be shaped to act as passive valves to increase the operating pressure across the pump in one flow direction but that will allow only for pump operation in one direction, thus making such a scheme unsuitable for application in MEHAs. The large size and low power density of miniature gear pumps will also make MEHAs employing them uncompetitive compared to EMAs.

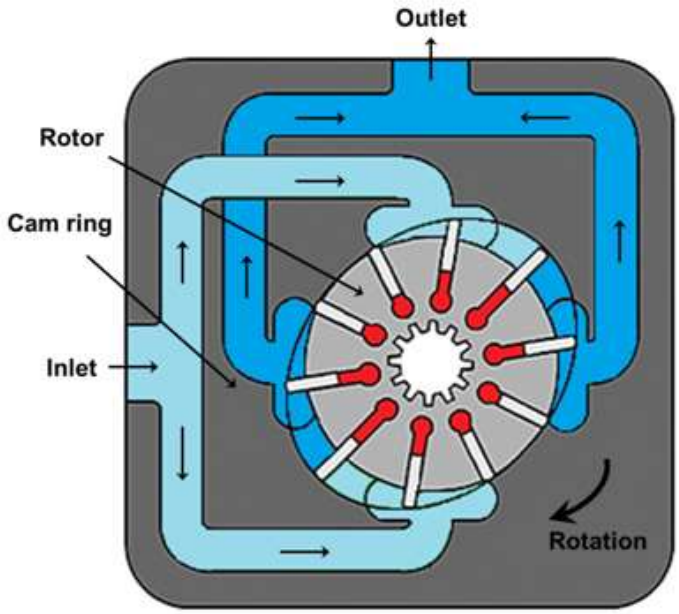

Figure 2-14: Schematic of a balanced vane pump [53]

While gear pumps are typically used in low-power hydraulic machines, vanes pumps (Figure 2-14) are usually employed in medium power hydraulic machines [54]. Vanes in slots on the pump rotor are displaced outwards by centrifugal forces to contact with the pump casing. The casing has a profile that guides the radial position of the vanes, thereby varying the volume between the vanes to draw in hydraulic fluid at the pump inlet and pump out fluid at the outlet. Within the slots on the rotor, the inner ends of the vanes are usually exposed to the inlet pressure. As the vanes approach the high pressure outlet of the pump, the centrifugal force acting on the vanes has to be greater than the force due to the pressure difference in the radial direction in order for the vanes to maintain contact with the pump casing so as to seal the pump outlet from its inlet.

Miniaturisation of the vane pump reduces the pressure that it can deliver. The centrifugal force acting on the vane with mass, m_v with its centre of mass at a distance r_{vcg} from the centre of rotation and rotating at a rotational speed $\dot{\theta}_m$ has to be greater than the force due to the pressure difference ΔP between the vane tip and its opposite end within the pump

rotor acting the projected area of the vane tip formed by the vane thickness, b_v and width, w_p. Thus,

$$m_v r_{vcg} \dot{\theta}_m^2 > \Delta P w_p b_v \qquad 2\text{-}37$$

By linearly scaling down the geometry of a vane pump, the pressure difference that the pump can deliver will scale down by the power of two. Certain design features can be incorporated to alleviate the effect of scaling down but the inherent limits of vane pump technology constrains the pressure limits of commercial miniature vane pumps to 7MPa [55]. Miniature vane pumps are also typically designed to pump unidirectional flow with the aid of passive valves, making them unsuitable for application in MEHAs. Springs have been used to push the vanes out of the rotor for some vane pumps but it will be difficult to implement such springs for miniature vane pumps and fatigue strength of the springs will become a limit on the life of the pump. Maximum operating pressure will also be limited due to relative leakage between the vane pump rotor and casing being greater. In addition, the speeds of vane pumps are limited by the wear of the vanes against the pump casing. For some uni-directional constant high speed applications, it is possible to add tilting pads to the ends of the vanes for the pump to operate with high input rotational speeds [56] but these are not feasible for miniaturised vane pumps for MEHAs that have to be bidirectional and operate in a wide range of speeds. For conventional miniature vane pumps, input rotational speeds are limited to 1800rpm [55]. Taken together, conventional miniature vane pumps cannot be used to realise MEHAs competitive with EMAs due to their low power density and their need for uni-directional operation to sustain any useful pressure.

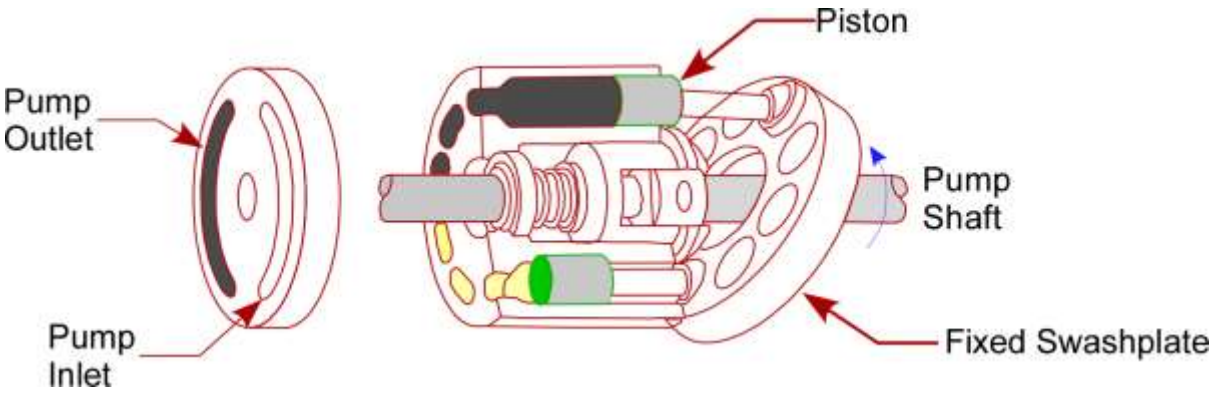

Figure 2-15: Piston pump schematic [57]

Piston pumps (Figure 2-15) are the most widely used pump for high power hydraulic actuators [54]. Multiple pistons are connected to the swash plate which controls the axial position of the piston. As the pistons are rotated by the rotor, the swash plate forces the piston to draw in fluid at the pump inlet and pump out fluid at the outlet. Springs can also be installed in the piston bores to push the pistons against the swash plate and draw in fluid at the pump inlet [58]. Among hydraulic pumps, piston pumps can deliver the highest pressure while operating at the highest rotational speed.

In order to operate piston pumps at higher rotational speeds for MEHAs, the forces acting on the swash plate will increase. Consider the equation of motion for a single piston,

$$m_p \ddot{x}_p = f_{bx} - A_p P_p - f_s - f_d \qquad 2\text{-}38$$

$$f_{bx} = m_p \ddot{x}_p + A_p P_p + f_s + f_d \qquad 2\text{-}39$$

The mass of the piston, m_p, is accelerated by the force acting on it through the ball joint, f_{bx},against the pressure P_p acting on the face area of the piston, A_p, and the friction and viscous drag acting on the piston, f_d. A miniature pump will require mechanical simplicity, so assuming that the spring return of the piston is used, f_s is the force of the spring acting on the piston. An increase in the input rotational speed of the pump will result in an increase in

the acceleration of the piston, $\ddot{x}_p$. At the pump inlet where the spring has to push the piston against the swash plate to draw hydraulic fluid into the piston so it is assumed that $f_{bx} = 0$. Also assuming that the opposite end of the piston is subjected to the inlet pressure, $A_p P = 0$ and

$$f_s = m_p \ddot{x}_p + f_d \qquad 2\text{-}40$$

Thus, an increase in piston acceleration with an increase in input rotational speed also increases the required spring force. Together, these lead to an increase in the force transferred through the ball joint to the swash plate, translating to increased wear between the piston slipper and the swash plate. Since wear on a surface is correlated with the pressure acting on the surface and the relative speed between the contacting surfaces, there is a need to limit the input rotational speed. As a result, miniature piston pumps are limited to input rotational speeds of about 2000rpm, even though they are able to operate with pressures of up to 14MPa [59]. Leakage between the miniature piston pump's rotor and casing as well as across the individual pistons relative to the pump displacement will be greater than conventional piston pumps, thus maximum operating pressures of miniature piston pumps tend to be lower than the 35MPa that typical piston pumps operate at [54]. Miniature piston pumps have the greatest potential among conventional miniature pumps to realise MEHAs that can meet the EMA benchmark, as there are commercially available products that can transmit the amount power required. However, these products have a low power density and due to the low speed limits, there is a need for gears to step down the speed from the electric motors, lowering the combined power density further.

Substantial effort was spent during the course of this work to develop an alternative miniature pump that would have been able to rotate at high input speeds of more than

10000rpm while being able to withstand high pressure across it. The Axial Vane Pump (AVP) (Figure 2-16) is a miniature hydraulic pump conceptualised in this work to enable the realisation of MEHAs for UAVs. It is a fixed displacement pump with vanes that move axially. Axial displacement of the vanes allows the pump to move hydraulic fluid from the low to the high pressure side as they rotate with the rotor. Four transition segments each on the front and rear cam surfaces guide the vanes between both axial positions, while rotor slots rotate the vanes within the pump. The radial motion of the vanes is constrained both by the clamped plate and the rotor slots. Each vane is forced against the cam, clamped plate and rotor slot by springs within the slot to seal the ports of the AVP from each other.

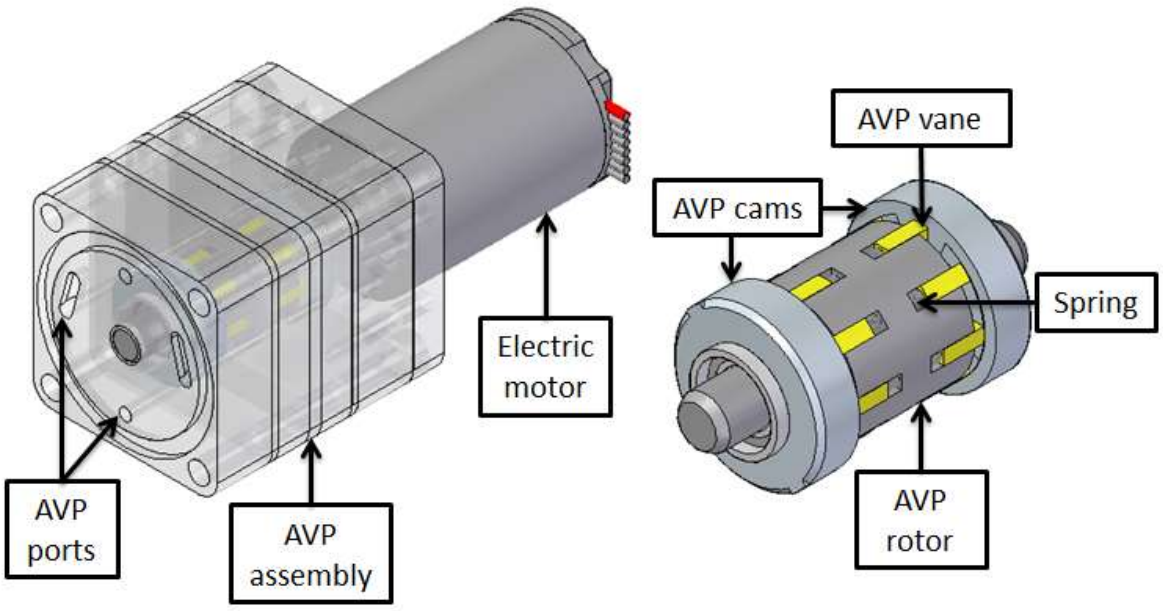

Figure 2-16: AVP schematic

Both the front and rear sides of the AVP displaces fluid but in opposite directions. The clamped plate has port openings and channels machined on one side to direct the flow of the hydraulic fluid. Its inner diameter forms a seal with the vanes as they are rotated by the rotor. The width of the port openings match the width of the vanes so that when the vanes are at the mid-point of the transition segment of the cam, they completely block the port

opening before the port is exchanged between enclosed volumes. Part of the clamped plate overlaps the rotor to prevent the leakage of hydraulic fluid between the rotor and the mid casing. It is clamped between the end and mid AVP casings to prevent leakage of hydraulic flow out of the AVP.

But tests with the AVP prototype reviewed substantial problems with leakage and running friction. To lower the rate of leakage, stiffer springs were used to increase the contact between the vanes and the cam and clamped plate but this led to a substantial increase in friction opposing the electric motor. Reducing the stiffness of the springs reduces the friction but the leakage rate increase quickly and the prototype is unable to develop useful pressure across it. Reducing the tolerances between pump components in an effort to reduce leakage similarly resulted in unacceptable levels of friction. Last but not least, the prototype AVP assembly proved difficult to fabricate and assemble during the testing phase.

Reviewing current hydraulic pump technologies, it can be concluded that they are not amendable to miniaturisation for operation at the high rotational speed of small electric motors and at high pressure for application in MEHAs. Gear pumps are limited by gear teeth strength, while piston pumps are limited by wear of the piston slippers and swash plate at high speed. Vane pumps are inherently not suitable for high pressure at miniature scales and have issues with the wear on vanes. The geometries of these pump types result in leakage paths that are larger relative to pump dimensions when they are scaled down, leading to greater leakage rates relative to pump displacement and lower maximum operating pressures. Substantial efforts during the course of this work to develop a new miniature pump suitable for MEHA applications revealed intractable problems. Thus MEHAs for UAVs require a new approach that does not require miniature pumps.

3. THEORETICAL BACKGROUND & MODELLING

This chapter serves to develop the equations and models that will be used to analyse the MEHA. Section 3.1 first provides a description of the MEHA. Sections 3.2 to 3.11 develop the governing equations required for the design, optimisation and analysis of the MEHA. This is followed by Section 3.12 where the non-linear dynamic model of the MEHA is developed.

3.1 Description of the MEHA

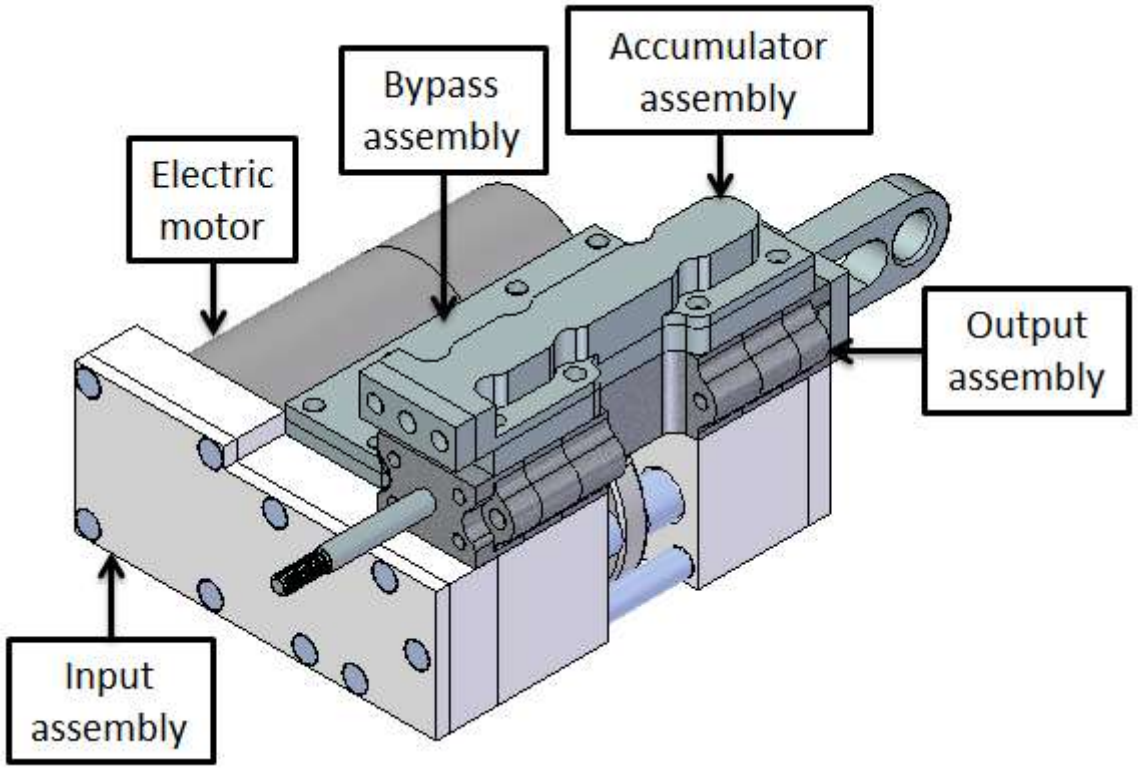

Figure 3-1: Overview of MEHA prototype

The MEHA consists of four major assemblies as shown in Figure 3-1. The input assembly is made up of an electric motor that drives a ballscrew shaft through a gear train. The rotational motion of the ballscrew shaft is converted to the linear motion of its nut that in turn drives the input pistons. These pistons generate a pressure and flow within the two closed hydrostatic circuits on both sides of the ballscrew nut. A schematic of the input assembly is shown in Figure 3-2.

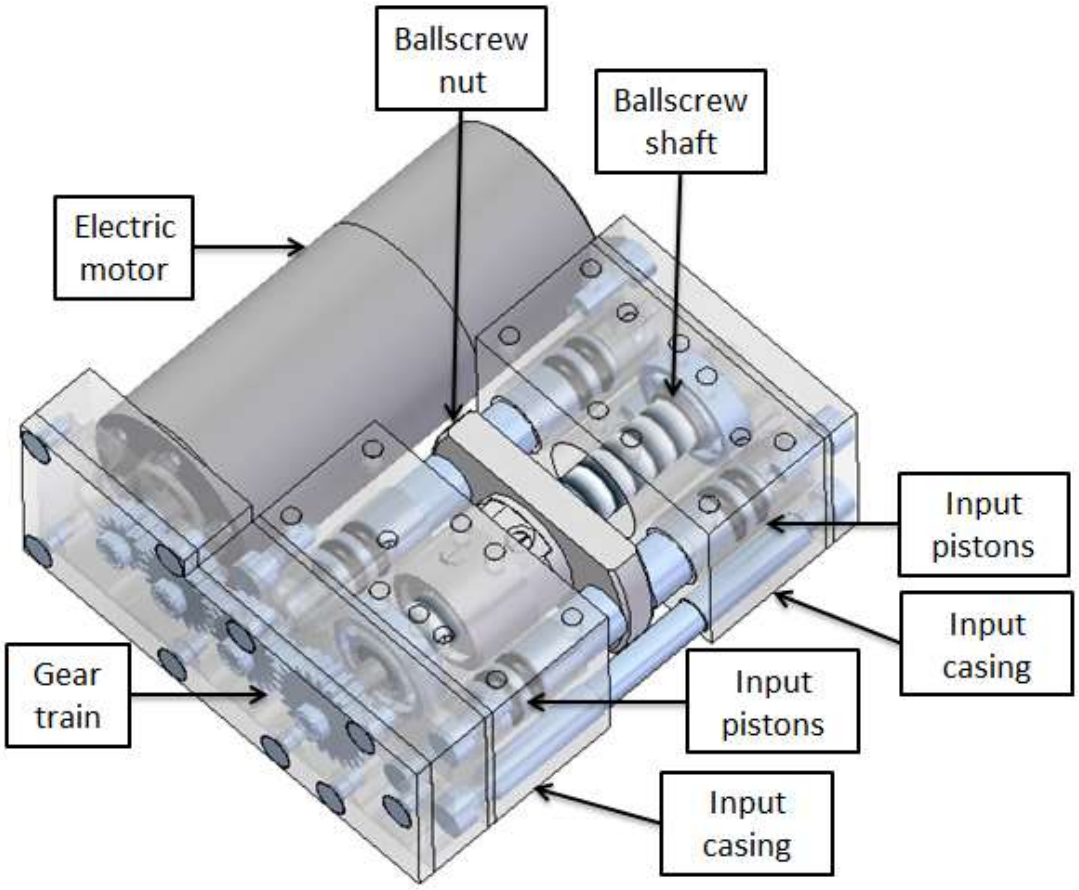

Figure 3-2: Schematic of input assembly

The circuits are connected to opposing sides of the output piston in the output assembly in Figure 3-3. The output piston converts the pressure difference across it and the flow in both hydrostatic circuits into a force and velocity at the piston that is in turn converted to a torque and rotational velocity at the UAV's control surface. The output casing consists of a centre casing and two inner and outer covers on each end. The ports of the output assembly on the inner covers also act as the junction that connects the flow channels from the accumulator and input assemblies. An attachment point at the rear of the output assembly allows for the mounting of the MEHA on a hardpoint within the UAV's structure.

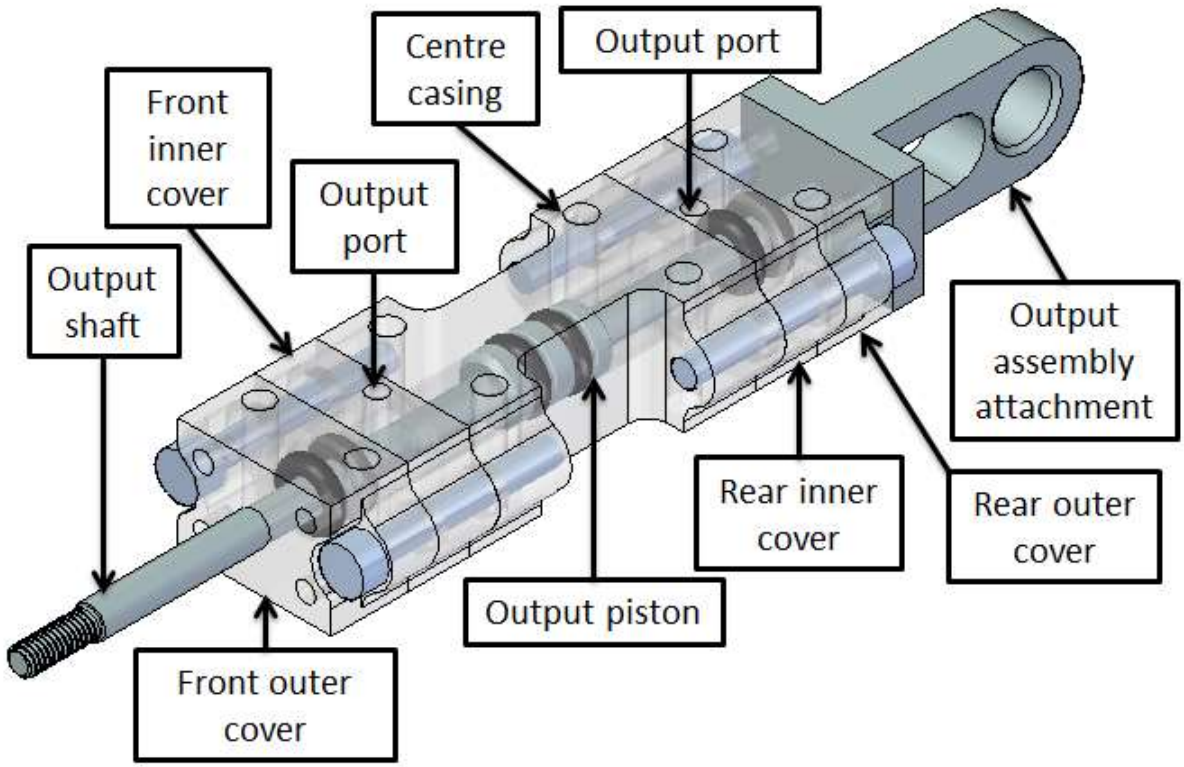

Figure 3-3: Schematic of output assembly

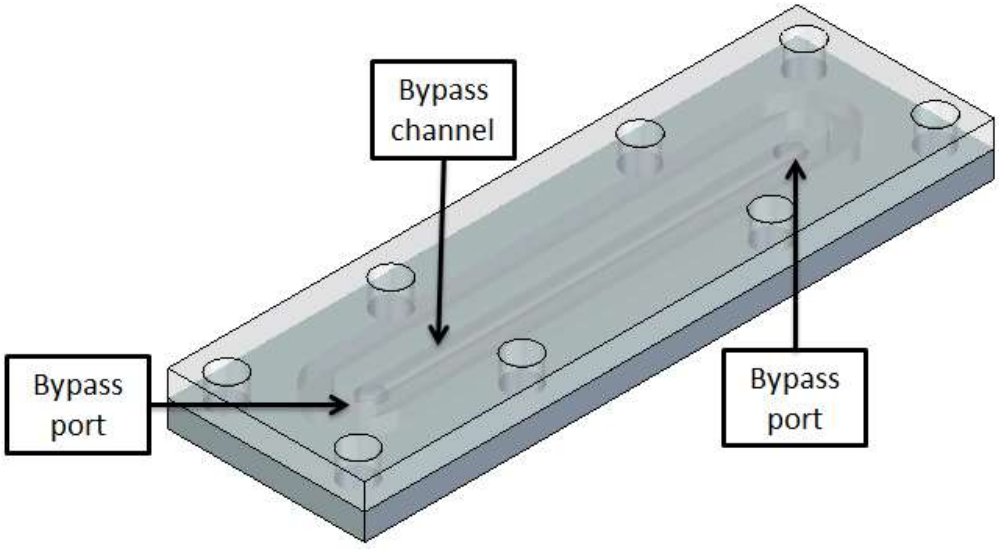

Figure 3-4: Schematic of bypass assembly

In the event of an electrical failure or mechanical jamming at the EMA, a bypass valve will be opened to allow hydraulic fluid to flow freely across opposing fluid volumes in both hydrostatic circuits. The output piston is thus isolated from the input pistons and the UAV's control surface is able to continue moving in a damped mode. In this work, a simplified

representation of the bypass valve (Figure 3-4) is used to simulate the effects of the MEHA operating in damped mode.

The accumulator assembly houses the accumulator circuit that is separated from the closed hydrostatic circuits on both sides of the output piston by ball valves. A spring accumulator maintains a pressure within the accumulator circuit. The ball valves act as flow controls to ensure that the minimum pressures in both hydrostatic circuits do not fall below the accumulator pressure to prevent cavitation in the hydraulic fluid while enabling the pressure difference between the hydrostatic circuits to increase when the ballscrew nut exerts a force on the input pistons. In addition, the accumulator also replenishes the hydraulic fluid within the closed hydrostatic circuits as decreases in the MEHA's operating temperature or leakage reduce the volume of hydraulic fluid within the circuits. Figure 3-5 shows the schematic of the accumulator assembly.

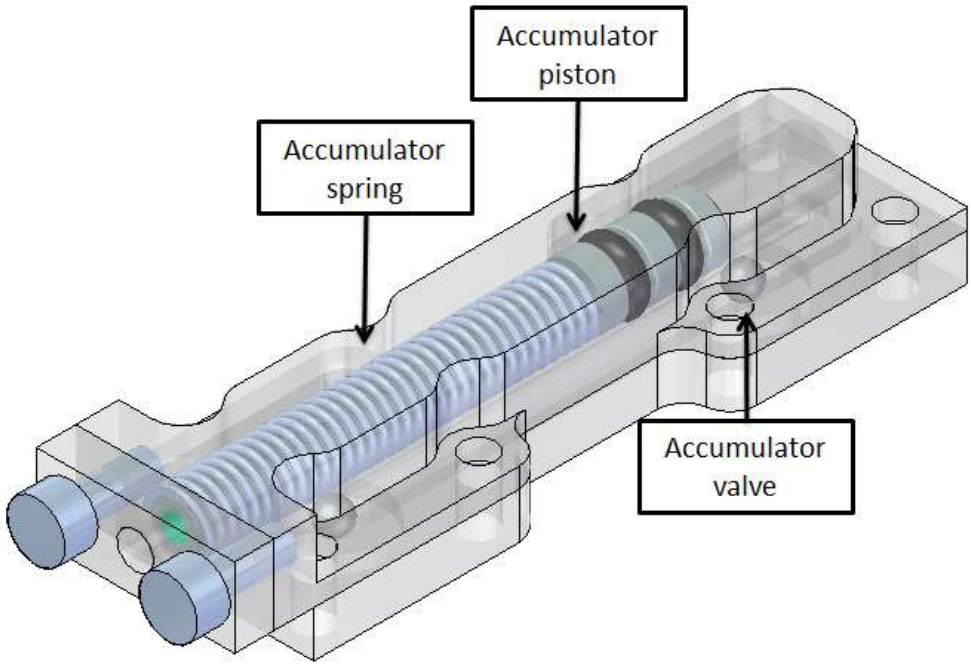

Figure 3-5: Schematic of accumulator assembly

3.2 Motor selection

The first step in the design of the MEHA involves the selection of a suitable electric motor. The torque $\mathrm{T_e}$ and rotational speed ω_m supplied by the electric motor is transmitted through the MEHA as a torque T to drive the UAV's control surface at a rotational speed $\dot{\theta}$ with losses along the transmission accounted for by n.

$$\mathrm{T}\dot{\delta} = n\mathrm{T_e}\omega_\mathrm{m} \tag{3-1}$$

Thus, a motor selected for the MEHA has to have a peak power capacity matching that required at the UAV's control surface, with an excess to account for efficiency losses.

3.3 Total reduction ratio

The MEHA's transmission converts the torque and rotational speed at the electric motor to the torque and rotational speed required at its load through a reduction ratio. This ratio is a function of the ballscrew lead, L, output lever arm length, l_l, gear train gear ratio, $\frac{\mathrm{N_b}}{\mathrm{N_e}}$ and ratio of the output piston to input piston areas, $\frac{\mathrm{A}}{\mathrm{A_{ip}}}$. It can be derived to be

$$\mathrm{N} = 2\pi\frac{\mathrm{A}}{\mathrm{A_{ip}}}\frac{\mathrm{N_b}}{\mathrm{N_e}}\frac{l_l}{\mathrm{L}}\sin\theta \tag{3-2}$$

Where θ is the angle subtended by output piston line of action and lever arm (Figure 3-6) and it can be found by,

$$\sin\theta_{\mathrm{extension}} = \frac{\mathrm{x_o}\cos\delta_{\max} + l_l\sin\delta_{\max}}{\sqrt{2l_l^2 + \mathrm{x_o^2} - 2l_l^2\cos\delta_{\max} + 2l_l\mathrm{x_o}\sin\delta_{\max}}} \tag{3-3}$$

$$\sin\theta_{\mathrm{retraction}} = \frac{\mathrm{x_o}\cos\delta_{\max} - l_l\sin\delta_{\max}}{\sqrt{2l_l^2 + \mathrm{x_o^2} - 2l_l^2\cos\delta_{\max} - 2l_l\mathrm{x_o}\sin\delta_{\max}}} \tag{3-4}$$

Derivation of N and θ can be found in Appendix A.

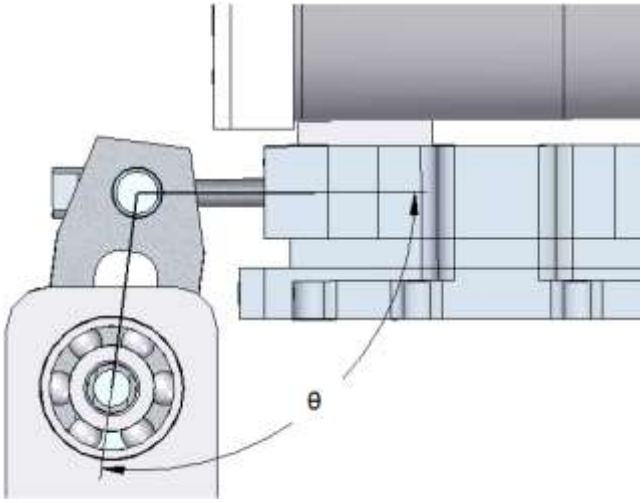

Figure 3-6: Angle subtended by output piston line of action and lever arm

The reduction ratio for the MEHA has to be optimised to balance the voltage and current drawn by the electric motor while driving the benchmark load at the required load case. A low reduction ratio will increase the current drawn by the motor while a high reduction ratio will increase the supply voltage required at the motor. At either extreme, the voltage and current limits on the electric motor's controller will result in the MEHA being unable to drive the benchmark load at the required load case.

A simplified first-order model is used for this optimisation. It considers only the motor and load inertias, ignoring the transmission inertia as well as any friction or damping. It also assumes that the hydraulic fluid within the closed hydrostatic circuit is incompressible and that the MEHA's components are infinitely stiff. These assumptions are necessary to allow for a quick optimisation process in the initial stages of the MEHA prototype's design when various parameters are unknown. For the electrical block in this model (Figure 3-7), electrical power from the UAV is input to the electric motor as voltage, V_s and current, I_a and the dynamics of the electrical circuit are modelled with the inductance, L_a and resistance, R_a of the motor,

$$V_s = L_a \dot{I}_a + R_a I_a + E_m \qquad 3\text{-}5$$

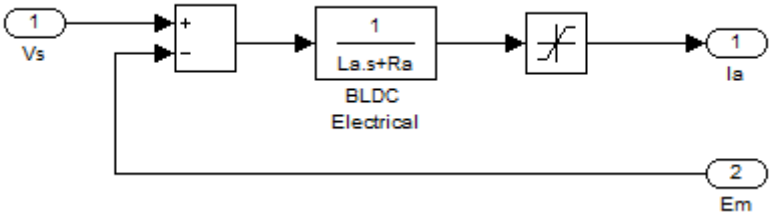

Figure 3-7: Dynamic model of electrical subsystem

A limit is placed on the current output of the electrical block to simulate the current limitation of the motor controller. In the BLDC motor block (Figure 3-8), the torque produced by the brushless electric motor, T_e is related to the current by the motor constant, K_t,

$$T_e = K_t I_a \tag{3-6}$$

While the back EMF, E_m generated in the motor's windings is related to the motor rotational speed, $\dot{\theta}_m$ by another motor constant, K_m,

$$E_m = K_m \dot{\theta}_m \tag{3-7}$$

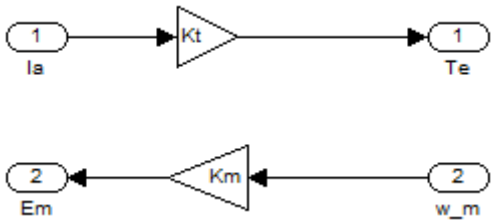

Figure 3-8: Dynamic model of BLDC motor

This is followed by the mechanical block (Figure 3-9) where the torque generated by the electric motor drives the rotational inertias of the motor, J_m and the ballscrew shaft, J_b against the friction torque, T_f and the load torque from the ballscrew nut, T_b

$$T_e = \left(J_m + J_b + m_{nut}L^2 + m_{ip}L^2\right)\ddot{\theta}_m + T_b + T_f \tag{3-8}$$

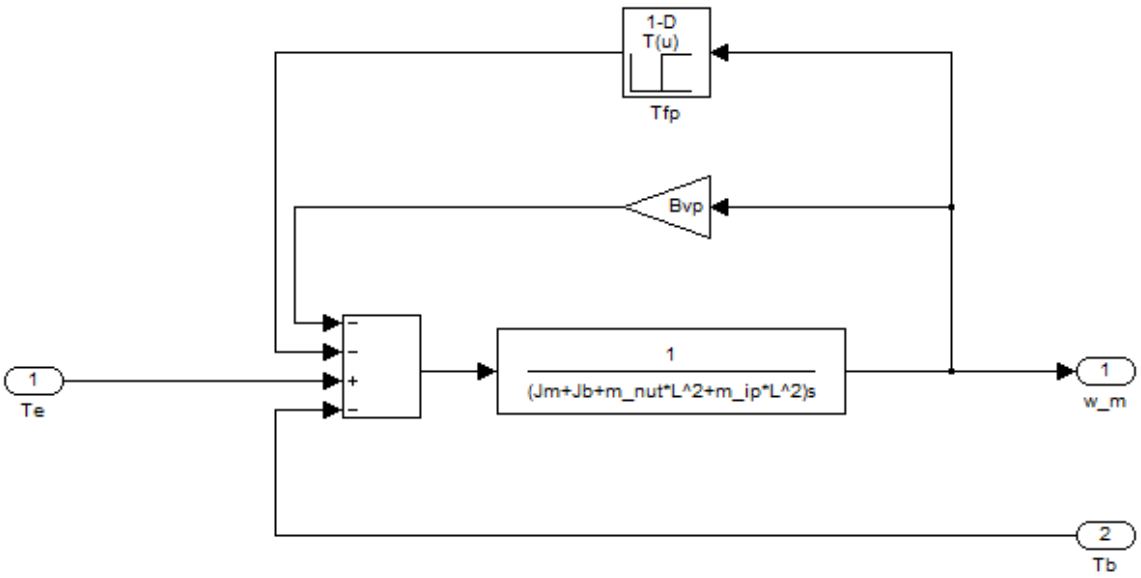

Figure 3-9: Dynamic model of BLDC rotor, ballscrew and input piston

The closed loop model of the MEHA is presented in Figure 3-10. It consists of an inner speed control loop with a linear controller and an outer position control loop with another linear controller to simulate the electric motor's controller. The controller of the inner speed control loop has to be tuned separately such that its bandwidth is at least a magnitude greater than the expected bandwidth of the outer position control loop. The outputs of the controllers have limits corresponding to the motor controller's voltage output limits. The total reduction ratio, N, is used to represent the entire MEHA's transmission and it will be varied to find the optimal value for the benchmark performance and selected motor.

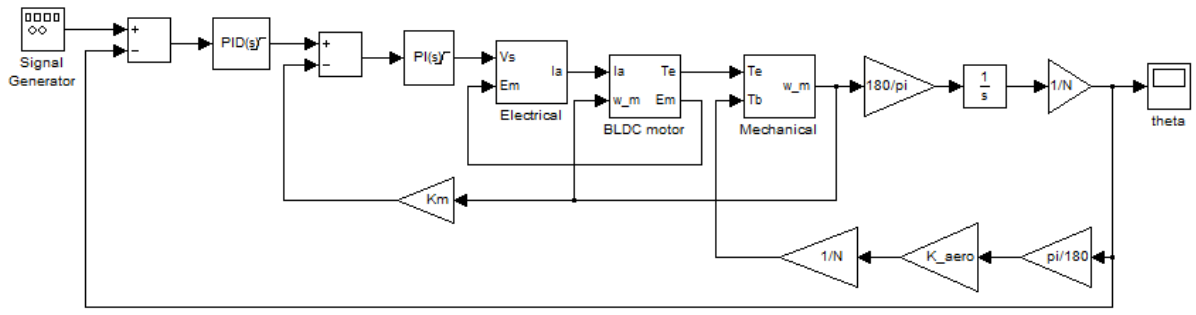

Figure 3-10: Dynamic model of the MEHA for optimisation of its total reduction ratio

After the electric motor and the total reduction ratio have been selected, the maximum torque at the UAV's control surface can be determined by

$$T = NT_e \tag{3-9}$$

3.4 Ballscrew selection

In the MEHA's input assembly, the torque from the electric motor is stepped up to the torque at the ballscrew shaft via the gear ratio $\frac{N_b}{N_e}$ of the gear train before it is converted by the lead of the ballscrew into a force at the input piston of the closed hydrostatic circuit. The ballscrew's lead is an integer value and the range of lead values available is typically limited for miniature ballscrews, while the choice of gear ratio is constraint by the distance between motor and ballscrew shafts as well as practical gear module. Above all, the expected maximum force that the ballscrew nut has to exert must be within the load limit of the ballscrew. Thus, the sizing of the MEHA should logically begin with a parametric study to choose a suitable ballscrew lead and gear train ratio. The governing equations for such a parametric study are

$$T_b = \frac{N_b}{N_e} T_e = \frac{F_b L}{2\pi} \tag{3-10}$$

$$F_b = \frac{2\pi}{L} \frac{N_b}{N_e} T_e \tag{3-11}$$

The choice of ballscrew lead and gear train ratio affects the stroke length required of the ballscrew for the required range of deflection angles at the UAV's control surface. This is in turn constraint by the need to minimise the physical size of the MEHA. The maximum stroke required of the ballscrew can be derived by first considering the MEHA's total reduction ratio, N and the maximum deflection angle required at the UAV's control surface, δ_{max},

$$\pm\theta_{m,max} = \pm N\delta_{max} \tag{3-12}$$

The maximum rotational displacement of the electric motor, $\theta_{m,max}$ is translated to the maximum rotational displacement of the ballscrew shaft via the gear train, which is then converted to the maximum linear motion of the ballscrew nut, $x_{ip,max}$.

$$\pm x_{ip,max} = \pm N \frac{1}{N_b/N_e} \delta_{max} \frac{L}{2\pi} \quad 3\text{-}13$$

3.5 Gear train design

The gear train transmits mechanical power from the electric motor to the ballscrew and steps up the torque driving the ballscrew shaft in the process. It also reduces the rotational speed at the electric motor so that the ballscrew shaft can rotate at a lower speed that is within its recommended speed limits. The orientation of the electric motor with respect to the ballscrew shaft requires idler gears between the gears attached to both shafts. With the selection of an optimised gear ratio, $\frac{N_b}{N_e}$ and a convenient module value, m, the design of the gear train begins with finding the pitch diameters of the idler gears, d_i in addition to the gears on the electric motor shaft, d_e, and ballscrew shaft, d_b

$$d_e = mN_e \quad 3\text{-}14$$

$$d_b = mN_b \quad 3\text{-}15$$

$$d_i = mN_i \quad 3\text{-}16$$

The contact ratio of the gear measures the overlap between the preceding pair of gear teeth ceasing contact and the next pair of gear teeth coming into contact. It is recommended that it be greater than 1.2 to ensure smooth continuous motion. Using the standard pressure angle of 20°, the contact ratio can be calculated using [51]

$$\varepsilon_{\gamma,e} = \frac{\sqrt{\left(\frac{d_e}{2}+1.25m\right)^2-\left(\frac{d_e}{2}-m\right)^2}+\sqrt{\left(\frac{d_i}{2}+1.25m\right)^2-\left(\frac{d_i}{2}-m\right)^2}-\frac{1}{2}(d_e+d_i)\sin 20°}{\pi m \cos 20°} \quad 3\text{-}17$$

$$\varepsilon_{\gamma,b} = \frac{\sqrt{\left(\frac{d_b}{2}+1.25m\right)^2-\left(\frac{d_b}{2}-m\right)^2}+\sqrt{\left(\frac{d_i}{2}+1.25m\right)^2-\left(\frac{d_i}{2}-m\right)^2}-\frac{1}{2}(d_i+d_b)\sin 20°}{\pi m \cos 20°} \quad 3\text{-}18$$

The bending strength of the gear train limits the mechanical power that can be transmitted through it. According to AGMA Standard 2001-B88, the tooth stress due to bending can be estimated using

$$\sigma_t = \frac{F_{gear}}{mw}\frac{K_a K_s K_{ld} K_B}{K_v K_J} \quad 3\text{-}19$$

Where K_J is the geometry factor, K_a is the application factor, K_s is the size factor, K_{ld} is the load distribution factor, K_B is the rim thickness factor, K_v is the dynamic factor and the maximum force acting at the gear teeth contact, F_{gear} can be found using

$$F_{gear} = \frac{T_{e,max}}{d_e/2} \quad 3\text{-}20$$

3.6 Piston diameter and lever arm length sizing

Having selected the motor, gear train ratio and ballscrew, the maximum force $F_{b,max}$ that can be exerted on the closed hydrostatic circuits at the input pistons is defined. The need to minimise the size of the MEHA requires the selection of the smallest diameter for the input pistons. This selection is constraint by the size of the smallest seals available and the maximum sealing pressure of these seals. For a selected diameter and its corresponding area, A_{ip}, the maximum pressure above the minimum accumulator pressure in the closed hydrostatic circuit can be found by

$$\Delta P_{max} = \frac{F_{b,max}}{A_{ip}} \quad 3\text{-}21$$

With the expected maximum pressure within the closed hydrostatic circuit, the output piston and the length of the lever arm, l_l can be sized to meet the maximum torque required at the UAV's control surface as determined during the selection of the MEHA's total reduction ratio. The maximum force, $\mathrm{F_{max}}$ produced by the output piston can be found by considering the piston area, A exposed to the maximum pressure above the accumulator pressure, $\Delta \mathrm{P_{max}}$

$$\mathrm{F_{max}} = \Delta \mathrm{P_{max}} \mathrm{A} = \Delta \mathrm{P_{max}} \left(\frac{\pi}{4} \mathrm{d_p^2} - \frac{\pi}{4} \mathrm{d_{shaft}^2} \right) \quad 3\text{-}22$$

The maximum torque, $\mathrm{T_{max}}$ produced at the UAV's control surface can then be found by

$$\mathrm{T_{max}} = \mathrm{F_{max}} l_l \sin \theta = \Delta \mathrm{P_{max}} \mathrm{A} l_l \sin \theta \quad 3\text{-}23$$

The selection of an optimum lever arm length, l_l, output piston diameter, $\mathrm{d_p}$ and shaft diameter, $\mathrm{d_{shaft}}$ will minimise the output piston's diameter and stroke length, $\mathrm{x_{max}}$ to minimise the overall dimensions of the MEHA's output assembly and to maximise its power density.

Knowing the output piston's stroke length and area, the volume of hydraulic fluid required to actuate it the full stroke length can be used to determine the required maximum linear motion of the ballscrew nut,

$$\mathrm{x_{ip,max}} = \frac{\mathrm{A x_{max}}}{\mathrm{A_{ip}}} \quad 3\text{-}24$$

With knowledge of the input piston diameters, the sizing of the MEHA's input assembly will be complete. For the output assembly, the sizing of the output piston and the lever arm will be similarly complete.

3.7 Hydraulic fluid flow rate

With the selection of the motor, ballscrew and diameters of the input and output pistons, the expected maximum flow rate of the hydraulic fluid through the closed hydrostatic circuit's flow channels and bypass can be computed.

The maximum linear speed of the input assembly's ballscrew nut and input pistons $\dot{x}_{ip,max}$ are a product of the gear ratio, $\frac{N_b}{N_e}$, ballscrew lead, L and maximum electric motor rotational speed, $\dot{\theta}_{m,max}$

$$\dot{x}_{ip,max} = \frac{1}{N_b/N_e}\dot{\theta}_{m,max}\frac{L}{2\pi} \quad 3\text{-}25$$

Assuming that the input piston's shaft is infinitely stiff and that it moves at the same speed as the ballscrew nut, the fluid flow rate, Q_{max} generated by the input pistons as they are driven by the ballscrew nut is related to the nut's linear velocity, $\dot{x}_{ip,max}$ by the total area of the twin pistons, $2A_{ip}$

$$Q_{max} = 2A_{ip}\dot{x}_{ip,max} \quad 3\text{-}26$$

While the maximum flow rate within the closed hydrostatic circuit was determined by considering the input pistons, it would also apply if the output piston was driven at the maximum speed at the MEHA's output as would be the case when it operates in the bypass mode.

3.8 Flow resistance of closed hydrostatic circuit channels

Having determined the maximum flow rate that can be generated by the input and output pistons of the MEHA, the pressure difference across the flow channels as fluid is driven between the input and output pistons or through the bypass valve can be estimated. This

aids the size minimisation of the flow channels connecting the bypass valve, input and output pistons while also minimising the pressure difference across them at the maximum flow rate within the closed hydrostatic circuit.

In the case where one of the EMA develops a fault and the bypass valve is opened, flow between the output piston's chambers goes through the bypass channel to decouple it from the input piston's chambers. In this case, the output piston essentially becomes a damped piston that is driven by the operational MEHA, with the pressure difference across it generated by the flow resistance of the bypass channel. The flow and pressure across the bypass channel has to be analysed to ensure that the size of the bypass channel does not cause the failed MEHA to exert an excessive load on the operational MEHA. While a larger bypass channel will minimise the flow resistance across it, the size of the bypass channel is limited by the geometrical constraints of the MEHA and the need to reduce the load on the bypass valve actuator.

For the purpose of sizing, the bypass channel can initially be assumed to be a circular pipe through which the hydraulic fluid flows. Since the flow generated by the motion of the input piston is expected to be low with the high pressure within the closed hydrostatic circuit, the speed of the flow that goes through the bypass channel is also expected to be low and thus, flow through the bypass channel will be laminar. As a result, the pressure difference across the bypass channel can be predicted by the pipe flow equation.

The velocity of the flow through the bypass channel, $\mathrm{v_{by}}$, is given by the cross-sectional area of the bypass channel, $\mathrm{A_{by}}$ and the maximum flow rate produced by the motion of the output piston, $\mathrm{Q_{max}}$

$$A_{by} = \frac{1}{4}\pi d_{by}^2 \quad 3\text{-}27$$

$$v_{by} = \frac{Q_{max}}{A_{by}} \quad 3\text{-}28$$

Adapting the textbook pipe flow equation [60], the pressure across the bypass channel $(P_A - P_B)$ can be related to the flow velocity within it.

$$P_A - P_B = \frac{32\mu l_{by}}{d_{by}^2} v_{by} \quad 3\text{-}29$$

Substituting Equations 3-27 and 3-28 into Equation 3-29,

$$P_A - P_B = \frac{32\mu l_{by}}{d_{by}^2} \frac{Q_{max}}{\frac{1}{4}\pi d_{by}^2} = \frac{128\mu l_{by}}{\pi d_{by}^4} Q_{max} \quad 3\text{-}30$$

The length of the bypass channe,l l_{by} is mainly constraint by the design of the bypass and output piston assemblies, while Q_{max} will be fixed by the design of the input and output pistons. The viscosity of the fluid, μ is the result of the choice of hydraulic oil. That leaves the selection of the bypass channel diameter, d_{by} which will determine the pressure across it for a given, Q_{max}.

The channels connecting the input and output pistons are similarly a resistance to the flow between the pistons during normal operation of the MEHA when hydraulic fluid will flow between the input and output pistons through channels within the closed hydrostatic circuit to transmit mechanical power from the electric motor to the UAV's control surface. With the same derivation from pipe flow equations, the equation for the flow between the input and output pistons through connecting channels of length, l_c and diameter, d_c can be derived to be

$$P_{A,ip} - P_{A,o} = \frac{128\mu l_c}{\pi d_c^4} Q_{max} \quad 3\text{-}31$$

An important distinction from the equation for the flow through the bypass channel is that the pressure difference across the channels connecting the input, $P_{A,ip}$ and output pistons, $P_{A,o}$ is on the same side of the output piston. During normal operation of the MEHA when one side of the output piston is at high pressure and the other side is at the accumulator pressure, the pressure on one side of the output piston may peak to damaging levels while the pressure on the other side of output piston drop to cavitation levels. An initial sizing of the channel diameter, d_c given a certain length, l_c is thus needed to ensure that the pressure difference needed to push the flow through the connecting channels does not cause damaging pressure peaks or cavitation. This pressure difference will be additional to that needed to actuate the UAV's control surface at the MEHA's output so it should also be minimised to keep within the torque capacity of the electric motor.

3.9 Accumulator sizing

The sizing of the accumulator within the MEHA's output assembly remains. It has to be sized to be able to replenish minimum operating temperature of the MEHA is reached. The total volume of hydraulic fluid in the hydrostatic circuits should be considered but during the initial design stage when the connecting channels have not been designed, only the major fluid volumes can be considered. For the purpose of sizing the accumulator, the minor fluid volumes such as those in the connecting channels can be considered negligible.

In the input assembly, the input piston chambers are the major fluid volumes and their total volume can be calculated by taking the product of the total area of the input pistons, $2A_{ip}$ and their maximum strokes $2x_{ip,max}$

$$V_{ip} = 2x_{ip,max}(2A_{ip}) = 4A_{ip}x_{ip,max} \quad 3\text{-}32$$

For the output assembly, the output piston chambers are the major fluid volumes. Similarly, their volumes can be computed by taking product of the output piston's area exposed to pressure of the closed hydrostatic circuits, $\left(\frac{\pi}{4}d_p^2 - \frac{\pi}{4}d_{shaft}^2\right)$ and its stroke length, x_{max}

$$V = 2\left(\frac{\pi}{4}d_p^2 - \frac{\pi}{4}d_{shaft}^2\right)x_{max} = \frac{\pi}{2}\left(d_p^2 - d_{shaft}^2\right)x_{max} \quad 3\text{-}33$$

With the maximum decrease in the MEHA's operating temperature, $(T_0 - T_{min})$, the change in the volume of the hydraulic fluid ΔV is a function of its coefficient of thermal expansion α_v and the total volume of hydraulic fluid in the closed hydrostatic circuits $(V + V_{ip})$

$$\Delta V = \alpha_v(V + V_{ip})(T_0 - T_{min}) \quad 3\text{-}34$$

The required stroke length, $x_{a,max}$of the accumulator piston and that of the accumulator spring is a function of the accumulator piston's area, A_{ac} and a safety factor, s_a added to ensure that the closed hydrostatic circuits will remain pressurised even when operating at the MEHA's minimum operating temperature

$$x_{a,max} = s_a\frac{\Delta V}{A_{ac}} \quad 3\text{-}35$$

The accumulator pressure, P_a is developed by the force exerted by its spring with stiffness, k_{ac} acting on the piston's cross sectional area, A_{ac}

$$P_a = \frac{k_{ac}(x_{a,max}+x_{a0})}{A_{ac}} \quad 3\text{-}36$$

A rise in the MEHA's operating temperature will cause thermal expansion of the hydraulic fluid within the closed hydrostatic circuit. This results in an increase in pressure within the

circuit, causing excess fluid to flow into the accumulator circuit and eventually limiting the pressure increase to that exerted by the accumulator spring. The maximum accumulator pressure, $\mathrm{P_{a,max}}$ will be developed at the maximum operating temperature of the MEHA, $\mathrm{T_{max}}$

$$\mathrm{P_{a,max}} = \frac{\mathrm{k_{ac}}}{\mathrm{A_{ac}}}\left(\mathrm{x_{a,max}} + \mathrm{x_{a0}} + \frac{\alpha_v(\mathrm{V}+\mathrm{V_{ip}})(\mathrm{T_0}-\mathrm{T_{max}})}{\mathrm{A_{ac}}}\right) \quad 3\text{-}37$$

While the minimum accumulator pressure, $\mathrm{P_{a,min}}$ will be developed at the minimum operating temperature of the MEHA, $\mathrm{T_{min}}$

$$\mathrm{P_{a,min}} = \frac{\mathrm{k_{ac}}}{\mathrm{A_{ac}}}\left(\mathrm{x_{a,max}} + \mathrm{x_{a0}} - \frac{\alpha_v(\mathrm{V}+\mathrm{V_{ip}})(\mathrm{T_0}-\mathrm{T_{min}})}{\mathrm{A_{ac}}}\right) \quad 3\text{-}38$$

3.10 Lever arm strength

The output piston of the MEHA's output assembly converts the pressure difference within the closed hydrostatic circuit into a linear force which in turn translates into a torque at the MEHA's output through the lever arm. This force exerts a bending stress on the lever arm which has to be within the yield strength of the lever arm's material. The stress in the lever arm, σ_l due to the output piston's force is a function of the maximum force output from the MEHA's output piston, $\mathrm{F_{max}}$ and the chosen lever arm length, l_l, as well as the lever arm's cross section's height, $\mathrm{h_l}$ and breadth, $\mathrm{b_l}$

$$\sigma_\mathrm{l} = \frac{(\mathrm{F_{max}}\mathrm{l_l})\mathrm{l_l}}{\mathrm{b_l}\mathrm{h_l}/12} \quad 3\text{-}39$$

3.11 MEHA Bandwidth

Like electro-mechanical actuators, the bandwidth of the MEHA can be obtained from

$$f_{-3dB} = 12\pi\tau \quad 2\text{-}11$$

For the MEHA, the mechanical time constant can be found using an expanded version of Equation 2-12 after the detailed design of the prototype is completed. This requires the computation of the equivalent rotational inertia of the MEHA's components as seen at the electric motor. For the gear train's total rotational inertia, J_g, the rotational inertias of the idler gears, J_i and ballscrew shaft gear, J_{bg} has to be converted with their respective gear ratios and summed with the rotational inertia of the electric motor shaft gear, J_m,

$$J_g = J_m + \left(\frac{N_e}{N_i}\right)^2 (J_i) + \left(\frac{N_e}{N_b}\right)^2 (J_{bg}) \quad 3\text{-}40$$

The equivalent rotational inertia of the ballscrew shaft at the electric motor, J_b can be found from the ballscrew shaft's rotational inertia, J_{bs} and mass of the ballscrew nut, m_{nut} using the gear train's teeth ratio, $\frac{N_e}{N_b}$ and ballscrew lead, L

$$J_b = \left(\frac{N_e}{N_b}\right)^2 J_{bs} + \left(\frac{N_e}{N_b}\right)^2 m_{nut} L^2 \quad 3\text{-}41$$

Similar to the mass of the ballscrew nut, the equivalent rotational inertia of the mass of the input pistons, m_{ip} can be derived from the gear train's teeth ratio, $\frac{N_e}{N_b}$ and ballscrew lead, L

$$J_{ip} = \left(\frac{N_e}{N_b}\right)^2 m_{ip} L^2 \quad 3\text{-}42$$

From the MEHA's output, the mass of the output piston, m is converted to an equivalent rotational inertia at the electric motor, J using the gear train's teeth ratio, $\frac{N_e}{N_b}$, ballscrew lead, L and ratio of output and input piston areas, $\frac{2A_{ip}}{A}$,

$$J = mL^2 \left(\frac{N_e}{N_b}\right)^2 \left(\frac{2A_{ip}}{A}\right)^2 \quad 3\text{-}43$$

The total rotational inertia of the MEHA's transmission, J_t is then the sum of the various rotational inertias

$$J_t = J_g + J_b + J_{ip} + J \quad 3\text{-}44$$

Together with the load inertia, total reduction ratio and relevant properties of the electric motor, J_t can be used to derive time constant of the MEHA using Equation 2-12.

3.12 MEHA Dynamic model

Dynamic models of the MEHA are important for ensuring that the dynamic performance requirements are met and for predicting the maximum forces and pressures during dynamic operation of the MEHA. In this work, these models are needed for the study of the effects of the close hydrostatic circuit on the performance of MEHA. Work has been done to model EHAs both linearly [20] and non-linearly [61, 62]. For this work, the MEHA was modelled in MATLAB Simulink. A simplified model of the MEHA was first developed in Section 3.3 to study the optimisation of the MEHA's total reduction ratio. In this section, that model is developed further to include the effects of non-linearities on the MEHA's performance.

In Section 3.3, the dynamic models of the electric motor's subsystems were developed for the optimisation study for the MEHA's total reduction ratio (see Figure 3-7, Figure 3-8 and Figure 3-9). For the MEHA non-linear dynamic model developed in this section, these models are grouped under the electric motor subsystem block whose schematic is shown in Figure 3-11.

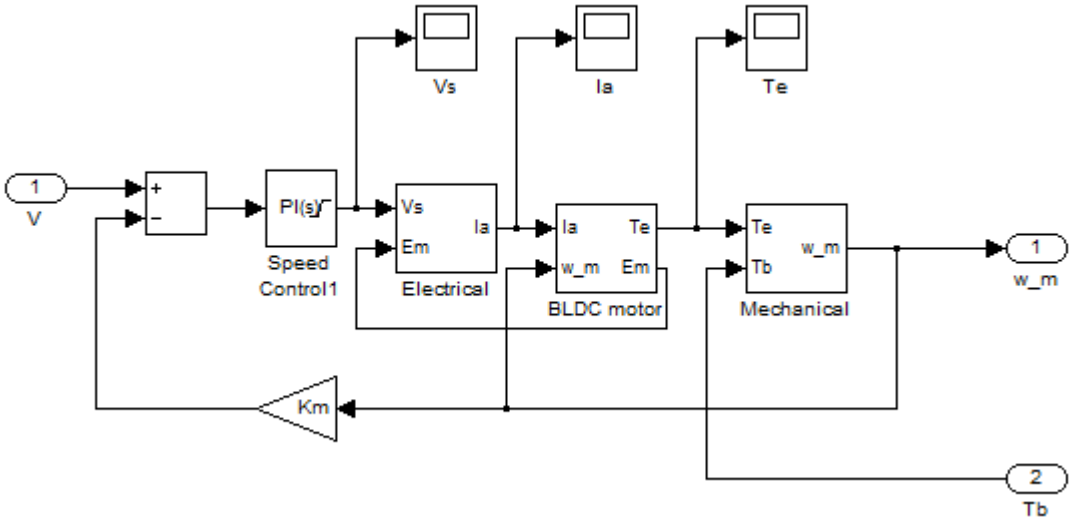

Figure 3-11: Dynamic model of the electric motor subsystem

In the dynamic model of the MEHA's input assembly subsystem (Figure 3-12), the output from the electric motor subsystem drives the ballscrew shaft through the gear train's ratio, $\frac{N_b}{N_e}$ which is represented by the gain value Gr in the model. Thus the motor's rotational speed, $\dot{\theta}_m$ is reduced by the gear ratio to the rotational speed at the ballscrew shaft, $\dot{\theta}_b$, while the load torque at the ballscrew shaft, T_b is reduced by the gear ratio to the load torque at the motor, T_e

$$\dot{\theta}_b = \dot{\theta}_m / \left(\frac{N_b}{N_e}\right) = \dot{\theta}_m / Gr \qquad 3\text{-}45$$

$$T_e = T_b / \left(\frac{N_b}{N_e}\right) = T_b / Gr \qquad 3\text{-}46$$

The ballscrew converts the rotational speed at its shaft, $\dot{\theta}_b$ into a linear speed at its nut, v_b while the load at the nut is similarly translated in to a load torque at the ballscrew shaft through its lead, L

$$v_b = L\dot{\theta}_b \qquad 3\text{-}47$$

$$T_b = \frac{L}{2\pi} F_b \qquad 3\text{-}48$$

The input pistons to the closed hydrostatic circuit are driven by the ballscrew nut, producing a flow rate, Q which relates to the speed of the pistons v_b by their total cross sectional area, $2A_{ip}$, while the pressure difference across the ballscrew nut due to the load, $(P_A - P_B)$ is seen as a load, F_b at the ballscrew nut through the same area

$$Q = 2A_{ip} v_b \qquad 3\text{-}49$$

$$F_b = 2A_{ip}(P_A - P_B) \qquad 3\text{-}50$$

In the dynamic model of the input piston assembly, the gear ratio, Gr, ballscrew lead, L and input piston area, A_{ip} are modelled as gain blocks. The pressure difference needed to drive the flow through the flow resistance of the channels of the closed hydrostatic circuit is in addition to the pressure difference due to the load and is modelled as an output from a polynomial function of the flow rate. The friction force acting on the pistons are added to the linear force on the ballscrew nut. The schematic of the input assembly subsystem is shown in Figure 3-12.

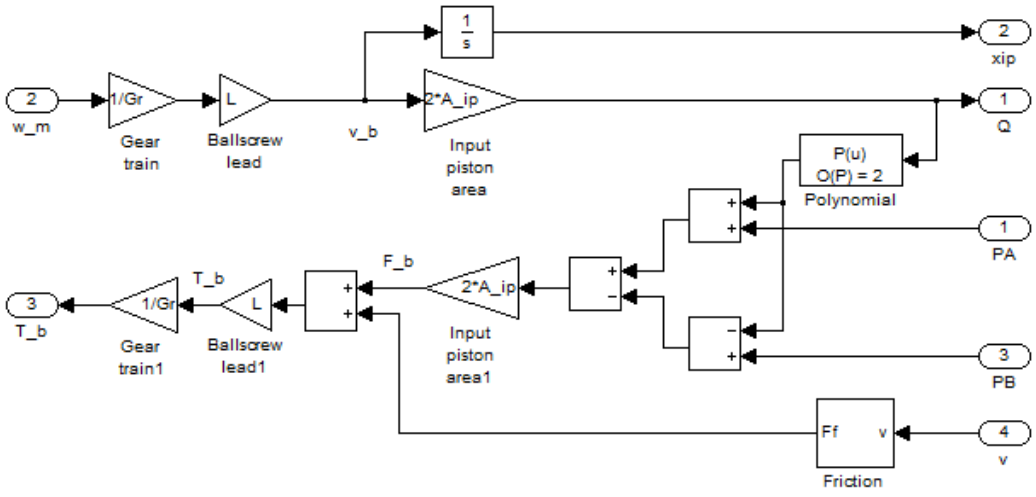

Figure 3-12: Dynamic model of the input piston assembly subsystem

The friction force module (Figure 3-13) adds the effects of the static and kinetic friction of the MEHA's pistons into the dynamic model. The kinetic friction, F_c and static friction, F_s factors are obtained experimentally from Section 6.2. The magnitude of the static friction factor includes contribution from the kinetic friction, thus the difference between the two factors has to be taken to remove this contribution. With the exponential function, the change in the direction of static friction can be approximated [61]. The friction force, F_f as a function of the velocity, v can thus be expressed as

$$F_f = (F_c + (F_s - F_c)e^{10000}|v|)\text{sign}(v) \qquad 3\text{-}51$$

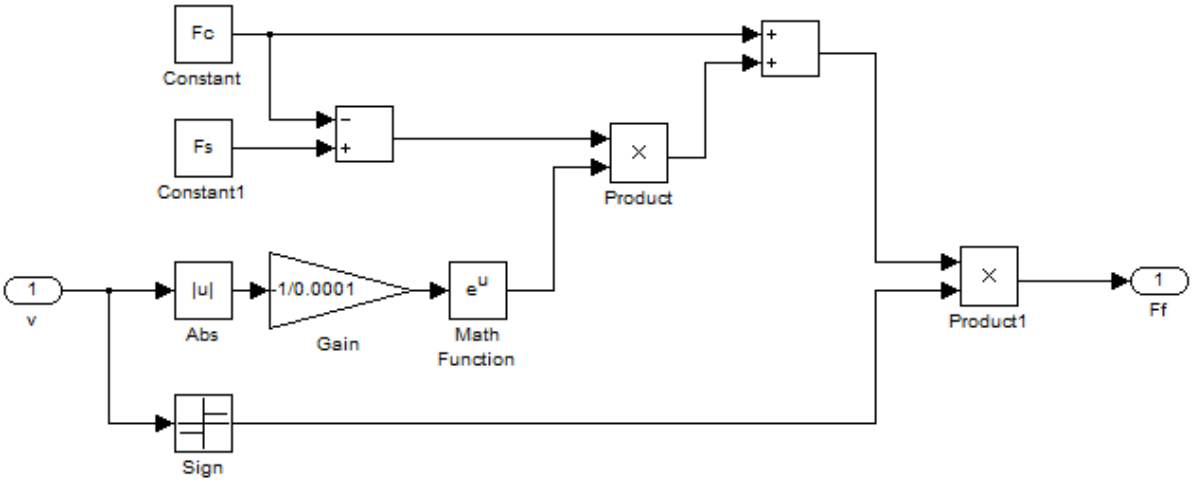

Figure 3-13: Friction force model

The refeeding subsystem in the MEHA's non-linear dynamic model (Figure 3-14) simulates the effects of the spring accumulator (Figure 3-15) on the flow and pressure within the closed hydrostatic circuit. If the pressure within the circuit on one side of the piston is more than the accumulator pressure, Pac, the checkvalve is closed and the flow from the input piston assembly passes to the output piston assembly. However, when the pressure within the circuit is less than the accumulator pressure, the checkvalve opens and flow from the spring accumulator adds to that between both piston assemblies to keep the pressure at the accumulator pressure. Leakage from the closed hydrostatic circuit across the checkvalves

into the accumulator circuit is accounted for by Q_{el}. The net flow into the accumulator circuit, Q_{ac} changes the initial compression of the spring, x_{aci} and the pressure within the accumulator circuit varies with spring compression through the stiffness of the accumulator spring, k_{ac} and the cross-sectional area of the accumulator piston, A_{ac}.

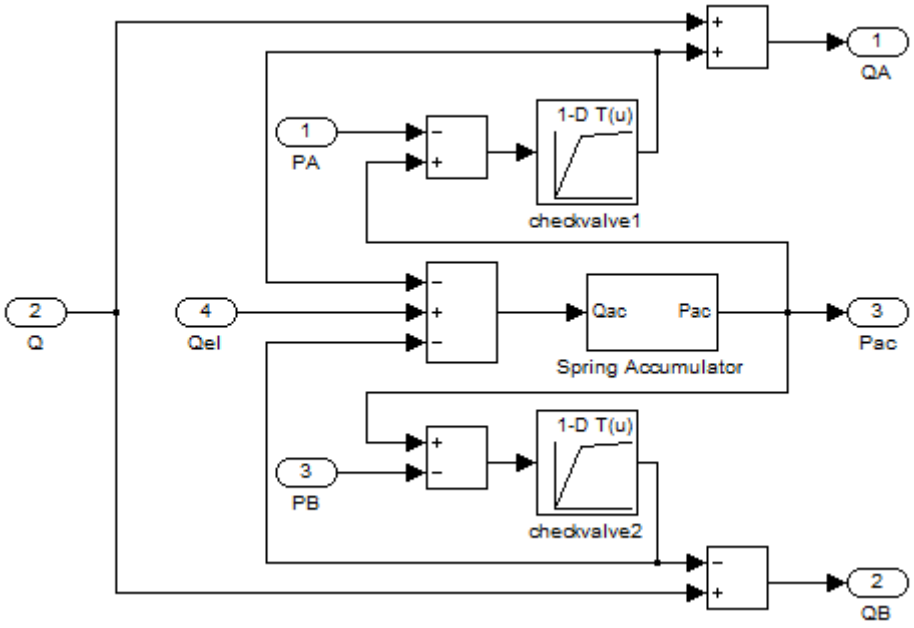

Figure 3-14: Dynamic model of the refeeding circuit subsystem

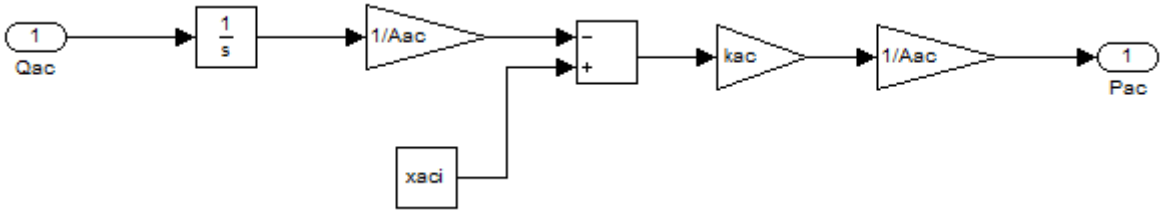

Figure 3-15: Dynamic model of the spring accumulator subsystem

The output assembly subsystem in the dynamic model takes the flow from the input piston assembly subsystem through the refeeding circuit subsystem, Q_A and Q_B, to compute the pressure within the opposing sides of the closed hydrostatic circuit, P_A and P_B, with the motion of the output piston and the bulk modulus of the hydraulic fluid, B_0. The flow within the output piston due to the motion of the piston, v, is proportional to the cross-sectional area of the piston, A

$$Q_{op} = Av \tag{3-52}$$

The leakage across the output piston, Q_{il}, is a function of the pressure across the piston and the internal leakage coefficient, C_{lossi}

$$Q_{il} = C_{lossi}(P_A - P_B) \tag{3-53}$$

Leakage from either side of the closed hydrostatic circuit across the checkvalves into the accumulator circuit is similarly a function of the external leakage coefficient, C_{losse}, and the accumulator pressure, P_{ac}

$$Q_{el} = C_{losse}(P_A - P_{ac}) + C_{losse}(P_B - P_{ac}) \tag{3-54}$$

Pressure within both sides of the closed hydrostatic circuit can be derived from the net flow into the respective output piston chambers, the instantaneous volume in each chamber and the bulk modulus of the hydraulic fluid, B_o

$$P_A = \frac{1}{s}\frac{B_o}{V_o + Ax - 2A_{ip}x_{ip}}(Q_A - Av - C_{losse}(P_A - P_{ac}) - Q_{il}) \tag{3-55}$$

$$P_B = \frac{1}{s}\frac{B_o}{V_o - Ax + 2A_{ip}x_{ip}}(-Q_B + Av - C_{losse}(P_A - P_{ac}) + Q_{il}) \tag{3-56}$$

The pressure difference, $(P_A - P_B)$, acts across the cross-sectional area of the output piston, A, to produce a force at the MEHA's output

$$F = (P_A - P_B)A \tag{3-57}$$

A schematic of the output piston assembly subsystem incorporating Equations 3-51 to 3-56 is shown in Figure 3-16.

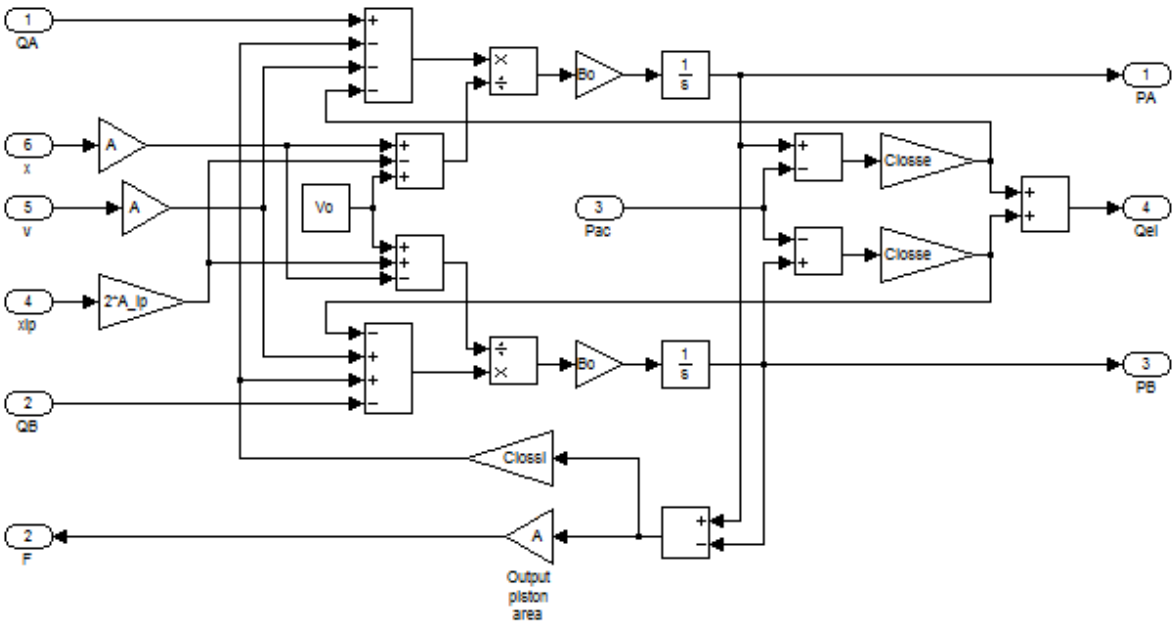

Figure 3-16: Dynamic model of the output assembly subsystem

In the case where the MEHA operates in tandem with other identical MEHA in the 'active-active' mode, the forces, F from both MEHAs are summed to drive the load inertia, I against the aerodynamic load, F_L and their own mass inertias, M through the lever arm of length, l_l

$$F + F - F_L = \left(M + M + \frac{I}{l_l^2}\right)\dot{v} \qquad 3\text{-}58$$

Figure 3-18 shows the model of a single MEHA while Figure 3-19 shows the schematic of the MEHA dynamic model with both MEHAs operating in tandem to drive the load at the output.

In the other case, one of the MEHA is operating in the damped mode after its output assembly has been decoupled from the input assembly by allowing the flow within its closed hydrostatic circuit to flow through the bypass assembly. The active MEHA then has to drive this damped MEHA in addition to the existing load and inertias. The closed hydrostatic circuit of the damped MEHA is not affected by the position of the input pistons since the

flow is allowed to go through the bypass, thus Equations 3-54 and 3-55 can be modified by removing the term $A_{ip}x_{ip}$ to become

$$P_A = \frac{1}{s}\frac{B_o}{V_o+Ax}(Q_A - Av - C_{losse}(P_A - P_{ac}) - Q_{il}) \quad 3\text{-}59$$

$$P_B = \frac{1}{s}\frac{B_o}{V_o-Ax}(-Q_B + Av - C_{losse}(P_A - P_{ac}) + Q_{il}) \quad 3\text{-}60$$

Adapting from Equation 3-30, the pressure difference $(P_A - P_B)$ across the flow resistance, K_{by} formed by the bypass valve drives the flow, Q through it

$$P_A - P_B = K_{by}Q \quad 3\text{-}61$$

Similar to the MEHA in active mode, the flow through the bypass valve is fed through the refeeding circuit block (see Figure 3-14) of the MEHA in damped mode to account for the effects of the spring accumulator on the flow and pressure within its closed hydrostatic circuit. The dynamic model of the bypass assembly is shown in Figure 3-17, while the schematic of the model with the MEHAs operating in 'active-damped' mode is presented in Figure 3-20.

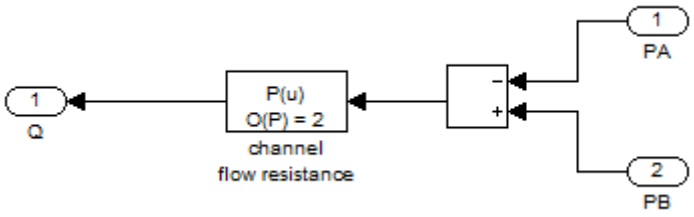

Figure 3-17: Dynamic model of the bypass assembly

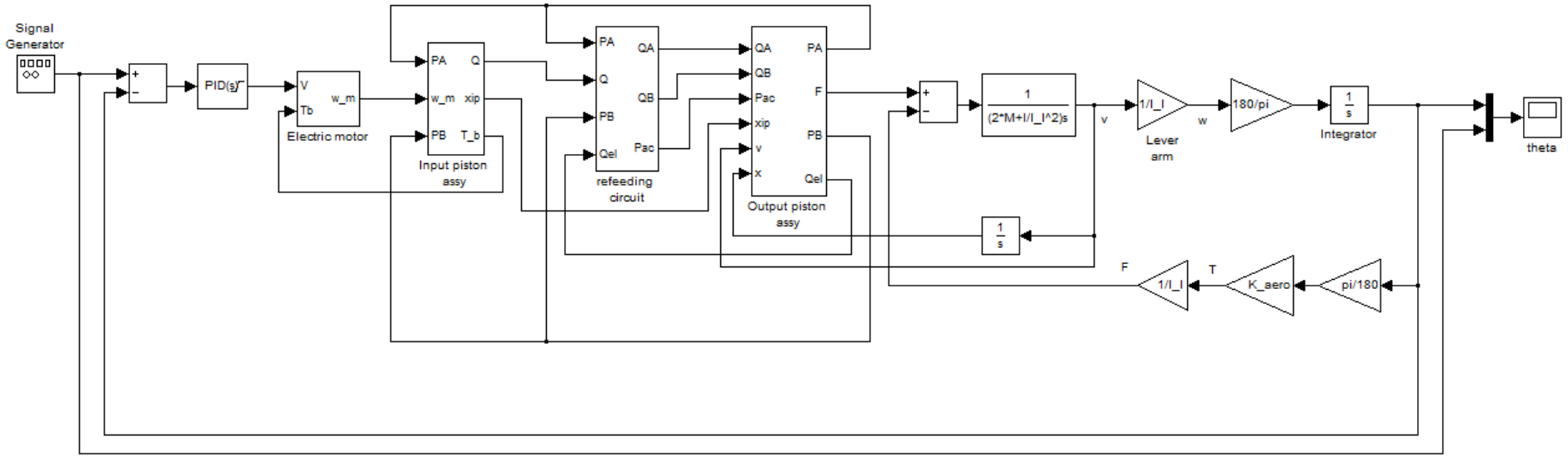

Figure 3-18: MEHA non-linear dynamic model

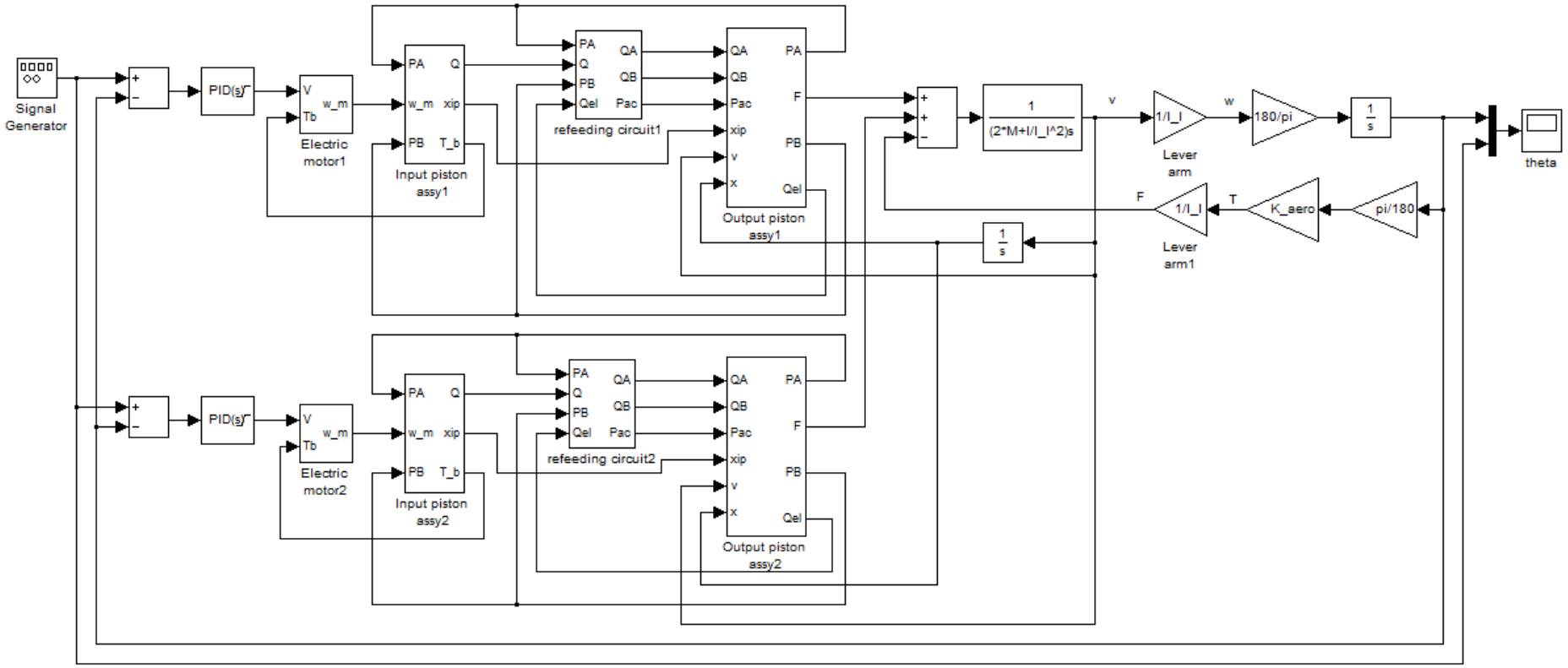

Figure 3-19: Dynamic model of the MEHAs operating in tandem 'active-active' mode

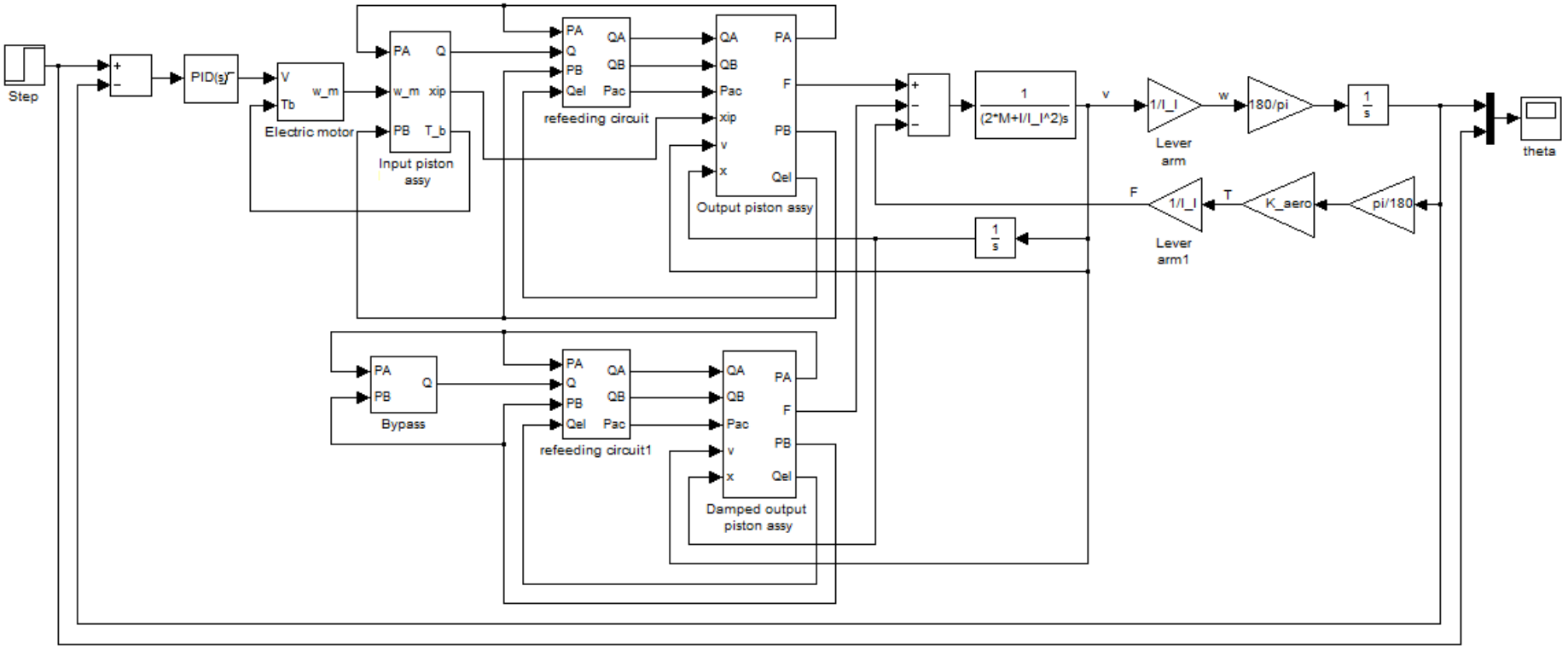

Figure 3-20: Dynamic model of the MEHAs operating in 'active-damped' mode with one MEHA in damped mode

4. PROTOTYPE DESIGN

This chapter reports the design of the MEHA prototype. It begins with the selection of the motor and the optimisation the MEHA's total reduction ratio. This is followed by the selection of the gear train and ballscrew parameters. Next is the design of the components that form the closed hydrostatic circuit, followed by the design of accumulator. Lastly this chapter ends with material selection for the components of the MEHA.

4.1 Motor selection

The prototype design process begins with the selection of a suitable electric motor. An electric motor with a peak power output that is able to supply the peak power required at the MEHA output attenuated by the assumed transmission efficiency was selected. An efficiency of 80% was assumed and the Faulhaber 2232BX4 brushless DC motor was chosen.

Table 4-1: Comparison of load requirements and electric motor capability

	MEHA torque	**BLDC electric motor torque**
Stall	25Nm	0.094Nm (stall torque at 3A)
	MEHA slew rate	**BLDC speed**
No load	160°/s	53340°/s (8890rpm)
Peak power output	17.5W	21.9W

4.2 MEHA total reduction ratio

Optimisation of the reduction ratio is required to balance the maximum voltage and current that the MEHA consumes while driving the benchmark load at the specified load case of ±20° at 3Hz (Table 2-1). This optimisation was performed using the simplified dynamic model developed in Section 3.3 (see Figure 3-10).

Table 4-2: Results from optimisation of total reduction ratio

Reduction ratio	Max V_s	Max I_a	Max T_e	Max ω_m
70	30	3	0.094	4500
80	28.6	1.88	0.059	5020
90	27.65	1.64	0.051	5670
100	27.2	1.43	0.045	6265
110	28.03	1.27	0.04	6928
120	29.96	1.12	0.0352	7555
130	30	1.18	0.0371	8170
140	30	2.4	0.0752	8760

From Table 4-2, it can be seen that as the total reduction ratio is increased, the maximum current drawn the electric motor is reduced. The maximum voltage required to drive the motor decreases to a minimum before increasing with the reduction ratio. This trend continues to the point where the maximum voltage required reaches the practical limit of the motor's controller. Since voltage cannot be increased further, the control loop attempts to increase the motor's speed by increasing the peak current.

In the interest of minimising the heat generated in the motor and its controller, the reduction ratio that gives the lowest current consumption at the motor should be chosen. However, the EMA benchmark has a constraint of 28V while driving the benchmark load, so the reduction ratio of 110 is chosen as the optimum balance between voltage and current consumption. The margin between the predicted maximum current drawn by the motor and the controller limit will account for any additional friction, damping or inertia loads.

4.3 Ballscrew selection

The total reduction ratio is dependent on a combination of parameters which have to be chosen with consideration for the constraints of the MEHA. The equation for the total reduction ratio has been derived to be

$$\mathrm{N} = 2\pi \frac{\mathrm{A}}{\mathrm{A_{ip}}} \frac{\mathrm{N_b}}{\mathrm{N_e}} \frac{l_l}{\mathrm{L}} \sin\theta \qquad 3\text{-}2$$

The lead of the ballscrew is chosen together with a gear ratio between the electric motor and ballscrew shaft through a parametric study that aims to minimise the dimensions of the MEHA while keeping within the load capacity of the ballscrew. For the MEHA prototype with the chosen electric motor, the maximum force at the ballscrew nut is generated when the stall torque of 0.094Nm is output at the electric motor.

Table 4-3: Parametric study for input piston assembly

Lead (mm)	N_b/N_e	F_b (N)	Nominal $\pm x_{ip,max}$ (mm)
0.5	1.5	1772	2.04
0.5	1	1181	3.06
0.5	0.5	591	6.11
1	2	1181	3.06
1	1.5	886	4.07
1	1	591	6.11
1	0.5	295	12.22
1.5	2	787	4.58
1.5	1.5	591	6.11
1.5	1	394	9.17
1.5	0.5	197	18.33
2	2	591	6.11
2	1.5	443	8.15
2	1	295	12.22
2	0.5	148	24.44

Generally, increasing the ballscrew's lead decreases the force output on its nut, while increasing its maximum velocity and the required stroke length. Decreasing the gear ratio has the same effect. The load capacity of the ballscrew and supporting bearings places a constraint on the force that the ballscrew can exert. In order to minimise the MEHA's size, the smallest lead and largest gear ratio within this constraint should be chosen. As a result, a ballscrew lead of 1mm and a gear ratio of 2 were chosen for the MEHA prototype in this study. The KSS SG0601 ballscrew with 1mm lead with a rated static load of 1200N and dynamic load of 680N was selected. Margin of safety of the static load rating over the expected maximum axial force

$$\text{MOS} = \frac{\text{rated static load}}{F_{b,max}} - 1 = \frac{1200}{1181} - 1 = 0.16 \qquad 4\text{-}1$$

Maximum output speed of selected motor in Section 4.1 is 8890rpm. With the chosen gear ratio of 2, the maximum rotational speed of ballscrew shaft will be 4445rpm. This exceeds the ballscrew manufacturer's rotational speed limit of 4000rpm, thus requiring a limit on the maximum speed of the electric motor during operation. In addition, while the maximum input piston stroke for the selected ballscrew lead and gear ratio will nominally be 3.06mm, the MEHA prototype will be designed with a greater maximum input piston stroke of 5mm to allow additional volume for the flow of hydraulic fluid within the piston bores.

4.4 Gear strength

In Section 4.3, the gear ratio $\frac{N_b}{N_e}$ of 2 was selected in the parametric study in Table 4-3. Choosing the following parameters for the gear train:

- Gear module, $m_g = 0.5$
- Number of gear teeth at electric motor gear, $N_e = 12$
- Number of gear teeth at ballscrew shaft gear, $N_b = 24$
- Number of gear teeth on idler gear, $N_i = 19$

The contact ratios between the gears on the electric motor and ballscrew shafts and their adjacent idler gears can be calculated using Equations 3-17 and 3-18 respectively,

$$\varepsilon_{\gamma,e} = \frac{\sqrt{\left(\frac{d_e}{2}+1.25m_g\right)^2-\left(\frac{d_e}{2}-m_g\right)^2}+\sqrt{\left(\frac{d_i}{2}+1.25m_g\right)^2-\left(\frac{d_i}{2}-m_g\right)^2}-\frac{1}{2}(d_e+d_i)\sin 20°}{\pi m_g \cos 20°} = 2.2 \qquad 4\text{-}2$$

$$\varepsilon_{\gamma,b} = \frac{\sqrt{\left(\frac{d_b}{2}+1.25m_g\right)^2-\left(\frac{d_b}{2}-m_g\right)^2}+\sqrt{\left(\frac{d_i}{2}+1.25m_g\right)^2-\left(\frac{d_i}{2}-m_g\right)^2}-\frac{1}{2}(d_i+d_b)\sin 20°}{\pi m_g \cos 20°} = 3.2 \qquad 4\text{-}3$$

The high contact ratios between the gears indicate that the engagement and disengagement of the gear teeth will be smooth as they transmit mechanical power between the electric motor and ballscrew.

From Section 4.1, the maximum torque output that the selected motor can provide is 0.094Nm. The maximum force at the gear teeth contact, F_{gear} can then be determined with Equation 3-20

$$\mathrm{F}_{gear} = \frac{\mathrm{T_{e,max}}}{\mathrm{d_e}/2} = 15.7\mathrm{N} \qquad 4\text{-}4$$

Table 4-4: Factors used in calculation of gear strength

Geometry factor, $\mathrm{K_J}$	0.39
Application factor, $\mathrm{K_a}$	2
Size factor, $\mathrm{K_s}$	1
Load distribution factor, $\mathrm{K_m}$	1
Rim thickness factor, $\mathrm{K_B}$	1
Dynamic factor, $\mathrm{K_v}$	0.76

This can then be used in Equation 3-19 to check on the bending stress at the gear contacts

$$\frac{\mathrm{F}_{gear}}{\mathrm{m_g w}} \frac{\mathrm{K_a K_s K_{ld} K_B}}{\mathrm{K_v K_J}} = 70.6\mathrm{MPa} \qquad 4\text{-}5$$

This is well within the tensile strength of 1000MPa for steel.

4.5 Ballscrew bearing selection

The ballscrew shaft in the MEHA's input assembly is supported on bearings which have to withstand the force exerted by the ballscrew nut on the input pistons of the closed hydrostatic circuit with a positive margin of safety. The peak force on the ballscrew shaft was determined in Section 4.3 to be 1181N. For the purpose of bearing selection, this peak force is converted to a mean force on the bearing by multiplying it with a factor of 0.65. Since there will be negligible radial forces on the ballscrew shaft, the axial force on the

bearing from the ballscrew axial load determined in Section 4.3 is converted to an equivalent radial force by

$$0.5 \times (0.65 \times 1181) = 384\text{N} \quad \text{4-6}$$

The NTN 686 was selected as the bearing supporting the ballscrew shaft. With its rated static torque of 440N, the Margin of Safety (MOS) over the equivalent axial force on the bearing will be

$$\text{MOS} = \frac{440}{384} - 1 = 0.14 \quad \text{4-7}$$

The positive MOS of the bearing's load rating over the equivalent load on it provides a safety factor to reduce the chance of unexpected premature failure. It also shows that the power density achieved with the MEHA prototype in this study is realistic.

4.6 Piston sizing

In order to minimise the size of the MEHA, the input piston diameter should be minimised. The commercial availability of small o-ring seals limits the smallest input piston diameter to 6mm. For the twin input pistons on one side of the ballscrew nut, the maximum pressure in the closed hydrostatic circuit can be found by applying Equation 3-21 with the expected maximum force $\mathrm{F_{b,max}}$ of 1181N on the ballscrew found in Section 4.3

$$\Delta\mathrm{P_{max}} = \frac{\mathrm{F_{b,max}}}{\mathrm{A_{ip}}} = 20.9\text{MPa} \quad \text{4-8}$$

From Equation 3-23, it can be seen that for a required torque at the MEHA's output and a given pressure difference across the output piston, the choices of an output piston diameter and a lever arm length at the MEHA's output are related, and must be considered together. Due to the need for a minimum output bearing diameter as well as considering the load

shaft and lever arm geometries, a minimum lever arm length of 20mm is required. For the prototype in this study, a stall torque output of 0.094Nm at the electric motor chosen in Section 4.1 and a total reduction ratio of 110 selected in Section 4.2 produces a stall torque of 10.34Nm at the output of the MEHA. The different combinations of output arm length, output piston and shaft diameters for a hydrostatic pressure of 20.9MPa to produce an output torque of 10.34Nm are computed in the following table together with the required nominal stroke length of the output piston for each combination.

The panel of piston and shaft diameters are selected based on the commercial availability of o-ring seals. Choosing the optimum combination of the output piston dimensions is done by minimising the goal function

$$\mathrm{d_p^2} \times \mathrm{x} \qquad 4\text{-}9$$

Table 4-5: Parametric study of output piston and lever arm

$\mathbf{d_p}$ (mm)	$\mathbf{d_{shaft}}$ (mm)	A (mm^2)	Force (N)	l_l (mm)	Nominal $\pm$x (mm)	Goal function
6	3	21.21	443.20	23.33	8.49	306
6	3.5	18.65	389.85	26.52	9.65	348
6.5	4	20.62	430.89	24.00	8.73	369
7	4.5	22.58	471.93	21.91	7.97	391
6	4	15.71	328.30	31.50	11.46	413
6.5	4.5	17.28	361.13	28.63	10.42	440
7	5	18.85	393.96	26.25	9.55	468
7.5	5.5	20.42	426.79	24.23	8.82	496
6	4.5	12.37	258.53	39.99	14.56	524
6.5	5	13.55	283.16	36.52	13.29	562
7	5.5	14.73	307.78	33.60	12.23	599
7.5	6	15.90	332.40	31.11	11.32	637
6	5	8.64	180.56	57.27	20.84	750
6.5	5.5	9.42	196.98	52.49	19.11	807
7	6	10.21	213.39	48.46	17.64	864
7.5	6.5	11.00	229.81	44.99	16.38	921
6.5	6	4.91	102.59	100.79	36.68	1550
7	6.5	5.30	110.80	93.32	33.97	1664
7.5	7	5.69	119.01	86.89	31.62	1779

This goal function seeks to minimise the overall size of the output piston. From the parametric study, the combination of an output piston diameter of 6mm and output shaft diameter of 3mm with the output lever arm length of 23.35mm gives the minimum goal function and should thus be selected as the parameters for the MEHA's output piston assembly.

During operation of the MEHA, its total reduction ratio changes from the nominal value selected in Section 4.2 as the UAV's control surface is deflected in either direction. Having selected the lever arm length, the range of total reduction ratio can be computed using Equations 3-2 to 3-4 to be 103.9-110. Considering the maximum motor torque output, the MEHA will still be able to deflect the design load at the minimum total reduction ratio.

4.7 Flow rate of hydraulic fluid

Having designed the main components of the MEHA, the maximum flow rate that can be expected to flow between the input and output pistons can be calculated by first considering the maximum linear speed of the ballscrew nut, $\dot{x}_{ip,max}$ with Equation 3-25 using a gear ratio, $\frac{N_b}{N_e}$ of 2 and ballscrew lead, L of 1mm from Section 4.3

$$\dot{x}_{ip,max} = \frac{1}{N_b/N_e}\dot{\theta}_{m,max}\frac{L}{2\pi} = \frac{1}{2}(837.76)\frac{1\times10^{-3}}{2\pi} = 0.067 ms^{-1} \quad 4\text{-}10$$

The maximum motor rotational speed $\dot{\theta}_{m,max}$ is assumed to be limited to 8000rpm or 837.76 rads^{-1} due to the ballscrew shaft's rotational speed limit of 4000rpm. The maximum flow rate from the input pistons to the output pistons is then a product of the twin input pistons' linear speed, $\dot{x}_{ip,max}$ and area, $2A_{ip}$

$$Q_{max} = 2A_{ip}\dot{x}_{ip,max} = 5.655 \times 10^{-5} \times 0.067 = 3.79 \times 10^{-6} m^3 s^{-1} \quad 4\text{-}11$$

The maximum speed of the output piston can be found by

$$\dot{x}_{max} = \frac{Q_{max}}{\frac{\pi}{4}(d^2 - d_{shaft}^2)} = 0.179 ms^{-1} \quad 4\text{-}12$$

4.8 Sizing of closed hydrostatic circuit channels

As explained in Section 3.8, the sizing of the fluid channels connecting the bypass valve, input and output pistons are critical to preventing excessive pressure peaks and drops within the MEHA during both bypass and operational modes. While this is not typically an important consideration for conventional electro-hydraulic actuators, the miniature scale of the MEHA requires that more attention be given to the connecting channels to prevent high pressure gradients across them. The flow resistances of these channels are also needed as inputs into the non-linear dynamic simulation of the MEHA in a later section.

From the design of the MEHA's bypass assembly, the channel length l_{by} was determined to be 147mm. The dynamic viscosity of the hydraulic fluid μ is 0.02784Pa.s with a density of 870kgm^{-3}. In this sizing analysis, it is first assumed that channels connecting the bypass valve are of circular with a constant diameter and that bends in the channels do not cause additional fluid resistance. For a range of different channel diameters, the pressure difference across the bypass valve at maximum MEHA flow speed Q_{max} can be calculated using Equation 3-30.

Table 4-6: Pressure difference across bypass valve for different channel diameters

Channel diameter d_{by} (mm)	Pressure difference across channel (MPa)
1	0.632
2	0.0395
3	0.0078
4	0.0025
5	0.001

A sample calculation using a channel diameter d_{by} of 2mm is

$$P_A - P_B = \frac{128\mu l_{by}}{\pi d_{by}^4} Q_{max} = \frac{128 \times 0.02784 \times 147 \times 10^{-3}}{\pi \times (2 \times 10^{-3})^4} \times 3.77 \times 10^{-6} = 0.0395\text{MPa} \quad 4\text{-}13$$

Compared to the maximum pressure of 20.9MPa expected during MEHA operation calculated in Section 4.6, this pressure difference of 0.0395MPa across the bypass valve is three magnitudes smaller. Thus, a channel diameter of 2mm is selected as the best compromise between the competing demands to minimise pressure difference across the bypass valve and to minimise the size of the channels.

With the selected channel diameter, the incremental pressure that the input pistons have to exert to drive the maximum fluid flow through the closed hydrostatic circuit's channels to the output piston can be calculated using Equation 3-31 with the length of the connecting channel l_c at 47mm from the prototype design

$$P_{A,ip} - P_{A,o} = \frac{128\mu l_c}{\pi d_c^4} Q_{max} = 0.0126\text{MPa} \quad 4\text{-}14$$

It is important to note that the analysis in this section is meant for the initial sizing of the fluid channels. It ignores the effects of bends in the channels and non-circular channels, and is only sufficient for a comparison of different channel diameters. After the detailed design of the MEHA and its closed hydrostatic circuit are completed, numerical analysis will provide a more accurate prediction of the channels' fluid resistance.

4.9 Accumulator sizing

With the selection of the parameters for the MEHA prototype's output piston and input piston assemblies, the accumulator can be sized to replenish the hydraulic fluid within the closed hydrostatic circuits during operation at low temperatures.

For the input assembly with the input piston diameter of 6mm selected in Section 4.6 and the designed maximum stroke of 5mm, the volume of hydraulic fluid in the twin input pistons on both sides of the ballscrew nut can be found using Equation 3-32

$$V_{ip} = 4A_{ip}x_{ip,max} = 5.65 \times 10^{-7}m^3 \quad 4\text{-}15$$

Similarly for the output assembly, the volume of hydraulic fluid in the output piston bores on both sides of the piston with a diameter of 6mm selected from the result of the parametric study in Table 4-5 and a designed stroke of 8.5mm can be calculated using Equation 3-33

$$V = \frac{\pi}{2}\left(d_p^2 - d_{shaft}^2\right)x_{max} = 4.45 \times 10^{-7}m^3 \quad 4\text{-}16$$

With the determination of the approximate volume of hydraulic fluid within the input and output piston assemblies, the change in volume due to thermal contraction while operating at the MEHA's minimum temperature of -40°C can be computed from Equation 3-34 using an hydraulic fluid volumetric thermal expansion coefficient, α_v of 0.0007K^{-1} and an initial temperature, T_0 of 25°C

$$\Delta V = \alpha_v\left(V + V_{ip}\right)(T_0 - T_{min}) = 4.6 \times 10^{-8}m^2 \quad 4\text{-}17$$

The stroke length required of the accumulator piston and spring can then be calculated using Equation 3-35 for the piston area A_a corresponding to a selected piston diameter of 5mm with a safety factor s_a of 3

$$x_{a,max} = s_a\frac{\Delta V}{A_a} = 7mm \quad 4\text{-}18$$

Selecting a spring with a stiffness k_a of 0.49N/mm and with a designed pre-compression of 18mm designed into the accumulator housing, the nominal accumulator pressure P_a can be computed with Equation 3-36

$$P_a = \frac{k_a(x_{a,max}+x_{a0})}{A_a} = 0.62\text{MPa} \quad 4\text{-}19$$

At the maximum MEHA operating temperature T_{max} of 70°C, the maximum accumulator pressure $P_{a,max}$ is computed using Equation 3-37

$$P_{a,max} = \frac{k_a}{A_a}\left(x_{a,max} + x_{a0} + \frac{\alpha_v(V+V_{ip})(T_0-T_{max})}{A_a}\right) = 0.66\text{MPa} \quad 4\text{-}20$$

The minimum accumulator pressure $P_{a,min}$ can similarly be computed using Equation 3-38 for the minimum MEHA operating temperature of -40°C

$$P_{a,min} = \frac{k_a}{A_a}\left(x_{a,max} + x_{a0} - \frac{\alpha_v(V+V_{ip})(T_0-T_{min})}{A_a}\right) = 0.57\text{MPa} \quad 4\text{-}21$$

The values of $P_{a,max}$ and $P_{a,min}$ show the importance of the accumulator in regulating the pressure changes due to thermal expansion and contraction of the hydraulic fluid within the closed hydrostatic circuits. At both extremes of the MEHA's operating temperature, the accumulator pressure is maintained at a level close to the nominal pressure due to the compliance of the accumulator spring and great pressure changes due to the thermal expansion or contraction of the hydraulic fluid are avoided.

4.10 Material selection

The choice of material for the components of the MEHA plays a vital role in minimising the total mass of the actuator. In addition, the friction acting on the pistons of the closed hydrostatic circuit is highly dependent of the materials used at the mating surfaces. As the

pressure within the closed hydrostatic circuit rises for mechanical power to be transmitted through it, the components have to be able to withstand the structural loads.

The forward and aft bases (Figure 4-1) act as bearing covers on the ballscrew shaft bearings mounted on the input casing. In addition, the forward base also acts as the housing for the gear train and mounting points for the motor and input casing. As the structural loads on these parts are expected to be small, Aluminium 6061-T6 is selected as the material for them.

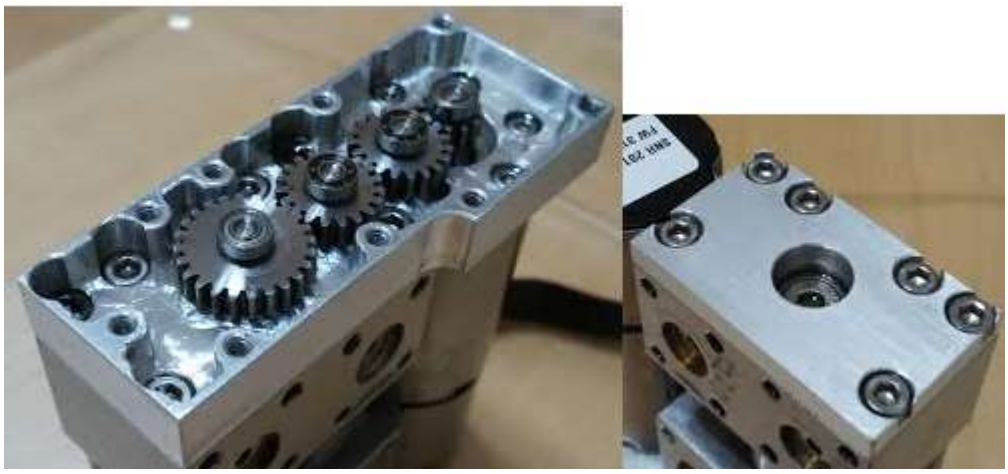

Figure 4-1: Input forward base housing the gear train (left) and aft base (right)

In the case of the input, output and accumulator pistons (Figure 4-2), stainless steel is a natural choice given the need for them to withstand high structural loads as forces are applied, as well as the requirement for high stiffness in these components. Hardened surfaces on these parts will help reduce friction and wear, while allowing for the grinding of the surfaces to achieve small clearances with their respective bores. These small clearances aid their alignment within their bores to minimise friction, seal damage and leakage. PH17-4 stainless steel heat-treated to H900 for high hardness is selected.

Figure 4-2: Input (top) and output (bottom) pistons

For the input, output and accumulator casings, the choice of material is less straightforward. They account for a large volume of the material within the MEHA thus the density of the material chosen for these components will have a significant impact on the MEHA's overall mass. The bores within these casings form sliding interfaces with their respective steel pistons, so the coefficient of friction of the chosen material with steel surfaces is an important consideration. The chosen material has to allow for easy fabrication of the internal channels within these casings. The strength of the material chosen also has to be able to withstand the high pressure within their bores. As a preliminary estimate, assuming that an effective material thickness of 1mm has to withstand the maximum expected pressure 20.9MPa found in Equation 4-8 in the 6mm bore selected in Section 4.6, the hoop stress due to this pressure load will be

$$\sigma_{\mathrm{h}} = \frac{\Delta \mathrm{P}_{\mathrm{max}}}{\mathrm{t_p}} \frac{\mathrm{d_p}}{2} = 62.7\mathrm{MPa} \qquad 4\text{-}22$$

Based on this estimate, the various materials in Table 4-7 can be considered. Polyetheretherketone (PEEK) is a high strength structural plastic that has a low coefficient of friction with steel sliding surfaces. Its lower density compared to metals means that there is potential for it to realise a very light MEHA. Aluminium is a lightweight metal that is frequently used in aerospace components thus it is included as a candidate material. However, as aluminium is known to have high friction with sliding steel surfaces, an

additional option is for a bronze insert to be used as an interface material within the bores between the aluminium casing and the steel pistons. Lastly, stainless steel is a common material used in hydraulic actuators due to its high strength and its low friction with another stainless steel sliding part. This comes with a penalty of high mass evident in the following table. This is partially mitigated by only using steel for the centre casing where it is in sliding contact with the output pistons and it is most exposed to the pressure within the closed hydrostatic circuit, thus only PEEK and aluminium will be considered for the covers of the output casing.

Table 4-7: Materials considered for input, output and accumulator casings

Material	Strength (MPa)	Mass of input casing (g)	Mass of output casing (g)	Mass of accumulator casing (g)
Polyetheretherketone (PEEK)	95	8.8	14.3	2.3
Aluminium 6061	275	20	21.1	4.8
Aluminium 7075 with bronze insert	505	21.6	22.8	5
Stainless steel PH17-4	1000	59.3	35.1	13.7

In this section, it is clear that that the PEEK option is superior in offering the lowest mass for the casings of the MEHA. In the following sections, analysis and experimental results will determine the ideal material based on other factors.

5. ANALYSIS OF MEHA PROTOTYPE

In this section, the components of the prototype developed in this work is first analysed to check that they are able to withstand the intended design loads, as well as to determine the optimum material for the components. This is followed by numerical analysis of the flow in the closed hydrostatic circuit when the MEHA is operating in active and damped modes. The dynamic performance of the prototype is then analysed with a computation of its bandwidth before the non-linear dynamic model developed in this work is used to study the effects of non-ideal factors. The section then concludes with a study of the closed hydrostatic circuit's contribution to the stiffness and accuracy of the MEHA.

5.1 Structural analysis

The analysis in this section is concerned with ensuring that the components of the MEHA prototype developed in this work are able to withstand their predicted structural loads. This is vital to ensure the safe operation of the prototype without structural damage during the testing phase. It also provides proof that the prototype developed during the course of this work is a realistic representation of the MEHA concept.

The structural analysis begins with the input casing. The bores for the input pistons of the input assembly are situated on the input casings. The bores of the input casing are subjected to the same maximum pressure of 20.9MPa within the closed hydrostatic circuit (Figure 5-1). With the ballscrew shaft and nut in between, the two input casings are secured to the output casing with fasteners and to each other via two steel rods. Fixed geometry constraints were applied to where these fasteners and steel rods are located on the input casings (Figure 5-2). The materials shortlisted in Table 4-7 are considered in this structural analysis. For the bronze insert, bores on the aluminium casing are expanded and the

pressure load is transferred directly to the casing. The mesh model of the analysis is shown in Figure 5-3 while stress plot of the analysis with stainless steel is shown in Figure 5-4.

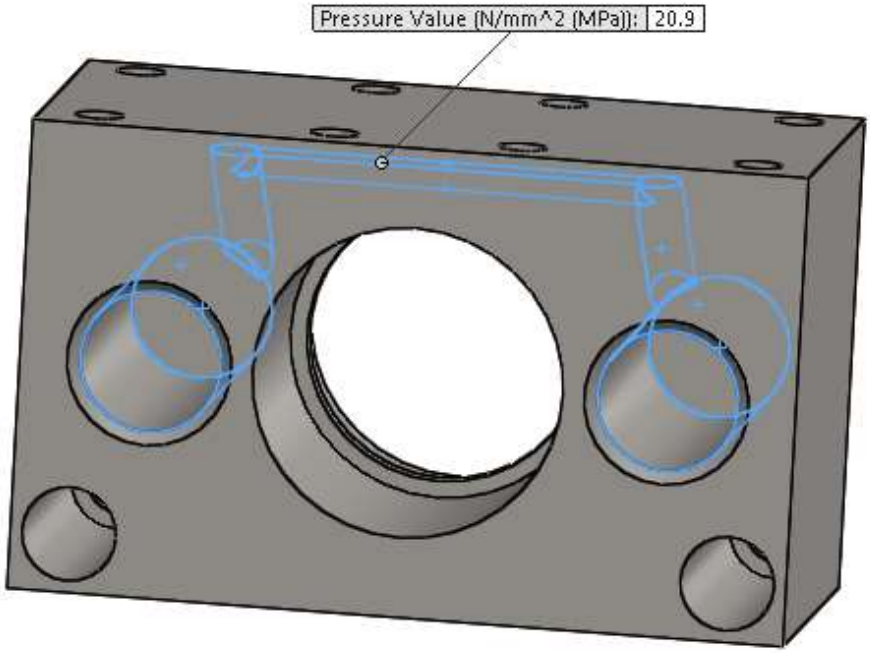

Figure 5-1: Loads on model of input casing

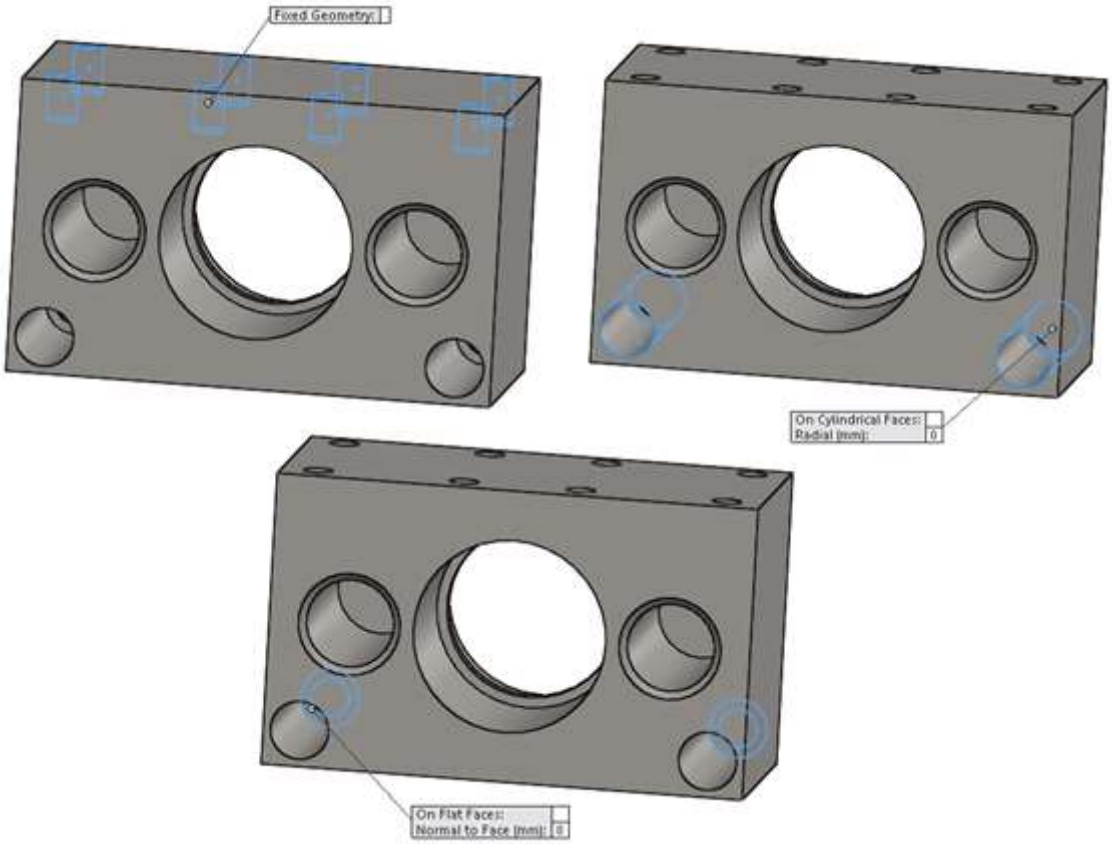

Figure 5-2: Constraints on model of input casing

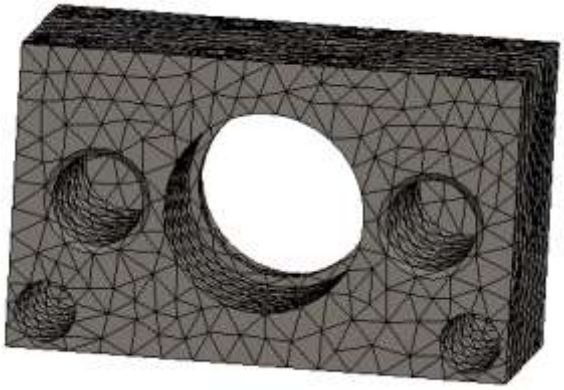

Figure 5-3 Mesh model of input casing

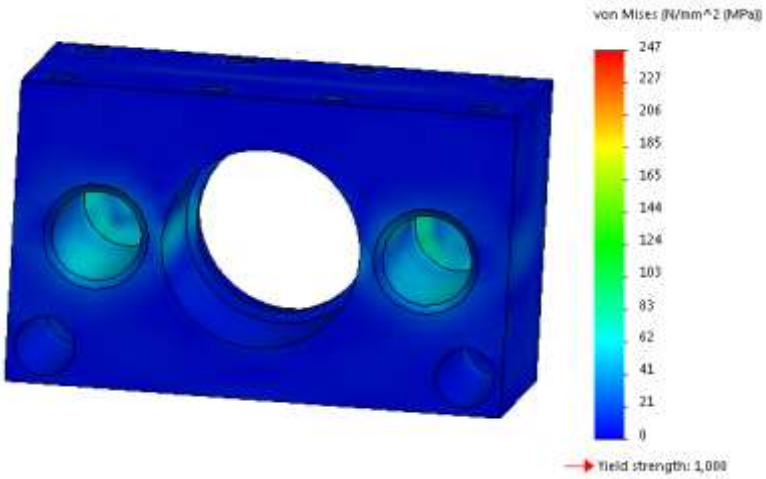

Figure 5-4: von Mises stress plot from structural analysis of the stainless steel input casing

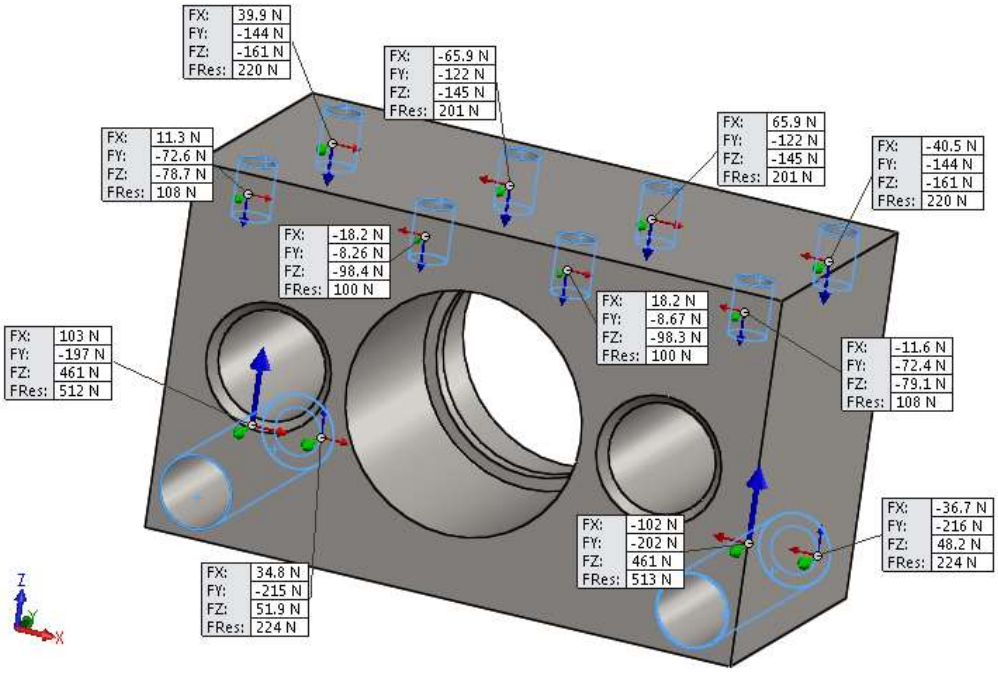

Figure 5-5: Resultant forces from structural analysis of input casing

Table 5-1: Structural analysis results of the input casing for the different materials

Material	Strength (MPa)	Max von Mises stress (MPa)	MOS
PEEK	95	237	NA
Aluminium 6061-T6	275	243	0.13
Aluminium 7075	505	301	0.68
Stainless steel PH17-4	1000	247	3.05

As seen in the preceding table, the stress in the input casing made of PEEK will exceed the tensile strength of the material. As such, PEEK is excluded as a candidate material for the input casing. Based on the structural analysis, the strength of the remaining materials will have positive margins of safety over the expected maximum stress in their structures.

The input piston transfers the applied force from the ballscrew nut to increase the pressure in the hydraulic fluid within the closed hydrostatic circuit. In this analysis, a fixed geometry constraint is applied on the face of the piston in contact with the ballscrew nut (Figure 5-6) while the expected maximum pressure of 20.9MPa within the closed hydrostatic circuit is applied to the opposing face that will be in contact with the hydraulic fluid (Figure 5-7). The input pistons are fabricated from PH17-4 stainless steel with a yield strength of 1000MPa. The mesh model used in this analysis is shown in Figure 5-8.

Figure 5-6: Constraint on model of input piston

Figure 5-7: Load on model of input piston

Figure 5-8: Mesh model of input piston

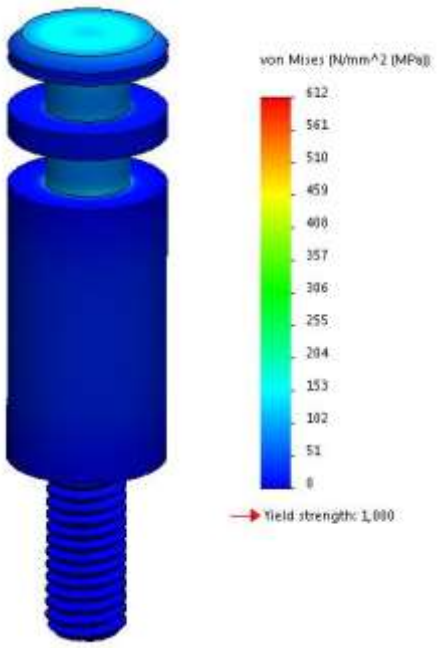

Figure 5-9: von Mises stress plot from structural analysis of input piston

The structural analysis shows that the maximum von Mises stress in the input piston (Figure 5-9) will be 612MPa. Compared to the material's yield strength, there is a MOS of

$$\text{MOS} = \frac{1000}{612} - 1 = 0.63 \qquad 5\text{-}1$$

Referring to the schematic of the output assembly in Figure 3-3, the inner covers cover both ends of the centre casing while channels that are cut into the covers allow for the flow of hydraulic fluid between the accumulator, output and input pistons within the closed hydrostatic circuits, thus the expected maximum pressure of 20.9MPa is applied to these channels and the inner face of the covers (Figure 5-10). A fixed geometry constraint is applied to the other side of the inner cover where the outer cover clamps it to the centre casing (Figure 5-11). As explained in Section 4.10, there will be two candidate materials for the covers of the output casing. The mesh model of this analysis is shown in Figure 5-12 while the results of the structural analysis with these materials are listed in Table 5-2.

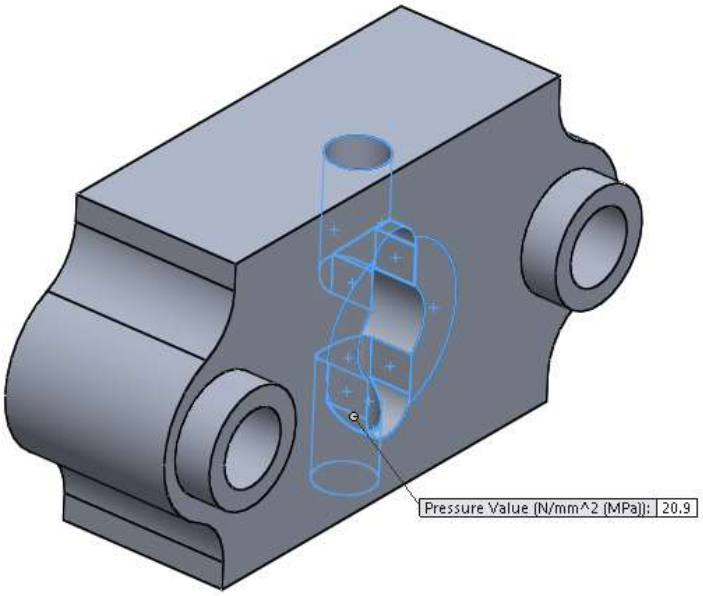

Figure 5-10: Pressure load on the model of the inner cover

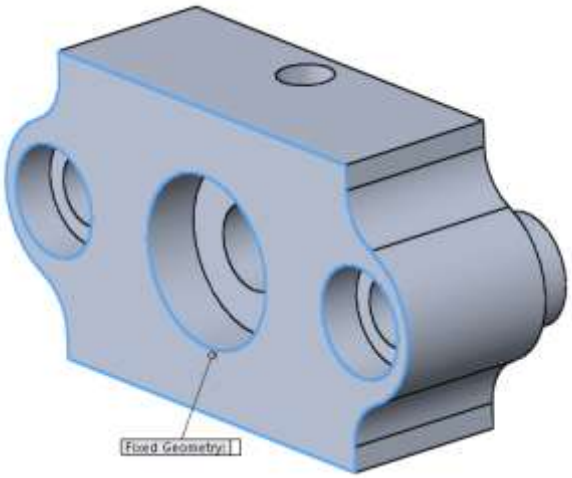

Figure 5-11: Constraint on model of the inner cover

Figure 5-12: Mesh model of the inner cover

Table 5-2: Structural analysis results of the inner cover for the different materials

Material	Strength (MPa)	Maximum von Mises stress (MPa)	MOS
PEEK	95	100.4	NA
Aluminium 6061-T6	275	100	1.75

The results show that if PEEK is used as the material for the inner cover of the output casing, it will not be able to withstand the stress due to the maximum pressure load from the closed hydrostatic circuit. Thus, only aluminium is a suitable material for the inner cover. Figure 5-13 shows the stress plot from the structural analysis of the aluminium inner outer cover.

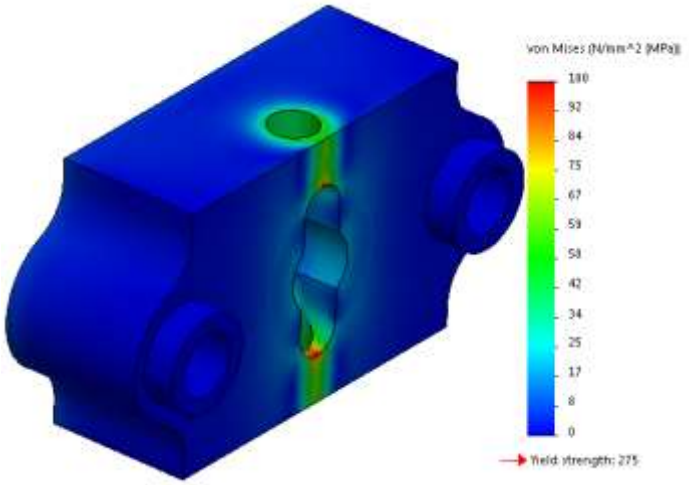

Figure 5-13: von Mises stress plot of the aluminium inner cover

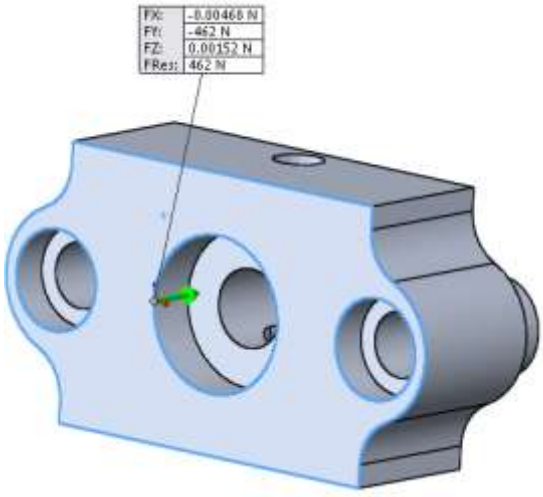

Figure 5-14: Resultant force on inner cover

The front outer cover of the output casing clamps the inner cover as well as mounts the input casing. The loads from the input casing (Figure 5-5) are applied on the bottom face of the outer cover model while those from the inner cover (Figure 5-14) are applied to its inner face (Figure 5-15). Fasteners secure the front outer cover to the centre casing, thus a fixed geometry constraint is applied at where the fasteners are in contact with the cover (Figure 5-16).

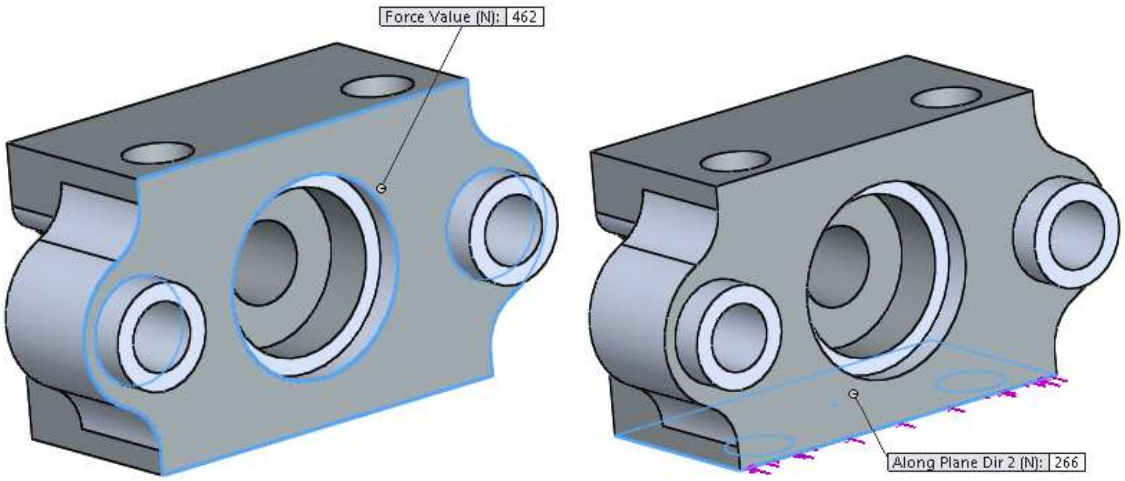

Figure 5-15: Loads on the model of the front outer cover

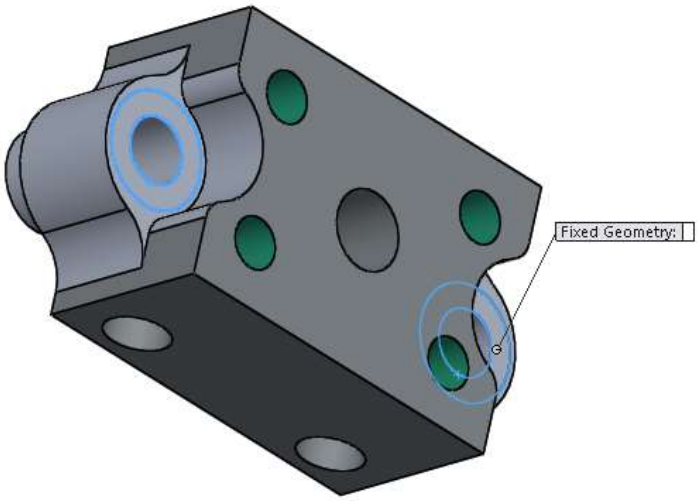

Figure 5-16: Constraints on the model of the front outer cover

Similar to the inner cover, two candidate materials are considered for the front outer cover. From Table 5-3, it can be concluded that aluminium is the only feasible material for the

front outer cover. Figure 5-17 shows the stress plot from the structural analysis of the aluminium front outer cover.

Table 5-3: Structural analysis results of the front outer cover for the different materials

Material	Strength (MPa)	Maximum von Mises stress (MPa)	MOS
PEEK	95	204.5	NA
Aluminium 6061-T6	275	219	0.26

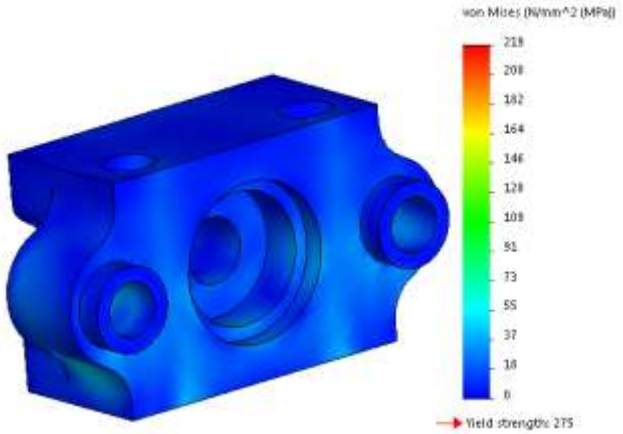

Figure 5-17: von Mises stress plot of the aluminium front outer cover

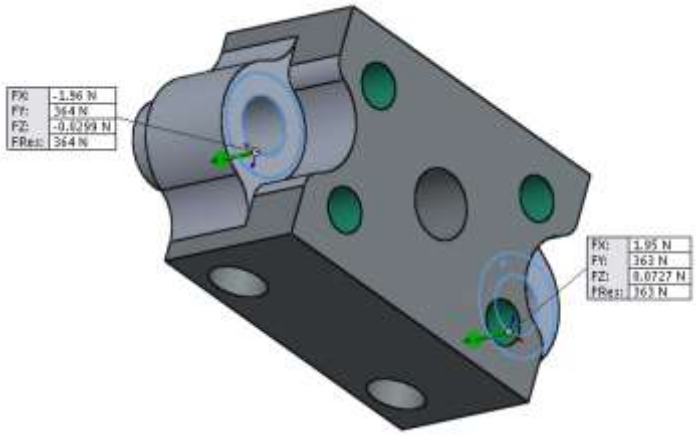

Figure 5-18: Resultant forces on front outer cover

The output assembly centre casing transfers the loads from the front covers to the rear covers. These loads from Figure 5-14 and Figure 5-18 are applied at the surfaces where the fasteners securing the covers to the centre casing. The centre casing is also subjected to the pressure load within the bore of the output piston, thus the expected maximum pressure of 20.9MPa is applied (Figure 5-20). Constraints are applied at the surfaces where fasteners

secure the rear covers to the centre casing (Figure 5-19). The candidate materials in Section 4.10 are considered in this analysis of the centre casing.

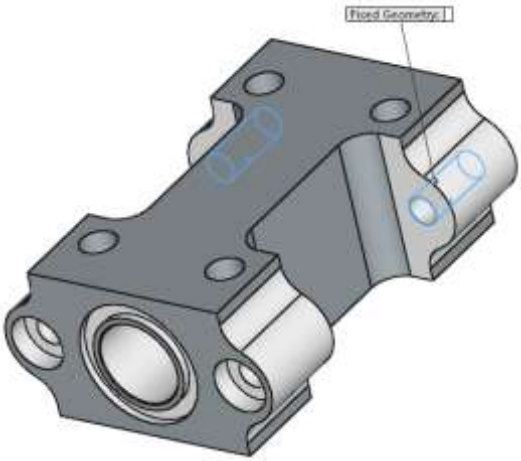

Figure 5-19: Constraint on model of centre casing

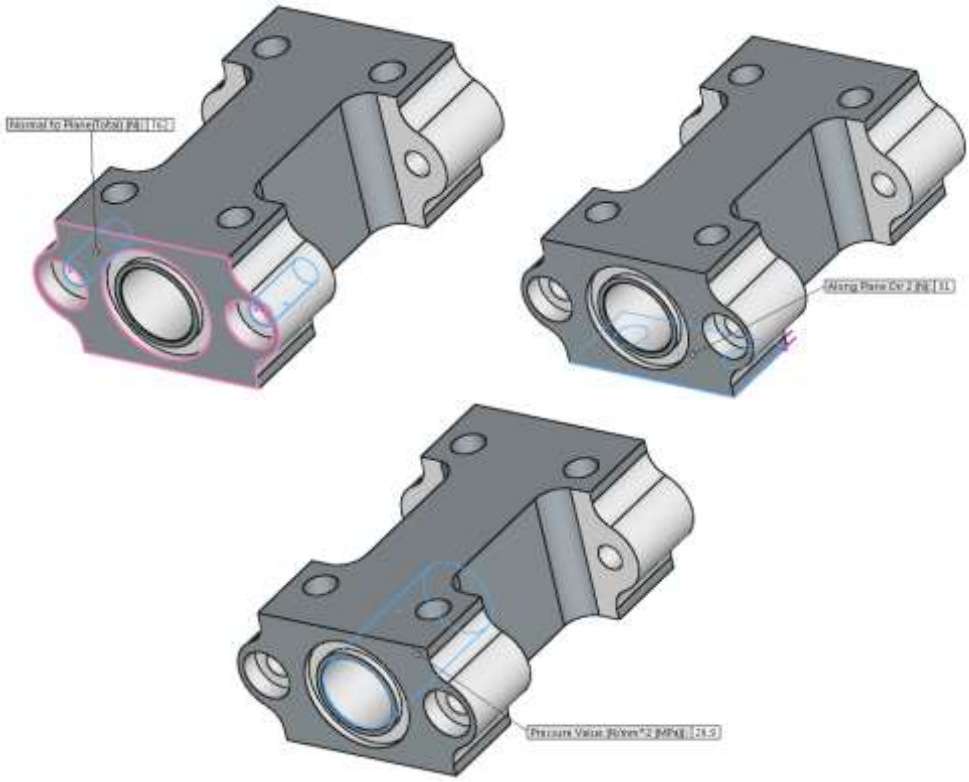

Figure 5-20: Loads on model of centre casing

The result presented in Table 5-4 show that only aluminium and steel can withstand the loads expected on the output assembly's centre casing. For the case of Aluminium 7075, the maximum stress is greater because of the need to expand the bore diameter to accommodate the bronze insert.

Table 5-4: Structural analysis results of the centre casing for the different materials

Material	Strength (MPa)	Maximum von Mises stress (MPa)	MOS
PEEK	95	96	NA
Aluminium 6061-T6	275	90	2.1
Aluminium 7075 with bronze insert	505	232	1.2
Stainless steel PH17-4	1000	91	10

Figure 5-21: Mesh model of the centre casing

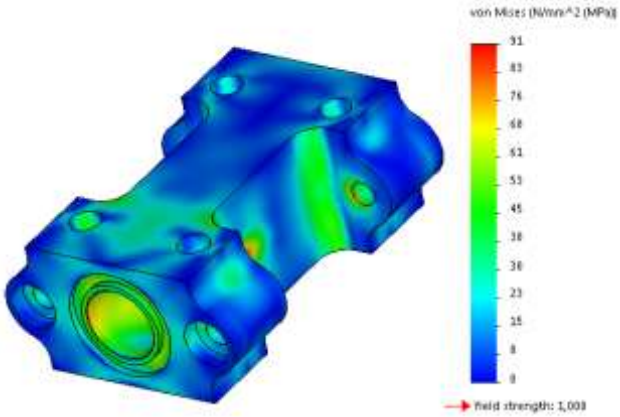

Figure 5-22: von Mises stress plot from structural analysis of steel centre casing

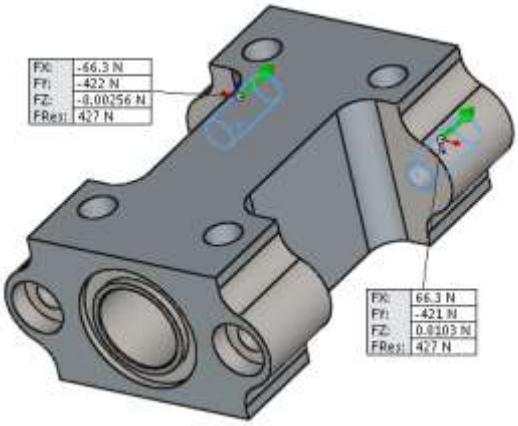

Figure 5-23: Resultant forces on centre casing

Within the MEHA's output assembly, the output piston converts the pressure difference across it into a force at the lever arm. In this analysis, a fixed geometry constraint is applied to the threaded portion where it interfaces with the lever arm (Figure 5-24). The maximum pressure difference of 20.9MPa expected across the piston from within the closed hydrostatic circuit is applied to the piston face (Figure 5-25). The output piston is fabricated from PH17-4 stainless steel with a yield strength of 1000MPa.

Figure 5-24: Constraints on model of output piston

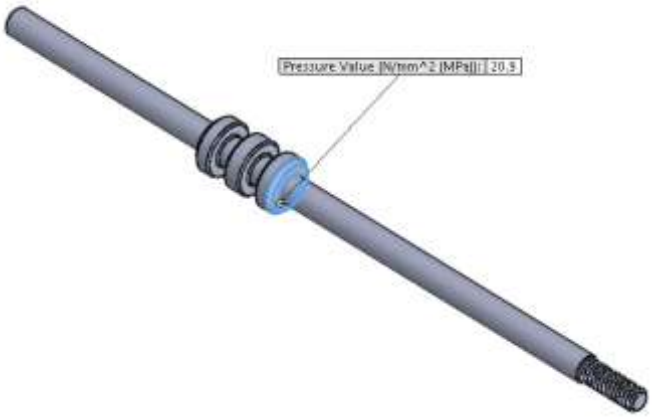

Figure 5-25: Loads on model of output piston

Figure 5-26: Mesh model of output piston

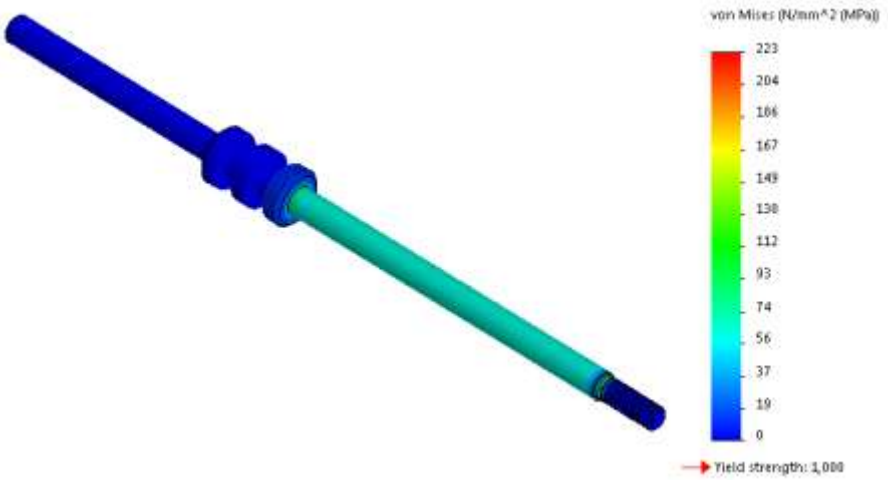

Figure 5-27: von Mises stress plot from structural analysis of output piston

Figures 5-26 and 5-27 show the mesh model and stress plots of the output piston. The maximum von Mises stress of 223MPa is expected from the structural analysis. The Margin of Safety (MOS) over the material yield strength will thus be

$$\text{MOS} = \frac{1000}{223} - 1 = 3.5 \qquad 5\text{-}2$$

At the MEHA's output, the lever arm converts the linear force from the output piston to a torque on the UAV's control surface. From the output piston and lever arm length parametric study in Table 4-5, the maximum linear force from the output piston is 443.2N with a lever arm length of 23.35mm to minimise the size of the MEHA's output assembly. This translates into a maximum torque of 10.35Nm about the lever arm's centre of rotation.

The bending stress on the lever arm can be computed using Equation 3-39 with the selected breadth b_l of 18mm and height h_l of 17.5mm

$$\sigma_l = \frac{(\mathrm{F}_{\max} l_l) l_l}{\mathrm{b}_l \mathrm{h}_l{}^3/12} = \frac{12 \times 443.2 \times 0.02335^2}{(18 \times 10^{-3})(17.5 \times 10^{-3})^3/12} = 30.1\mathrm{MPa} \qquad 5\text{-}3$$

In the lever arm's FE analysis, a linear force of 443.2N was applied perpendicular to the interface with the output piston (Figure 5-29) and a fixed geometry constraint was applied to the interface with the output shaft (Figure 5-28). The lever arm is fabricated from PH17-4 stainless steel with a yield strength of 1000MPa.

Figure 5-28: Constraints on model of lever arm

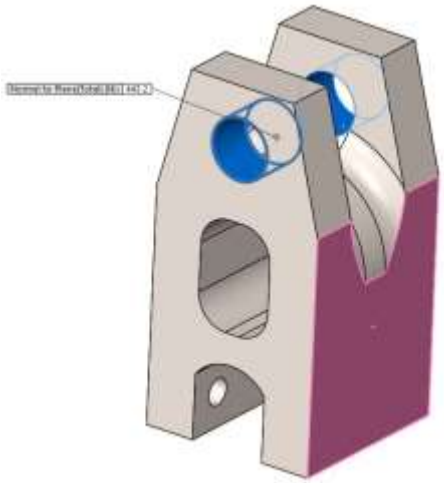

Figure 5-29: Loads on model of lever arm

Figure 5-30: Mesh model of lever arm

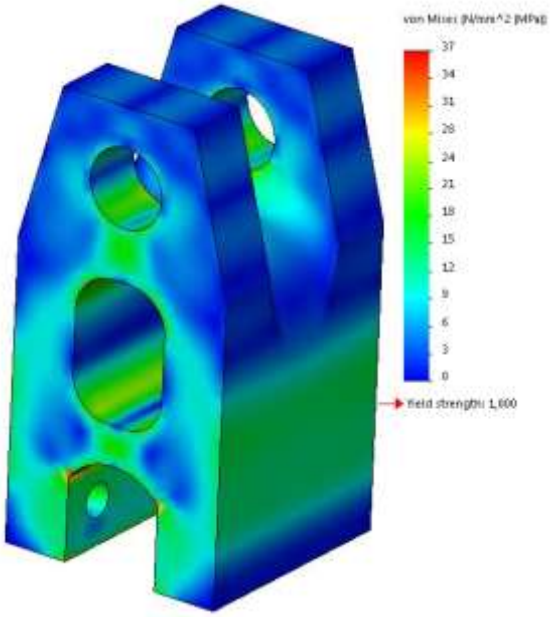

Figure 5-31: von Mises stress plot from structural analysis of lever arm

Figures 5-30 and 5-31 show the mesh model and stress plot of the lever arm. The structural analysis shows that the maximum von Mises stress in the lever arm will be 37MPa, which gives a large MOS relative to the material's yield strength

$$\text{MOS} = \frac{1000}{37} - 1 = 26 \qquad 5\text{-}4$$

Compared to the lever arm material's yield strength of 1000MPa, the maximum stress of 31MPa in the lever arm indicates that it is structurally sound. The large margin between the

yield strength and the maximum stress is to be expected since the lever arm has to be designed to maintain high stiffness.

The casing of the accumulator assembly houses the accumulator piston and spring, as well as the volume of hydraulic fluid within the accumulator circuit that was designed in Section 4.9 to cater for thermal expansion and contraction of the hydraulic fluid within the closed hydrostatic circuit. It is thus subjected to the accumulator pressure and the accumulator spring force (Figure 5-32). It is secured to the input casing with fasteners, so fixed geometry constraint is applied at where the fasteners clamp the accumulator casing (Figure 5-33).

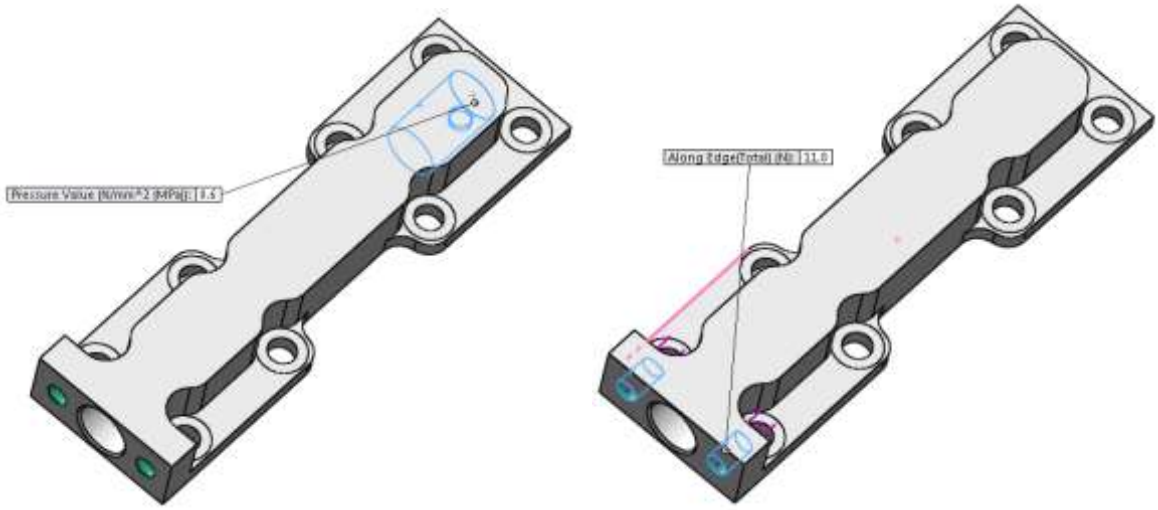

Figure 5-32: Loads on the model of the accumulator casing

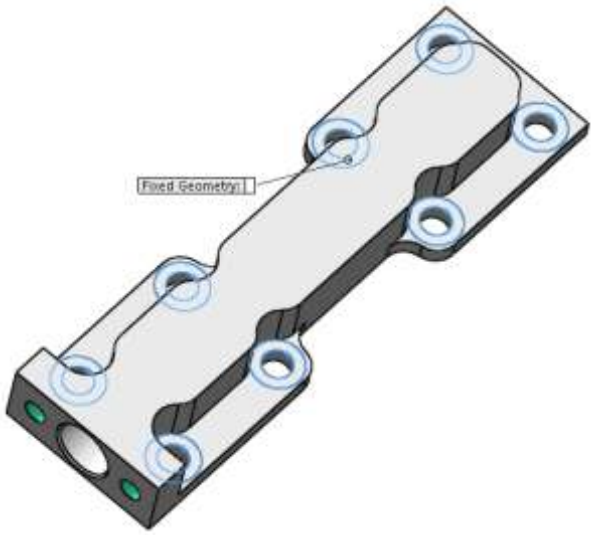

Figure 5-33: Constraint on the model of the accumulator casing

Candidate materials for the accumulator casing were considered in this analysis and the results are tabulated in the following table. Due to the small loads that the casing is subjected to, plastics such as PEEK can be used.

Table 5-5: Structural analysis results of the accumulator casing for the different materials

Material	Strength (MPa)	Maximum von Mises stress (MPa)	MOS
PEEK	95	6	15
Aluminium 6061-T6	275	6	45
Aluminium 7075 with bronze insert	505	8	62
Stainless steel PH17-4	1000	5	199

5.2 Numerical analysis of flow in hydrostatic circuit in operational mode

In Section 3.8, the channels of the closed hydrostatic circuit were sized to minimise their size and their fluid resistance. From the analytical equation 3-31, the pressure difference across the channels varies as a straight-line function for different flow rates if non-ideal effects are ignored. In this section, a CFD analysis of the channels is used to determine their flow resistance after the detailed design of the prototype is completed. A pressure boundary corresponding to the accumulator pressure is placed on the face of the output piston to simulate the effect of the accumulator in maintaining a minimum pressure within the closed hydrostatic circuit. An inlet boundary condition is placed on the faces of the input pistons which are in contact with the hydraulic fluid. The speed of the flow through the inlet boundary condition simulates the motion of the input pistons, and it is varied in this analysis to study the characteristic of the flow through the channels for different output piston speeds. From Section 4.7, the maximum speed of the input piston, $\dot{x}_{ip,max}$ was determined to be $0.067 \mathrm{ms}^{-1}$ which corresponds to the maximum flow rate of $3.79 \times 10^{-6} \mathrm{m}^3\mathrm{s}^{-1}$.

A mesh sensitivity study was conducted at the maximum input piston speed to determine the most suitable mesh for use in this study. Multiple runs of the same analysis problem with increasingly finer mesh were conducted and a comparison of the pressure result obtained for the range of mesh fineness examined is shown in Table 5-6 and Figure 5-34. Based on this study, the mesh 26X48X24 gave the largest improvement in results and it was selected as the mesh for this analysis.

Table 5-6: Results of mesh fineness evaluation

Mesh	Pressure difference across channel (Pa)	Variance in pressure
18X34X16	76302	1%
26X48X24	77056	16.4%
36X58X34	89672	-1%
56X78X54	88744	-0.25%
66X88X64	88522	-0.22%
76X98X74	88325	

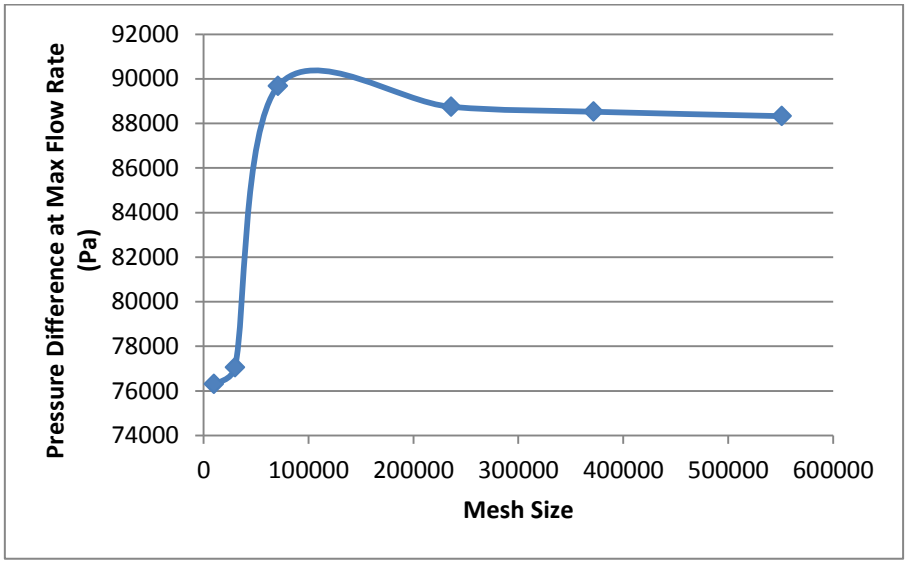

Figure 5-34: Plot of results from mesh fineness evaluation for normal mode CFD

Simulation runs were performed for the input piston speeds corresponding to the rotational speed of the electrical motor from 0 to 8000rpm at intervals of 1000rpm. The results of the numerical analysis are presented in Figure 5-35 and 5-36. From these results, it can be seen that the pressure due to fluid resistance of the channels is not a straight-line function of the

flow through it as predicted by Equation 3-31. The pressure predicted by this numerical analysis is also much higher than that predicted by the analytical Equation 4-14. These can be attributed to the presence of bends and sharp corners in the channels of closed hydrostatic circuit which lead to energy loss in the fluid flow and the need for greater pressure across the channel to drive the same flow rate as the flow speed increases.

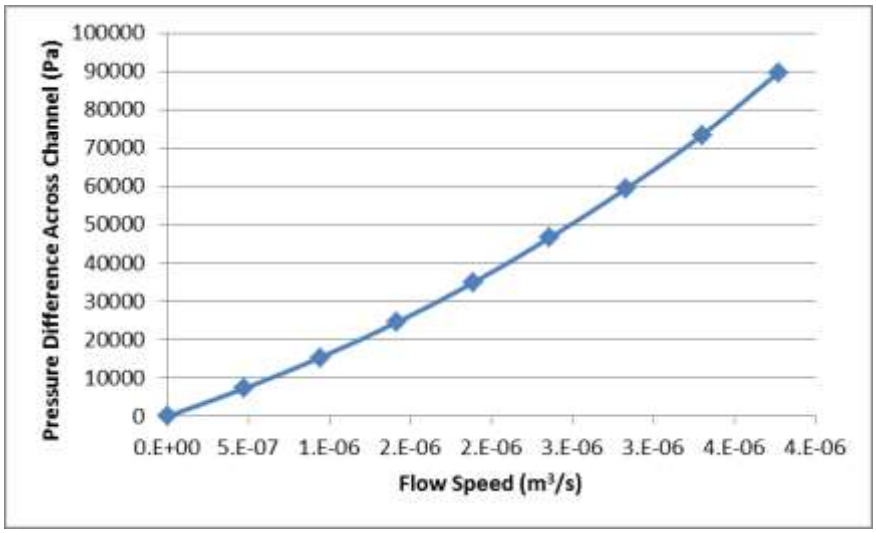

Figure 5-35: Pressure difference across channel at different flow speeds during normal operation

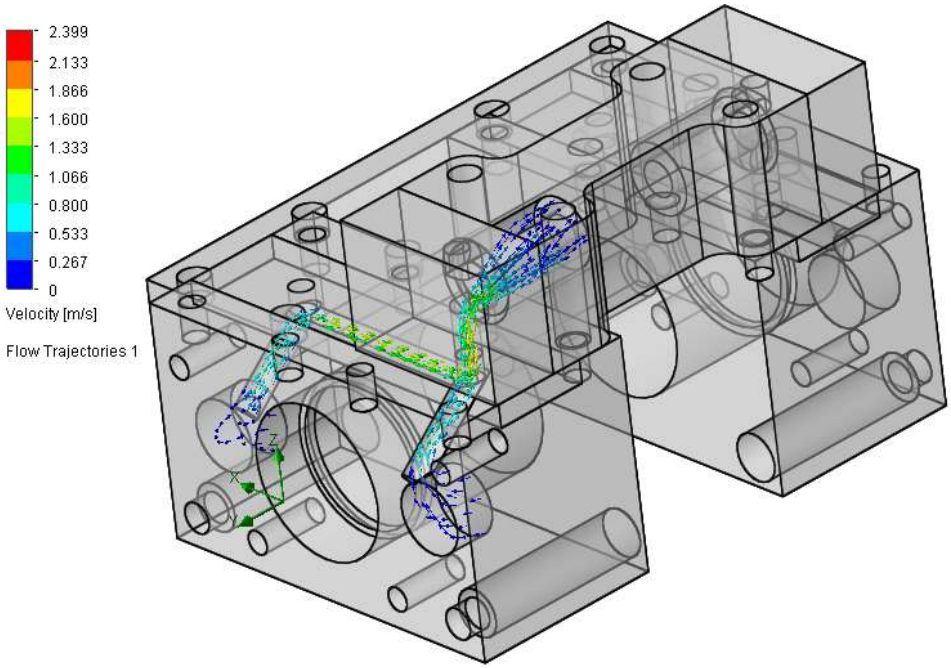

Figure 5-36: Visualisation of flow from input pistons to output piston

5.3 Numerical analysis of flow in hydrostatic circuit in bypass mode

For the MEHA's operation in bypass mode with the bypass valve open and flow passing across it to the other side of the output piston, CFD analysis is similarly performed to predict the fluid resistance that the flow is expected to encounter and the force on the output piston needed to actuate this flow. As was explained in Section 3.8, this force acts as a load on the remaining active MEHA and with the detailed design of the MEHA prototype completed, CFD can be used to predict this additional load without the ideal assumptions that were used in the initial sizing of the channel diameters in Section 4.8.

In this analysis, a pressure boundary condition corresponding to the accumulator pressure is placed on one face of the output piston, while an inlet boundary condition is place on the opposite face. The speed of the flow at the inlet boundary condition is set as the speed of the output piston. A mesh sensitivity study was performed with the expected maximum speed of the output piston found from Equation 4-12 to determine the optimal mesh for this analysis. A comparison of the pressure result obtained for the range of mesh fineness examined is shown in Table 5-7 and Figure 5-37. The mesh 36X58X34 gave the biggest improvement in results over the previous mesh and was thus chosen as the mesh to be used in this analysis.

Table 5-7: Results of mesh evaluation

Mesh	Pressure difference across channel (Pa)	Variance in pressure
10X16X8	482490	
12X22X12	386885	-19.8%
18X34X16	358715	-7.3%
26X48X24	365418	1.9%
36X58X34	400550	9.6%
56X78X54	403700	0.79%

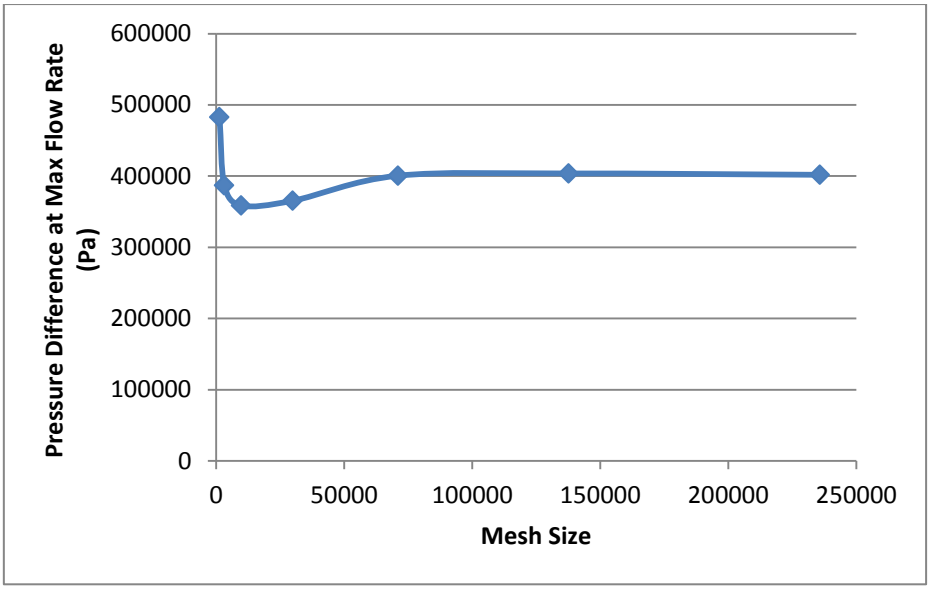

Figure 5-37: Plot of results from mesh fineness evaluation for bypass mode CFD

The selected mesh was then applied to the problem with different output piston speeds. In the bypass mode, the output piston has to be driven by the remaining MEHA, thus the simulation runs were performed for the output piston speeds corresponding to the rotational speed of the remaining operational electric motor electrical motor from 0 to 8000rpm at intervals of 1000rpm.

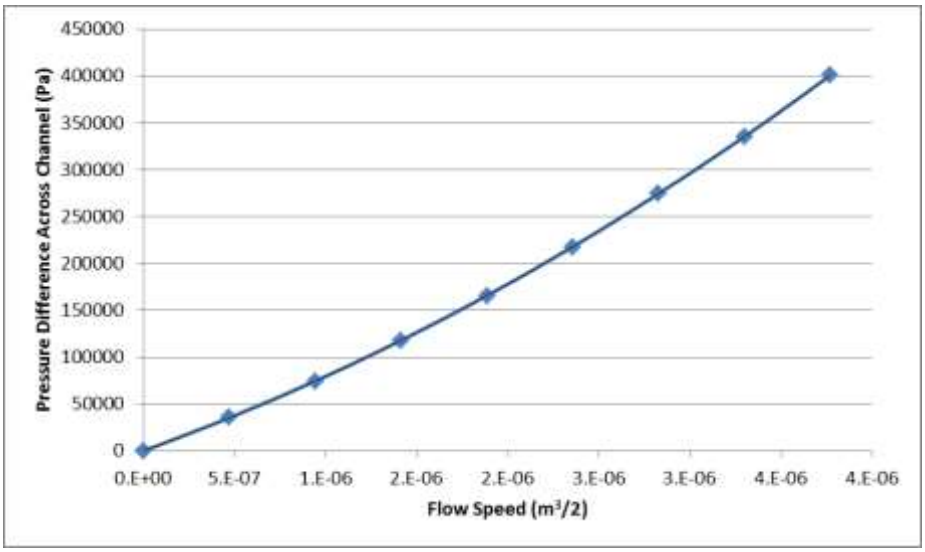

Figure 5-38: Pressure difference across bypass channel for different motor speeds

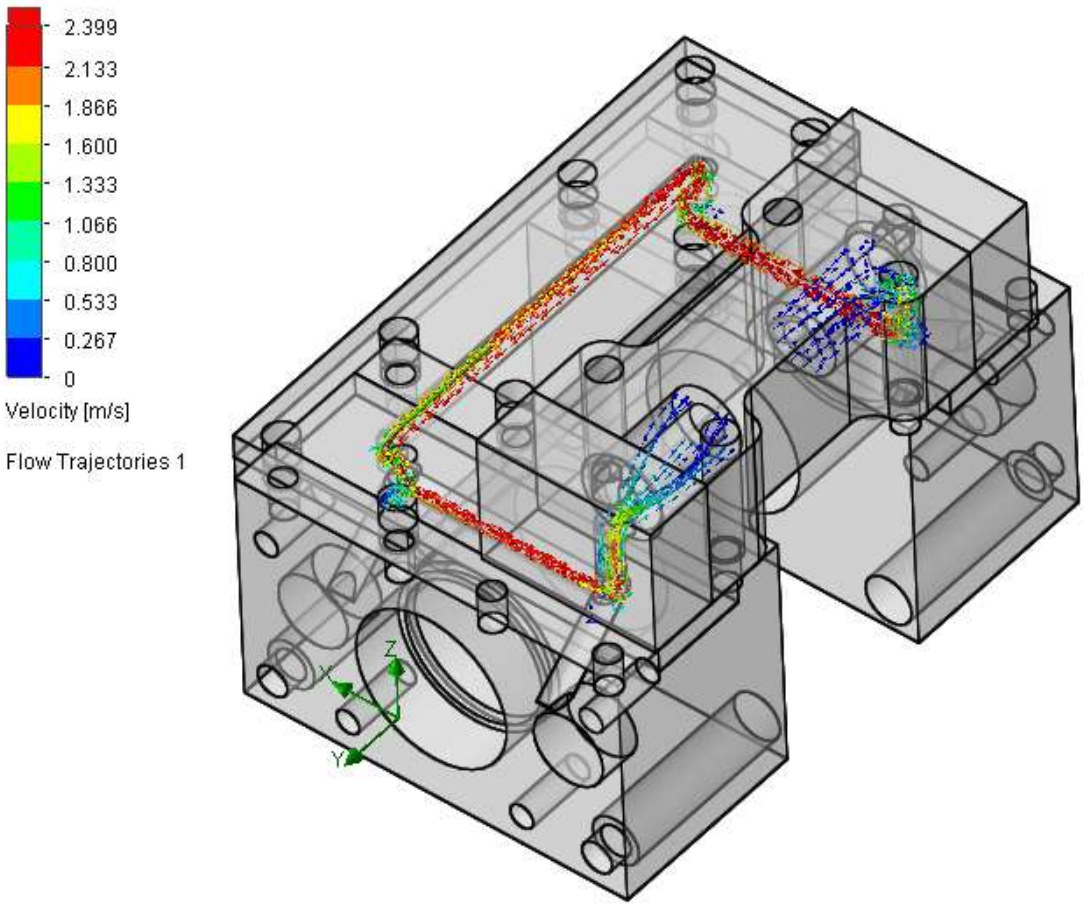

Figure 5-39: Flow visualisation of flow between opposing sides of the output piston through the bypass channels

The results from the simulation runs are summarised in Figure 5-38 and 5-39. While Equation 3-30 predicts that the pressure difference across the channel will be a straight-line function of the flow through it, this analysis predicts that the relationship will be a polynomial function. Compared to the pressure difference predicted in Equation 4-13, the magnitude of the pressure difference predicted in this analysis is also significantly higher. These can be attributed to the presence of bends in the path of the fluid flow as well as the non-circular cross-section of the channels. This underscores the need for CFD analysis after the detailed design of the MEHA is completed to predict the actual flow resistance so that these effects can be included in the MEHA's dynamic model to study their impact on the MEHA's performance.

5.4 MEHA Bandwidth

The MEHA's dynamic performance can be estimated by considering the load as 'seen' at the BLDC motor. The rotational inertias of the gear train and ballscrew shaft, as well as the mass of the ballscrew nut and pistons can all be converted to an equivalent total inertia of the MEHA's transmission at the motor, J_t using Equations 3-34 to 3-44.

Table 5-8: MEHA transmission equivalent rotational inertia at motor

Component	Component rotational inertia/mass	Equivalent rotational inertia ($\mathbf{kgm^2}$)
Electric motor gear	$3.307 \times 10^{-9}\ \mathrm{kgm^2}$	3.307×10^{-9}
Idler gear	$1.89 \times 10^{-8}\ \mathrm{kgm^2}$	1.51×10^{-8}
Ballscrew shaft gear	$4.8 \times 10^{-8}\ \mathrm{kgm^2}$	1.2×10^{-8}
Gear train		$\mathbf{3.04 \times 10^{-8}}$
Ballscrew shaft	$4.76 \times 10^{-8}\ \mathrm{kgm^2}$	1.19×10^{-8}
Ballscrew nut	$0.028\ \mathrm{kg}$	1.77×10^{-10}
Ballscrew		$\mathbf{1.21 \times 10^{-8}}$
Input pistons	0.0127kg	8.04×10^{-11}
Input pistons		$\mathbf{8.04 \times 10^{-11}}$
Output piston	0.00528kg	2.34×10^{-10}
Output piston		$\mathbf{2.34 \times 10^{-10}}$
Total MEHA transmission		$\mathbf{8.56 \times 10^{-8}}$

The following properties of the electric motor and load are required to find the MEHA's bandwidth:

- Motor resistance, $R_a = 12.4\Omega$
- Motor constant, $K_t = 0.0314\mathrm{Nm/A}$
- Motor rotational inertia, $J_m = 0.52 \times 10^{-6}\mathrm{kgm^2}$
- Load inertia, $I = 0.015\mathrm{kgm^2}$
- Equivalent inertia at motor for load inertia, $J_{load} = \frac{I}{N^2} = 1.24 \times 10^{-6}\mathrm{kgm^2}$
- Total equivalent inertia at the motor = 2.45 X 10^{-6} kgm^2

The mechanical time constant and bandwidth of the MEHA can then be computed using Equations 2-11 and 2-12,

$$\tau = \frac{12.4\times\left(0.52\times10^{-6}+8.56\times10^{-8}+1.24\times10^{-6}\right)}{(0.0314)^2} = 23.2\text{ms} \quad 5\text{-}5$$

$$f = \frac{1}{2\pi(23.2\times10^{-3})} = 6.86\text{Hz} \quad 5\text{-}6$$

Analysis of the MEHA using the simplified dynamic model developed in Section 3.3 (see Figure 3-10) shows that the bandwidth of the position control loop is 42.9rad/s or 6.83Hz (Figure 5-40). This is more than twice the bandwidth requirement of 3Hz for the benchmarks in Table 2-1 and Table 2-2, and it provides a comfortable margin of safety for the MEHA prototype to meet the benchmark requirements.

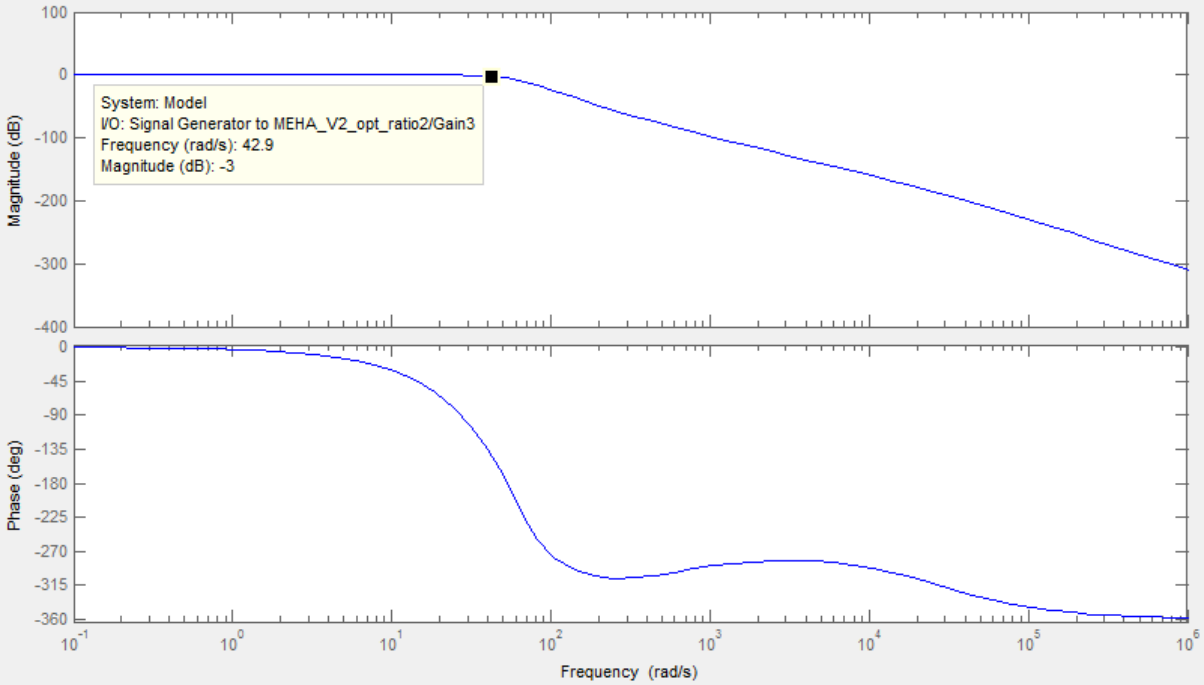

Figure 5-40: Bode plot of the simplified MEHA model

5.5 Non-linear dynamic analysis of MEHA

In Section 3.12, the dynamic model of the MEHA and its components was developed. This model allows for the simulation of non-ideal effects such as hydraulic fluid compressibility and flow resistance within the closed hydrostatic circuit. Such simulation aids the investigation of the effects of these factors on the performance of the MEHA, in addition to ensuring that requirements are met. The peak forces and pressures during dynamic operation of the MEHA can also be predicted from this simulation models.

In Section 4.2, the total reduction ratio of the MEHA was optimised using a simplified model developed in Section 3.3. For the total reduction ratio selected from this optimisation, the plots of the current consumption and driving voltage for the electric motor are shown in Figure 5-41 and Figure 5-43 respectively. These represent the load on the motor with the assumption that the effects of the MEHA's transmission are negligible.

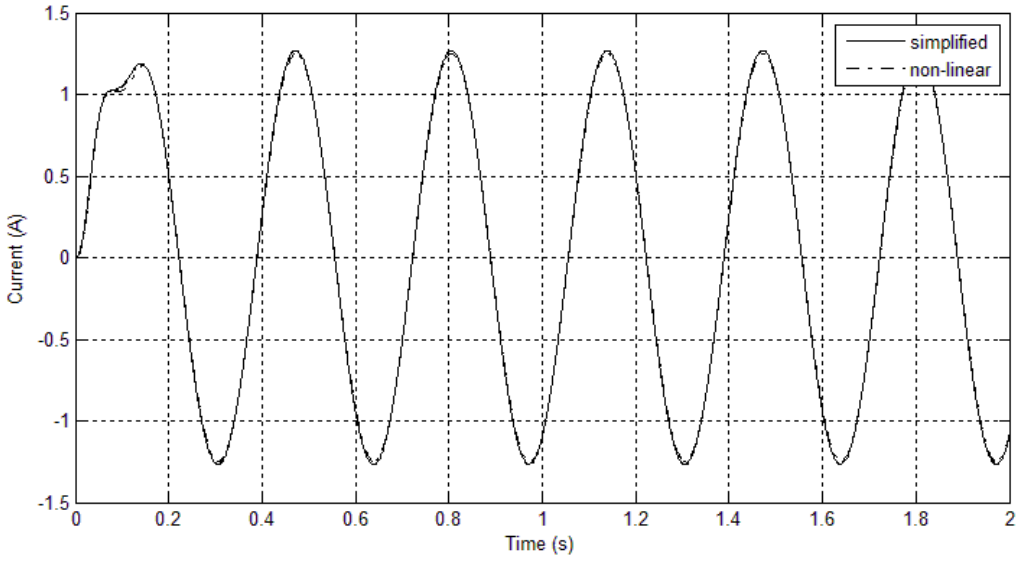

Figure 5-41: Current consumption by motor in simplified and non-linear models with hydraulic fluid compressibility and accumulator

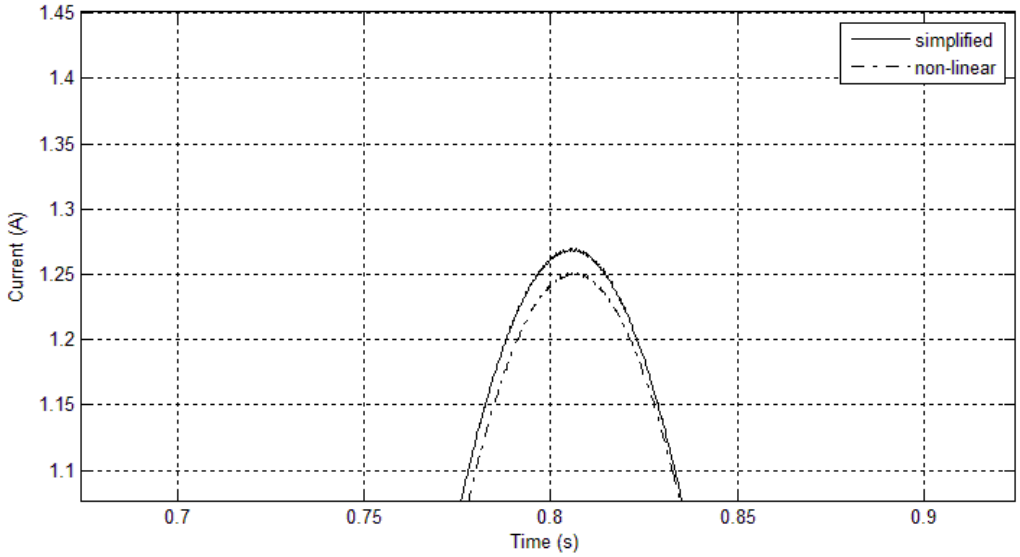

Figure 5-42: Close-up view of Figure 5-41

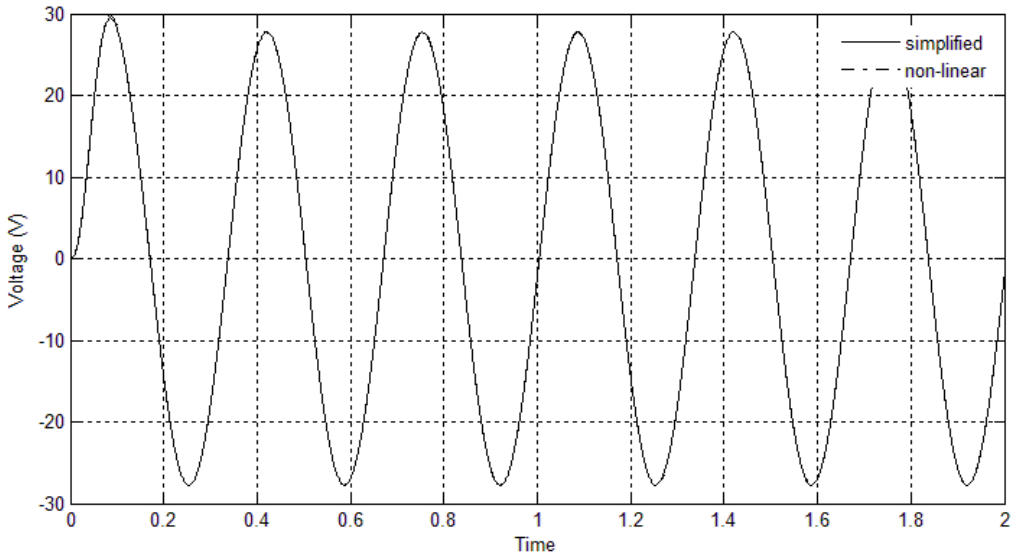

Figure 5-43: Voltage supplied to motor in simplified and non-linear models with hydraulic fluid compressibility and accumulator

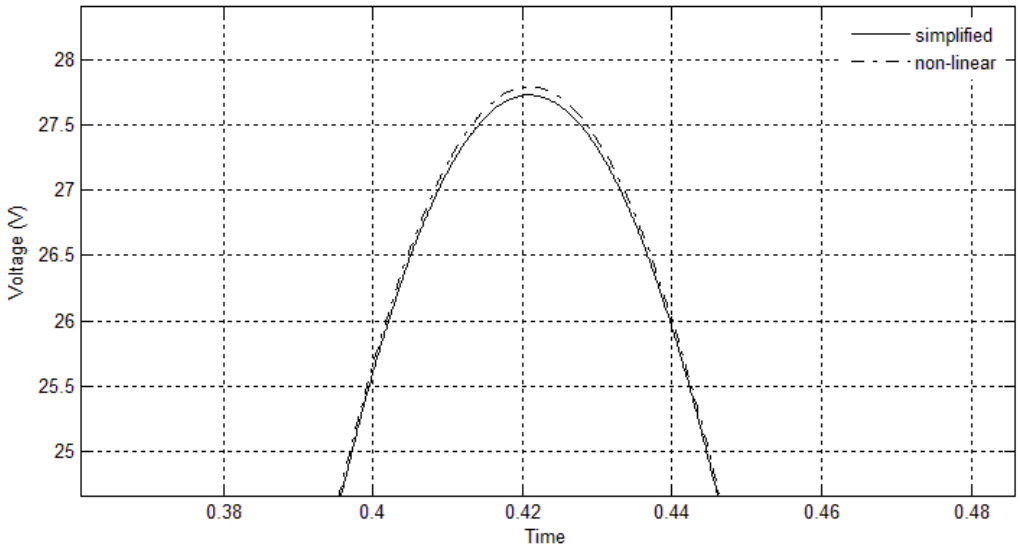

Figure 5-44: Close-up view of Figure 5-43

With the non-linear dynamic model, the effects of the hydraulic fluid's compressibility and the accumulator can be studied. Due to the high bulk modulus of the hydraulic fluid at 1.3×10^9 and the small volume of hydraulic fluid within closed hydrostatic circuit, the effect of the hydraulic fluid's compressibility is nearly negligible, as can be seen in Figure 5-42 and Figure 5-44. From Figure 5-45, it can be observed that the accumulator designed in Section 4.9 will be effective in maintaining the minimum pressure within the closed hydrostatic circuit of the MEHA during operation.

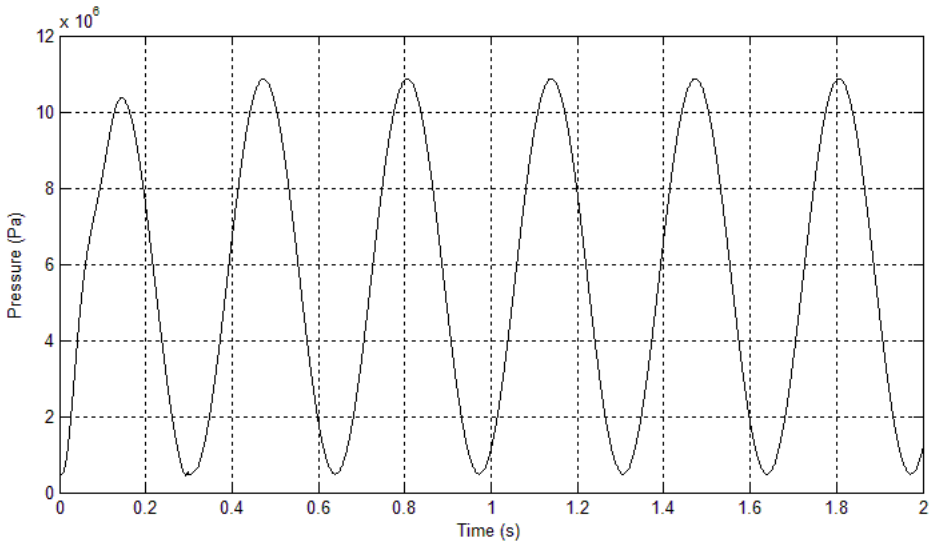

Figure 5-45: Pressure in closed hydrostatic circuit on one side of the output piston

Continuing with the non-linear model of the MEHA, the effect of flow resistance of the connecting channels between the input and output pistons is studied next. With the flow resistance predicted in Section 5.2, it can be seen from Figure 5-46 to Figure 5-49 that the effect on the MEHA is minimal. This can be attributed to the short length of the connecting channels of the closed hydrostatic circuit and the relatively low speed of the flow within them.

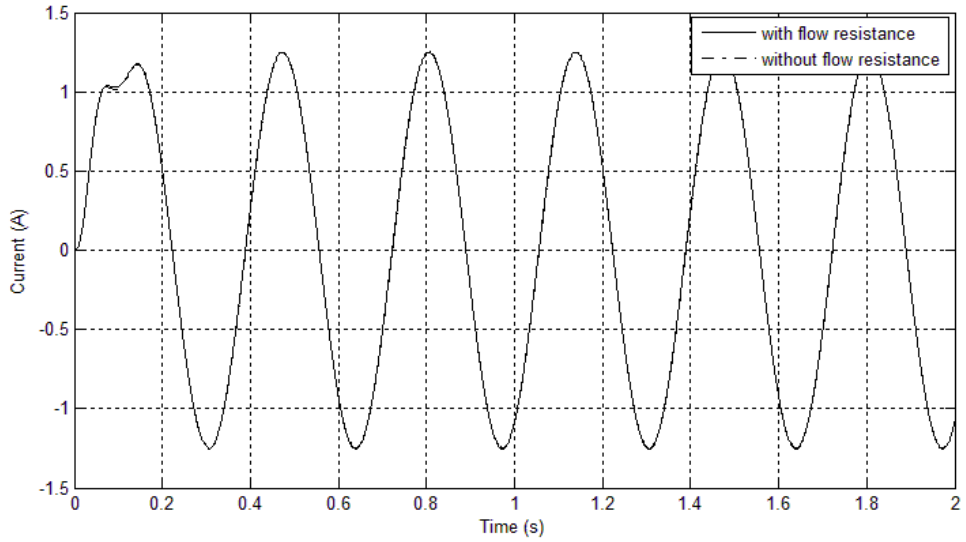

Figure 5-46: Motor current consumption in non-linear model with and without flow resistance

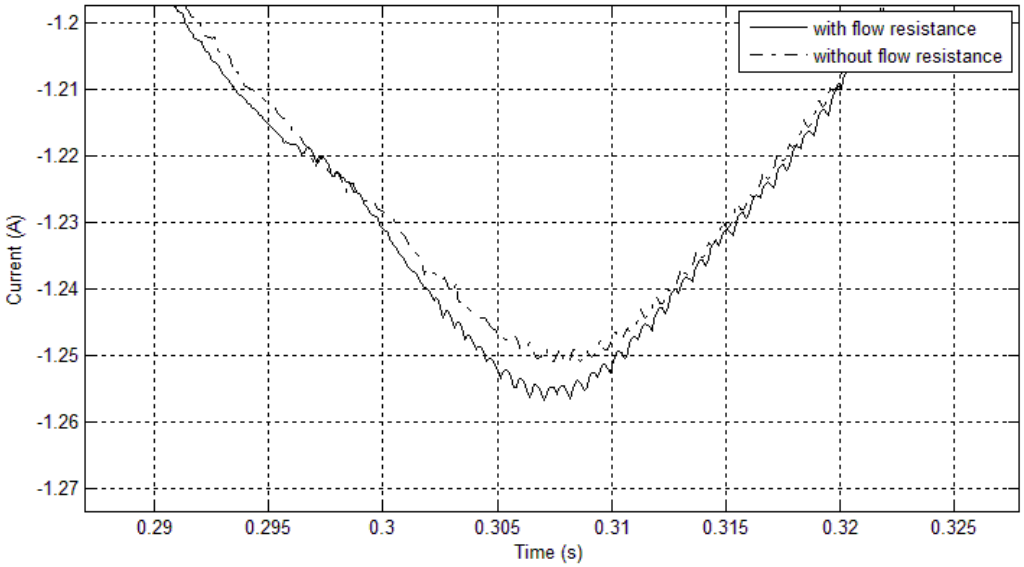

Figure 5-47: Close-up view of Figure 5-46

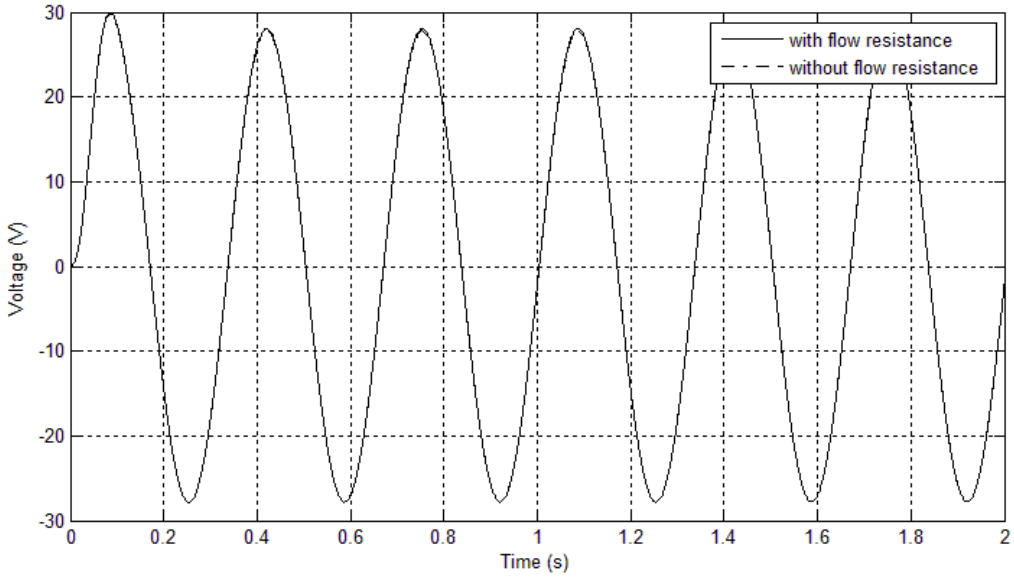

Figure 5-48: Voltage supplied to motor in model with and without flow resistance

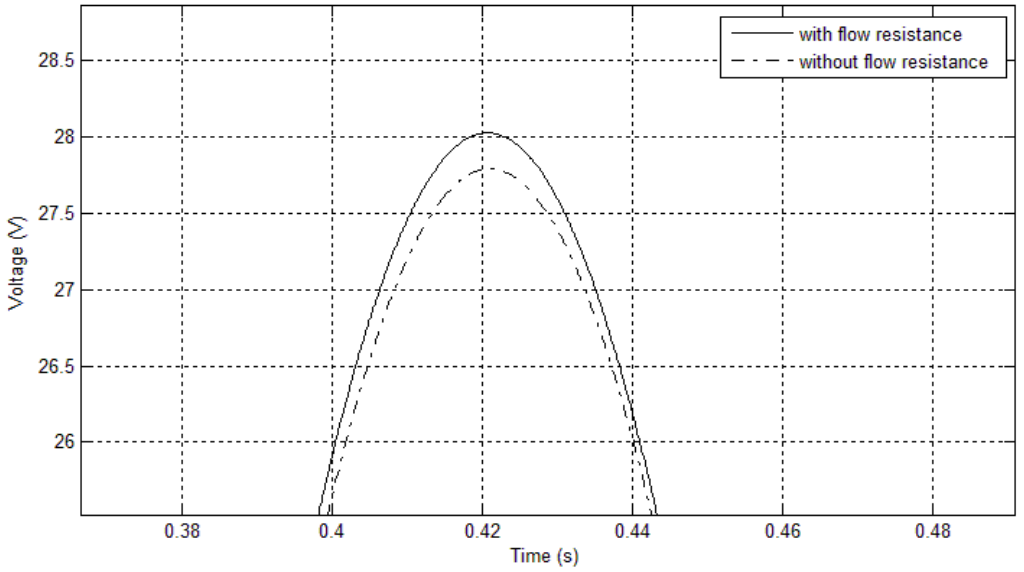

Figure 5-49: Close-up view of Figure 5-48

The friction of the input and output pistons are an important factor that was not considered in the simplified model developed in Section 3.3 and used in the optimisation of the MEHA's total reduction ratio in Section 4.2. As the friction within a system is dependent on the material and geometry of mating parts, the dynamic model requires experimental data obtained in Section 6.2 to study the effects of friction on the dynamic performance of the MEHA. For the range of speeds expected from the motor, it can be seen that the kinetic

friction is fairly constant and for the ease of implementation, it is modelled as a constant average value in the friction sub-system model used in the MEHA's non-linear model. From the experimental results, an average value for the static friction was also obtained and included in the friction sub-system.

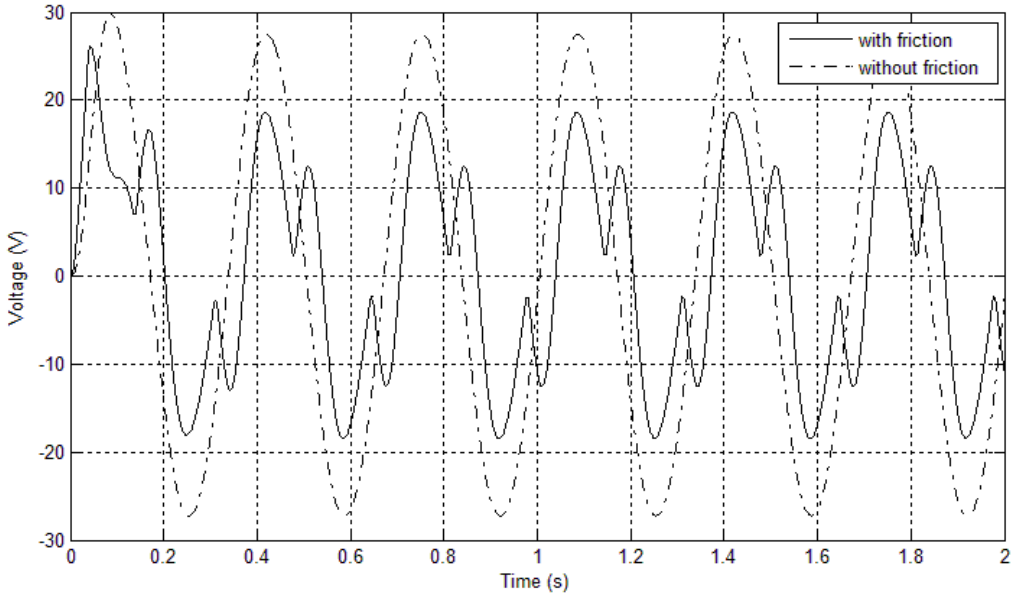

Figure 5-50: Voltage supplied to motor in the model with and without friction

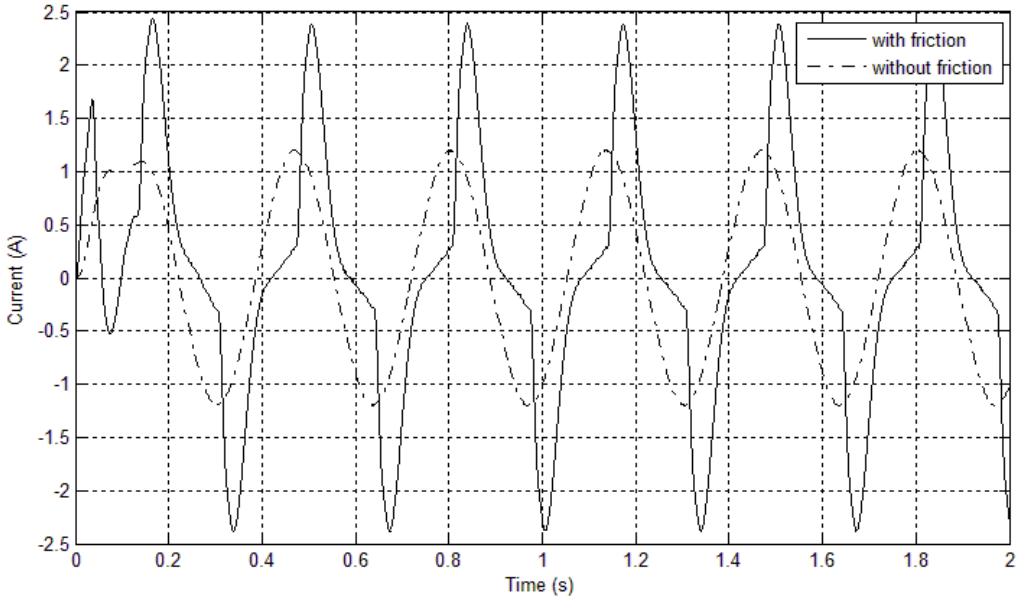

Figure 5-51: Current consumed by motor in the model with and without friction

Figure 5-50 and Figure 5-51 show the drastic effect of including friction in the simulation model. The voltage supplied to the motor varies greatly as the control loop has to overcome the static friction of the pistons in order to drive them against the kinetic friction and the MEHA's load. Compared to the simulation without friction, the damping effect of friction reduces the peak voltage applied to the motor as the combined inertia of the MEHA's components is prevented from accelerating and overshooting to high speeds, reducing the peak voltage that the controller needs to compensate for these overshoots. The friction on the pistons also results in higher current consumption by the motor. Within the closed hydrostatic circuit, the peak pressure is increased as the high static friction prevents the motion of the pistons until the force applied is sufficient, at which point the pistons surge forward to increase the pressure within the hydraulic fluid till it is sufficient to stop the mass inertia of the pistons. It is also important to note that despite the highly dynamic motion of fluid within the closed hydrostatic circuit due to the friction on the pistons, the accumulator is able to maintain the minimum pressure within the hydraulic fluid, serving its function of preventing cavitation.

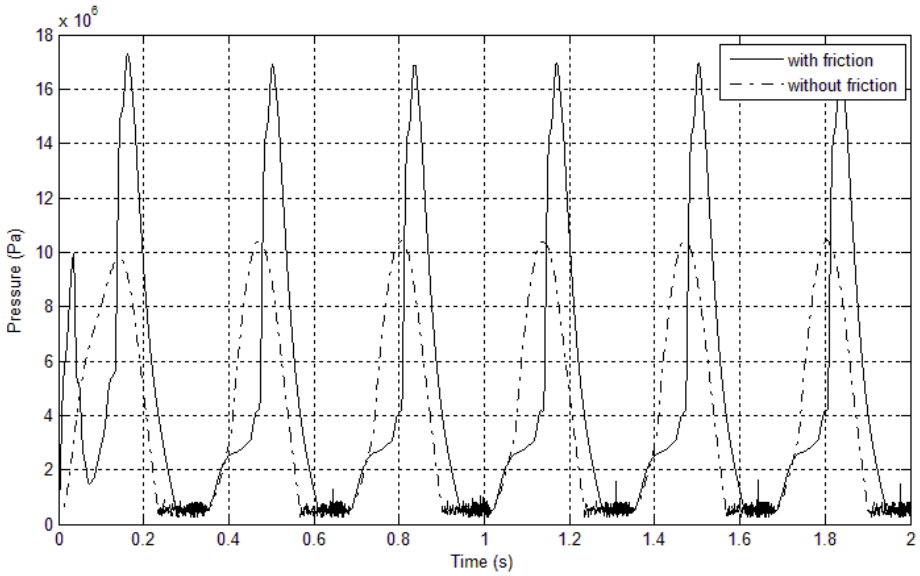

Figure 5-52: Pressure in the closed hydrostatic circuit on one side of the output piston

In order to investigate the effects of leakage on the dynamic performance of the MEHA, the leakage rate at different pressures has to be similarly obtained from experimental results in Section 6.2 and included in the MEHA's non-linear dynamic model. From Figure 5-53 and Figure 5-54, it can be seen that the effects of leakage on the MEHA's dynamic performance are minimal.

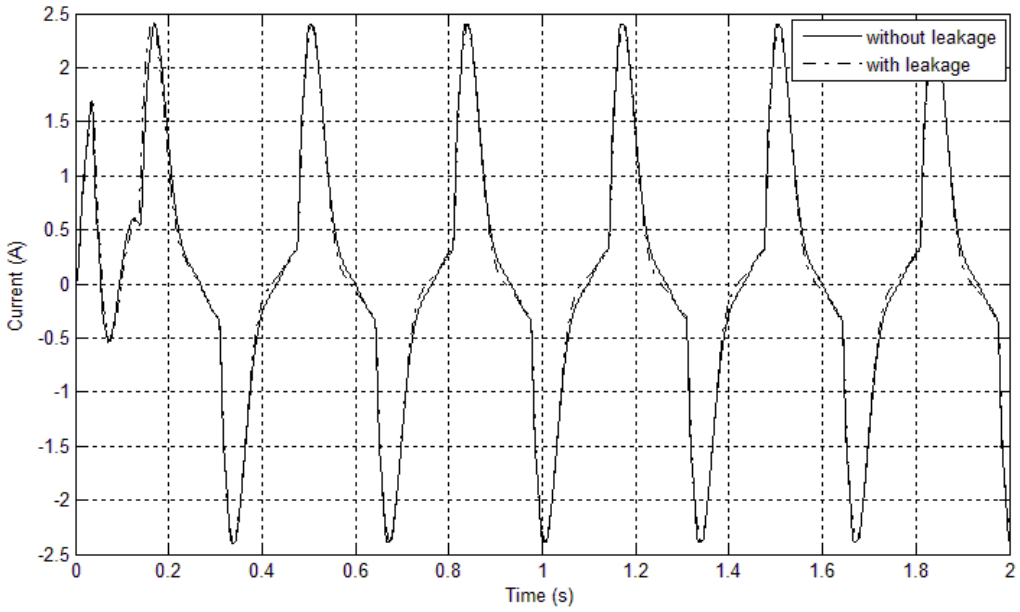

Figure 5-53: Current consumed by motor in the model with and without leakage

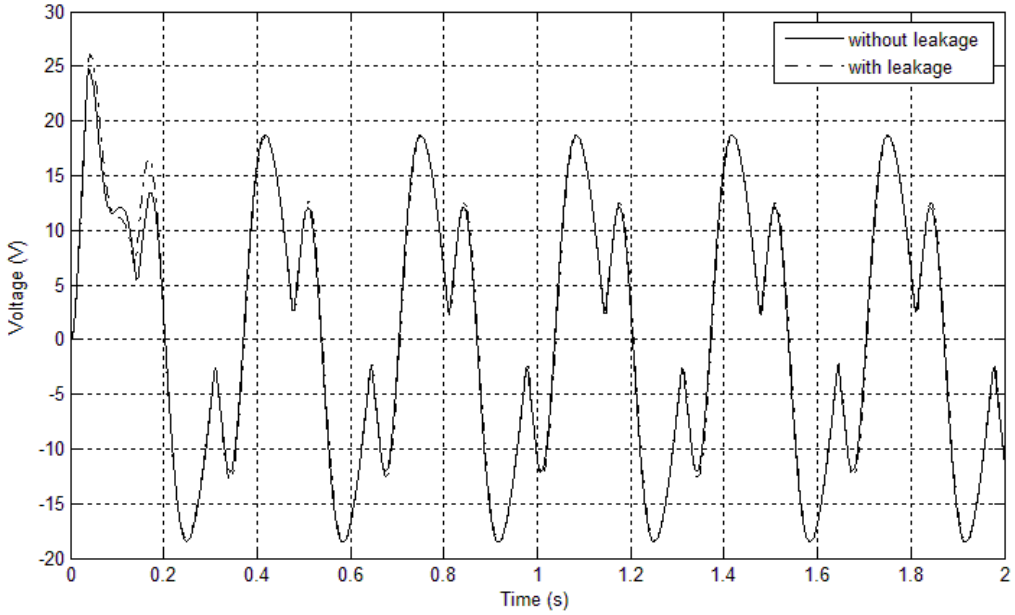

Figure 5-54: Voltage supplied to motor in the model with and without leakage

During normal operation where both MEHAs are active, they act in tandem to drive the load. When a fault develops in one of the MEHA and its bypass valve is opened, the flow from one side of its output piston is allowed to flow to the opposite side and this MEHA operates in the damped mode. The remaining active MEHA then has to drive the output piston of the damped MEHA. The models for both modes were developed in Section 3.11 (see Figure 3-19 and Figure 3-20).

When operating in tandem mode, it can be seen from Figure 5-55 and Figure 5-56 that the mechanical power required of each individual motor is about half of that required of the motor when the MEHA is operating singularly against the load since both the supplied voltage and consumed current are reduced by to 70% of that needed by a singular MEHA. This can be attributed to the dominant effect of friction at the input pistons within the MEHA which has to be overcome by each individual motor regardless of whether the design load is shared with another MEHA. .

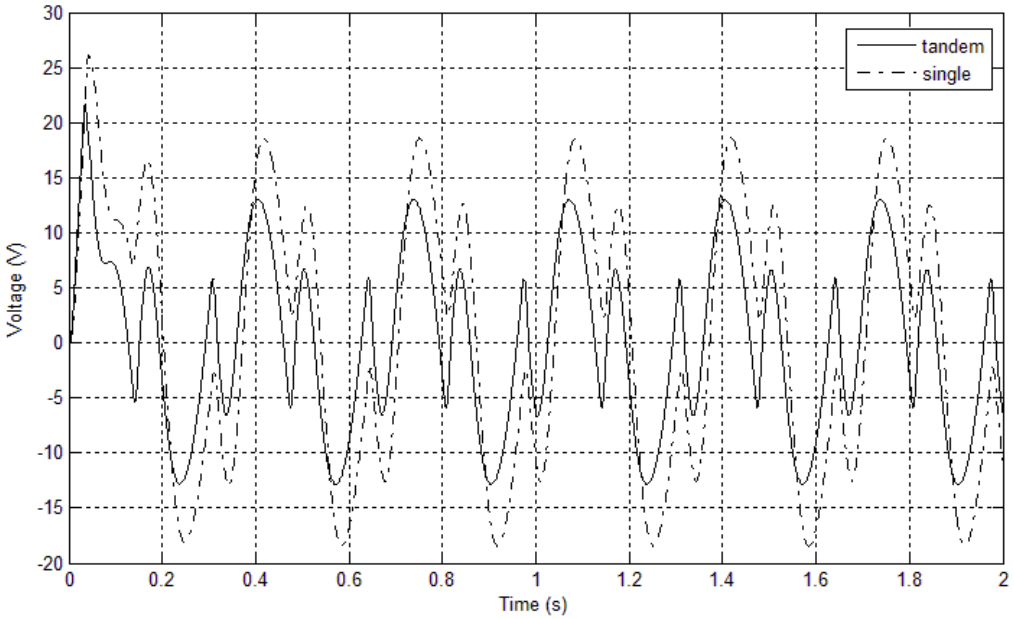

Figure 5-55: Voltage to the motor when MEHA is operating in tandem and singularly against the load

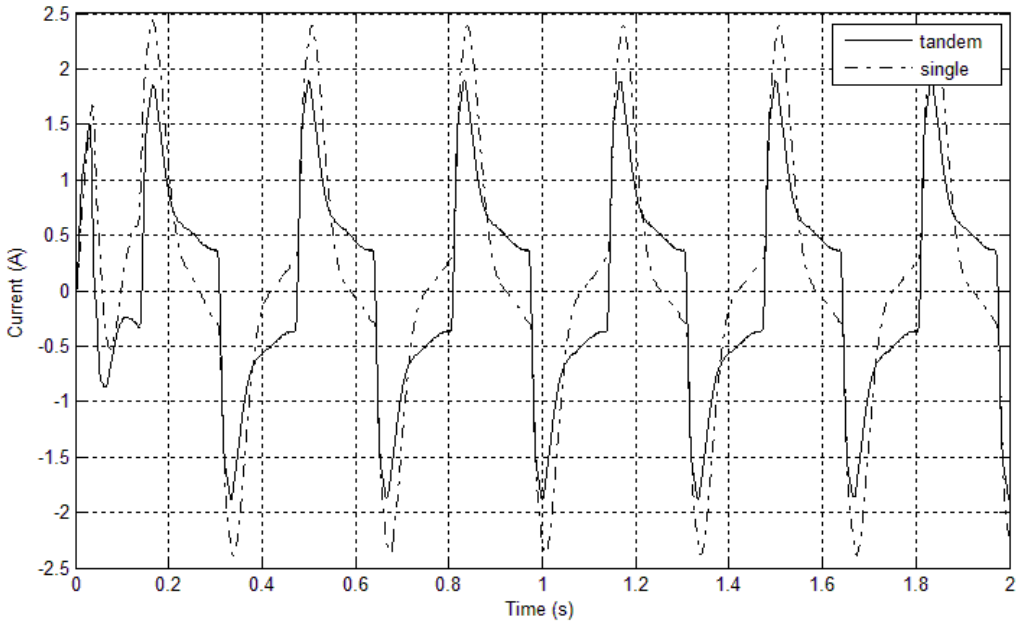

Figure 5-56: Current consumed by the motor when the MEHA is operating in tandem and singularly against the load

In the worst case when the single MEHA has to operate against the load while subjected to the additional load from another MEHA in damped mode, the voltage and current consumed by the motor is presented in the following figures.

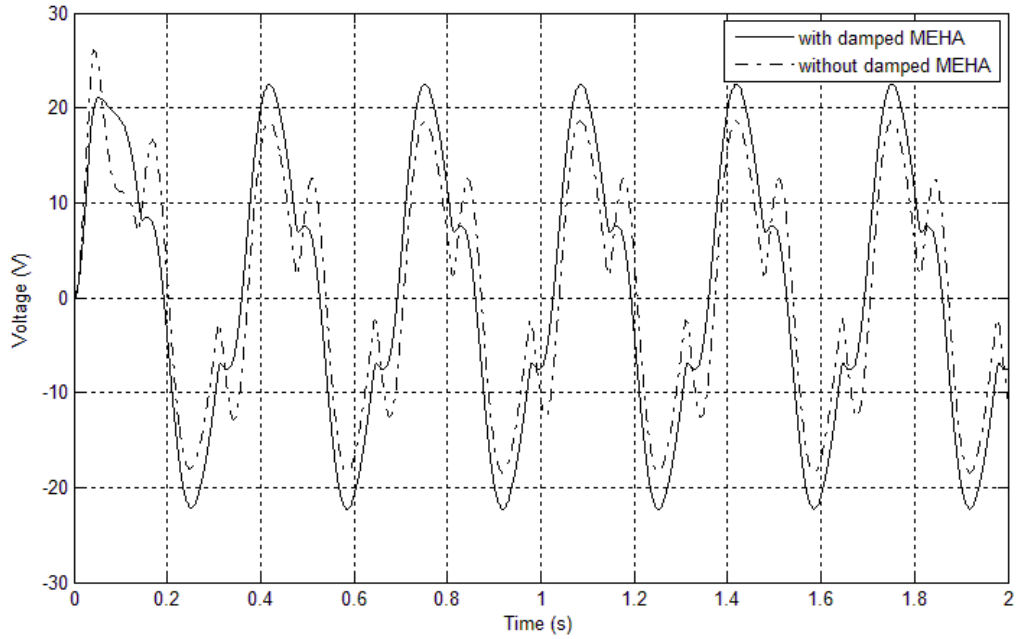

Figure 5-57: Voltage to the motor when the MEHA is acting singularly and with another MEHA in damped mode

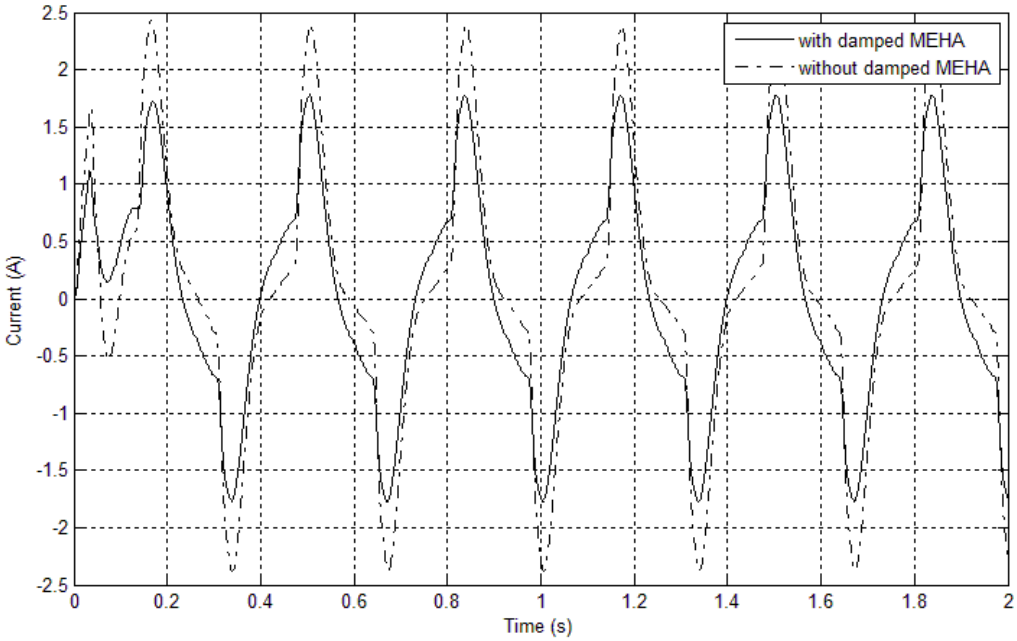

Figure 5-58: Current consumed by the motor of a MEHA acting singularly and with another MEHA in damped mode

While it was expected that the voltage to the motor will decrease and the current consumption will increase with the additional friction from the damped MEHA as was seen in Figure 5-50 and Figure 5-51, the combined effects of the damped MEHA's closed hydrostatic circuit has an opposite effect on the voltage and current consumption on the motor of the active driving MEHA as shown in Figure 5-57 and 5-58. The output and input pistons are isolated from each other with the opening of the bypass valve in the damped MEHA, thus only the friction of the output piston is relevant to the dynamic simulation and the friction of the damped MEHA is reduced. Combined with the greater flow resistance in the damped MEHA as the flow in its closed hydrostatic circuit has to go through the longer bypass channel, friction is a less dominant factor for the damped MEHA.

In order to verify the validity of the model developed in this work, the MEHA's response to a step command is predicted using the non-linear dynamic model and compared with the experimental results obtained from the prototype in Section 6.2. Due to the limits of the

test setup as explained in Section 6.1, the motion of the MEHA prototype has to be monitored at the motor shaft through its integral encoder. The step response of the MEHA prototype predicted by the non-linear dynamic model is plotted in Figure 5-59, while the current consumption of the motor is plotted in Figure 5-60.

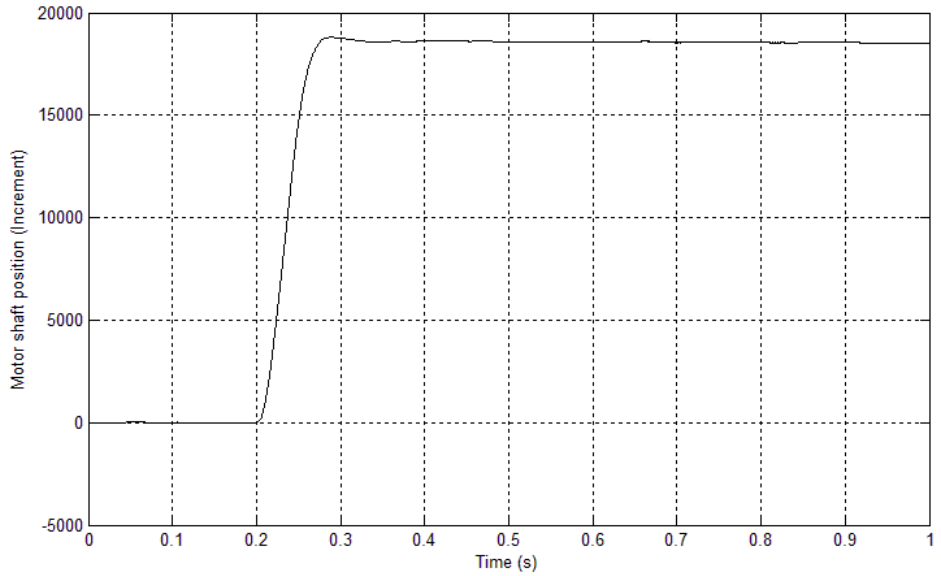

Figure 5-59: Plot of motor shaft position in step response

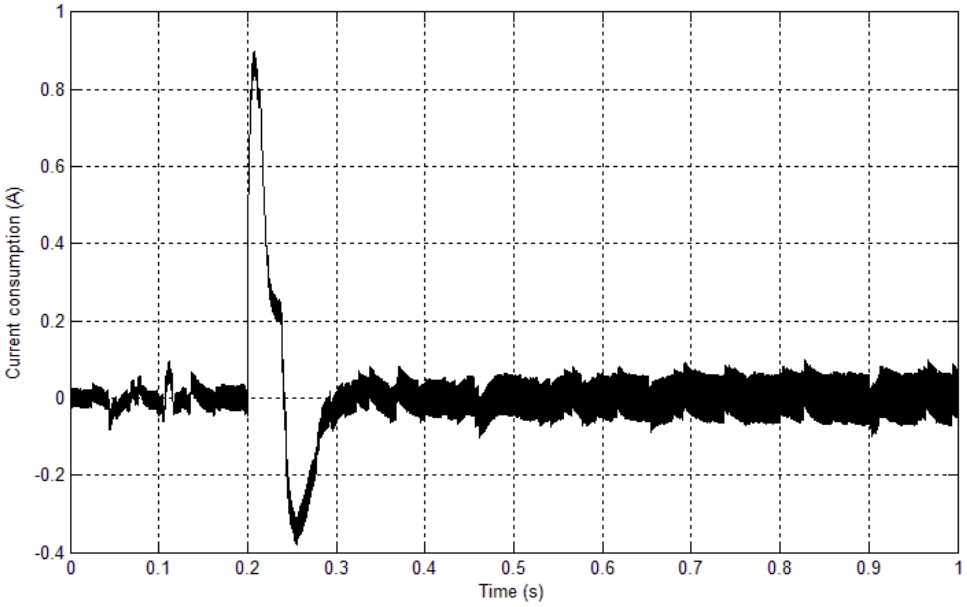

Figure 5-60: Motor current consumption in step response

In this section, the different non-linear effects of the MEHA were investigated with the models developed in Section 3.12 and the dominant factors affecting the current and voltage draw at the motor were determined. For this work, the models validated the design of the prototype. It should be noted that the performance of the MEHA in the worst case active-damped mode was achieved with lower current and voltage limits of 1.8A and 28V respectively, compared to the benchmark's limit of 4.5A and 32V. This analysis highlights the importance of the ability of the MEHA to decouple the EMA. As the EMA can be decoupled from the output in the event of a failure, it does not become a load on the remaining active MEHA. This is vital since the remaining active motor will have to drive two times its own inertia if the failed motor was not decoupled, drastically reducing its dynamic performance in active-damped mode. The mass inertia and friction of the damped MEHA's output piston as well as the flow of its hydraulic fluid through its bypass channel have a manageable impact on the remaining operational MEHA's dynamic performance when in active-damped mode. This characteristic of the MEHA allows for the implementation of multiple redundancies without severely compromising dynamic performance. This sets it apart from current state-of-the-art EMAs which have to contend with severe compromises on their dynamic performance and are limited to only dual redundancy. Lastly, the value of the models developed in this work as a tool to determine the effects of design changes for faster and more effective design iterations in future implementations of the MEHA was also shown.

5.6 Accuracy and stiffness analysis

In this section, the impact of the MEHA's closed hydrostatic circuit on the accuracy and stiffness of the MEHA is studied. In conventional EMAs, the accuracy and stiffness of the

actuator is determined by the tolerances of the mating parts and the stiffness of its components. For the MEHA, the stiffness of the hydraulic fluid in the closed hydrostatic circuit will reduce the overall accuracy and stiffness of the actuator on top of the contributions from the gear train and ballscrew.

In Section 4.9, the total volume of fluid, $\mathrm{V_o}$ within the closed hydrostatic circuit was calculated in Equations 4-15 and 4-16. Adapting from Equation 3-54, the change in volume, $\Delta \mathrm{V}$ due to an increase in pressure on one side of the output piston to that found in Equation 4-8 within the closed hydrostatic circuit can be found from

$$\Delta \mathrm{V} = \frac{\mathrm{P_{A,max}}}{\mathrm{B_o}} \mathrm{V_o} = 1.62 \times 10^{-\mathbf{8}} \mathrm{m}^3 \qquad 5\text{-}7$$

This translates into a stiffness of $0.9°$ or accuracy of $\pm 0.45°$ at the MEHA's output that is within the benchmark laid out in Table 2-2.

6. EXPERIMENTAL INVESTIGATION OF THE MEHA

This chapter reports the experimental investigation of the Miniature Electro-Hydrostatic Actuator (MEHA) prototype. The objectives of the investigation are to determine the:

1. Friction of the input pistons
2. Combined friction of the input and output pistons
3. Maximum output speed of the MEHA prototype
4. Leakage within the closed hydrostatic circuit
5. Maximum deflection of the MEHA prototype
6. Step response of the MEHA prototype

Section 6.1 will first describe the experimental setup and procedures. Section 6.2 will discuss and analyse the results obtained. Lastly, conclusions from the experiments are drawn in Section 6.3.

6.1 Experimental setup and procedure

The experimental setup consists of the following:

- MEHA prototype
- MEHA test assembly
- MEHA input casing samples
- Faulhaber 2232BX4 CSD brushless motor with integral controller
- Computer with Faulhaber Motion Manager user-interface
- Calibrated Vernier calipers
- Hyspin 32 hydraulic mineral oil
- Tenma power supply

Beginning with the tests to determine friction for the input pistons of the MEHA, three versions of the input casing were fabricated from aluminium and stainless steel, with one of the aluminium samples fabricated with bores of larger diameter to accommodate the bronze and PEEK inserts. The friction on individual piston is tested by placing weights on a single piston within a bore on the casing with the hydraulic fluid as lubrication and gradually increasing the weights till the piston begins to slide within the bore (Figure 6-1). This simple test provides an initial estimate of the friction on the input piston.

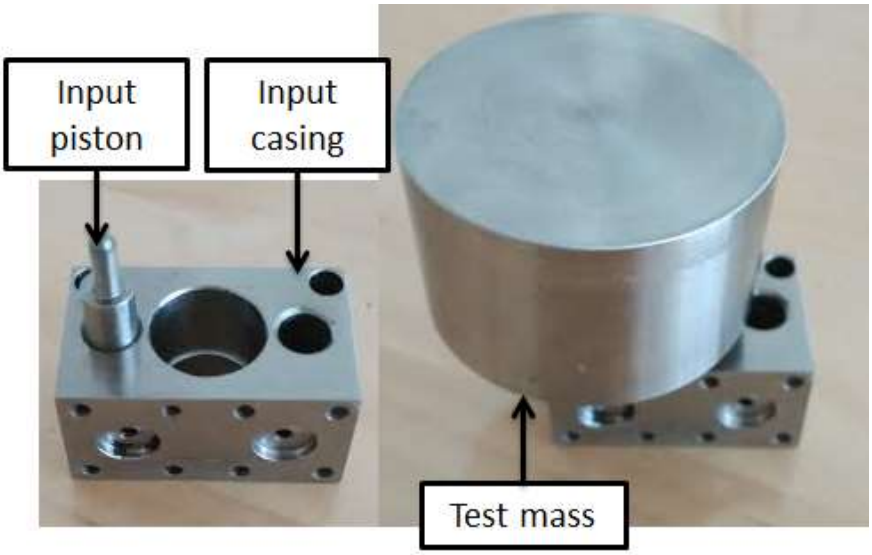

Figure 6-1: Input piston friction test setup

Next, the input assembly is assembled and held in a vice to form a rigid base for the test of the ballscrew and input pistons (Figure 6-2). The input piston and casing has to be coated with hydraulic oil to reproduce the surface lubrication between the seals on the input piston and the surface of the bores of the input casing. The electric motor fastened to the input assembly is commanded via the user interface to actuate the gear train and ballscrew at different speeds. The current consumption at the motor is then monitored at the user interface. Average values of the peak and steady current consumption are obtained and converted to determine the static and kinetic friction force respectively.

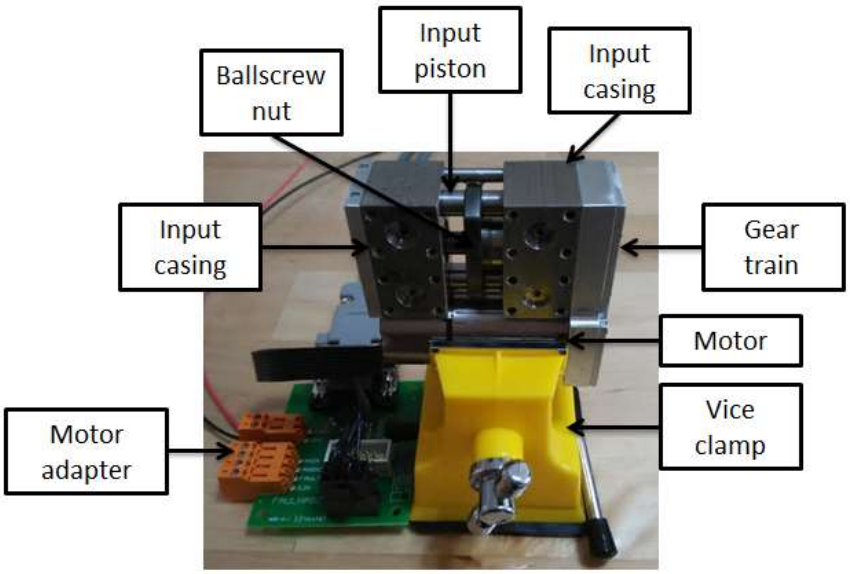

Figure 6-2: Input assembly test setup

In order to test for the combined effect of the friction in the input and output pistons of the MEHA, the MEHA assembly with stainless steel input casings is assembled and held in a vice before the electric motor is commanded via the user interface to actuate the gear train and ballscrew at different speeds (Figure 6-3). In this test, a stainless steel output casing and an aluminium casing with bronze insert are considered. The average values of the peak and steady current consumption are again obtained and converted to determine the static and kinetic friction force. The results from the first test can be subtracted from the results of this test to obtain the friction on the output piston.

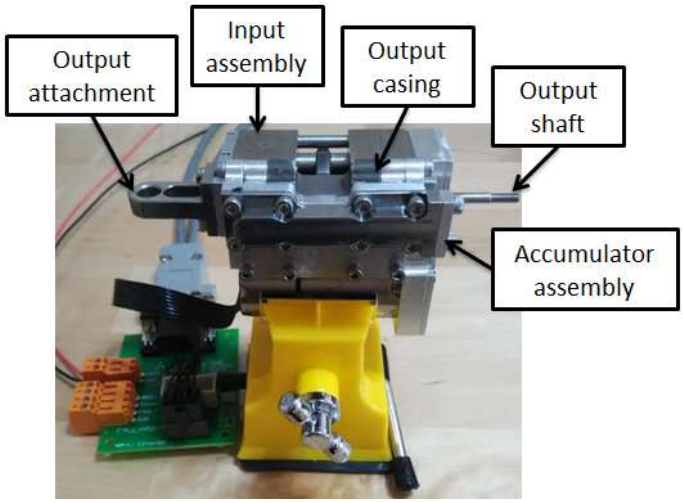

Figure 6-3: MEHA test setup

Continuing with the same test setup, the MEHA can be tested to obtain its maximum speed. Commanding the motor via the user interface to position the pistons to one end of their travel stroke, the motor is then commanded to its maximum speed before it comes to a stop at the other end of the stroke. During this time, the motion of the motor can be monitored via the user-interface. The time interval between when the motor rotation starts till when it stops will then be the time that the MEHA's output piston takes to travel between both ends of its stroke. The average speed of the output piston can then be computed by dividing the total distance travelled by the time between when the motor starts and stops. The test is repeated three times and the average is multiplied by two to obtain the maximum speed of the MEHA.

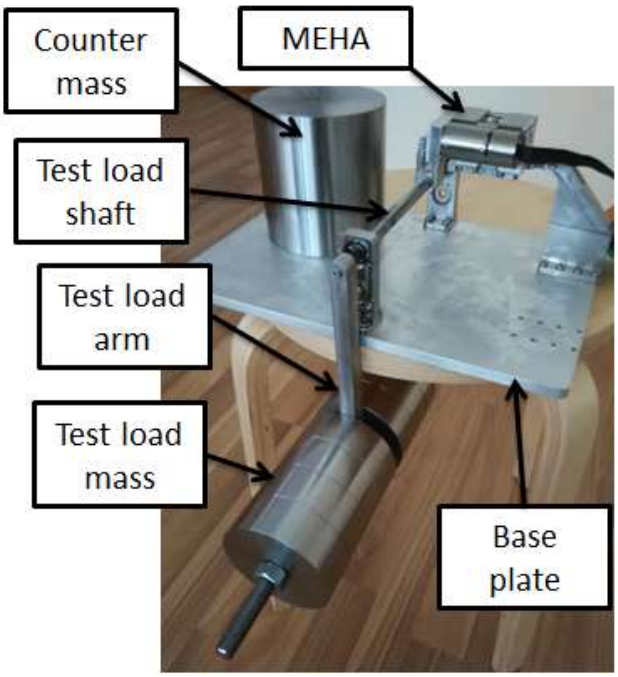

Figure 6-4: MEHA test assembly

The MEHA assembly is then mounted onto the test assembly (Figure 6-4). At the user-interface, the motor is commanded to rotate the MEHA output at the test assembly till it is at the maximum deflection angle achievable with the test load attached. The force on the MEHA output piston corresponding to the deflection angle can then be calculated. From the

motor's user-interface, the current consumption when the MEHA is at the maximum deflection angle can be obtained.

Continuing with the test to determine the leakage within the MEHA, the motor is commanded at the user-interface to rotate the MEHA output to different deflection angles with the test load attached. This varies the pressure across the output piston, which can be derived from the deflection angle of the MEHA. Each deflection angle is held for a period of one hour and the change in position of the MEHA's output piston is measured with the Vernier calipers. The change in the piston's position over this test interval can then be used to determine the leakage rate across the MEHA. The average pressure over this test interval is derived from the pressure corresponding to the deflection angle of the output arm at the start and end of the test interval.

Lastly, using the test setup in Figure 6-3, the step response of the MEHA is studied. As there is no encoder mounted on the output of the MEHA, the position of the MEHA is monitored through the encoder integral to the motor, which has a resolution of 3000 increments per motor revolution. With the designed total reduction ratio of 110 and the maximum deflection of the UAV control surface at 20°, the step command to the motor is set at 18333 increments. Through the user-interface, the motor current consumption is recorded.

6.2 Results & discussion

The results from the initial input piston friction test in Table 6-1 reveal very low friction with the stainless steel casing as well as for the aluminium casing with inserts. It is only possible to determine the static friction with this simple test but an aluminium-only casing can be ruled out as a candidate for the input casing given its relatively high friction.

Table 6-1: Friction on input pistons due to different casing materials

Input casing material	Static friction (N)
Aluminium	14.3
Aluminium with bronze insert	2.5
Aluminium with PEEK insert	4.8
Stainless steel	3.5

The data for the peak and steady current consumption of the motor during the input piston friction test with the aluminium input casing and bronze insert are presented in Table 6-2 and Figure 6-5, while a plot of the current consumption for the 2000rpm case is shown in Figure 6-6. From these data, it can be seen that the peak and steady friction force are almost constant except for when at very low speeds of below 300rpm. The MEHA is unlikely to operate at such low speeds for extended periods of time and the data at these low speeds do not differ much from the average values at higher speeds, thus the average values above 300rpm can be used as inputs for the non-linear dynamic model in Section 5.5. The average peak and steady current consumption above 300rpm is 0.5A and 0.38A respectively. This can be translated to the friction force as seen at the ballscrew nut by

$$\text{Peak friction force} = 0.5\text{A} \times \text{K}_\text{t} \frac{\text{N}_\text{b}}{\text{N}_\text{e}} \frac{2\pi}{\text{L}} = 196.9\text{N} \quad 6\text{-}1$$

$$\text{Steady friction force} = 0.38\text{A} \times \text{K}_\text{t} \frac{\text{N}_\text{b}}{\text{N}_\text{e}} \frac{2\pi}{\text{L}} = 150.6\text{N} \quad 6\text{-}2$$

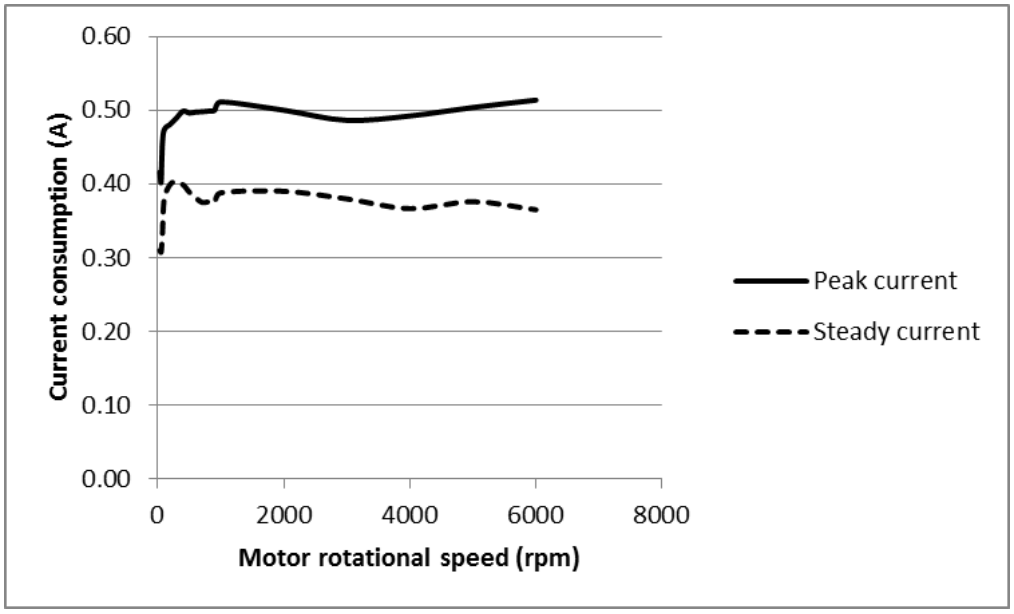

Figure 6-5: Plot of data from input piston friction test with aluminium input casing and bronze insert

Table 6-2: Data from input piston friction test with aluminium input casing and bronze insert

Motor rotational speed (rpm)	Peak current consumption (A)	Steady current consumption (A)
30	0.42	0.31
50	0.40	0.31
70	0.45	0.33
100	0.47	0.38
200	0.48	0.40
300	0.49	0.40
400	0.50	0.40
500	0.50	0.39
600	0.50	0.38
700	0.50	0.38
800	0.50	0.38
900	0.50	0.38
1000	0.51	0.39
2000	0.50	0.39
3000	0.49	0.38
4000	0.49	0.37
5000	0.50	0.38
6000	0.51	0.37

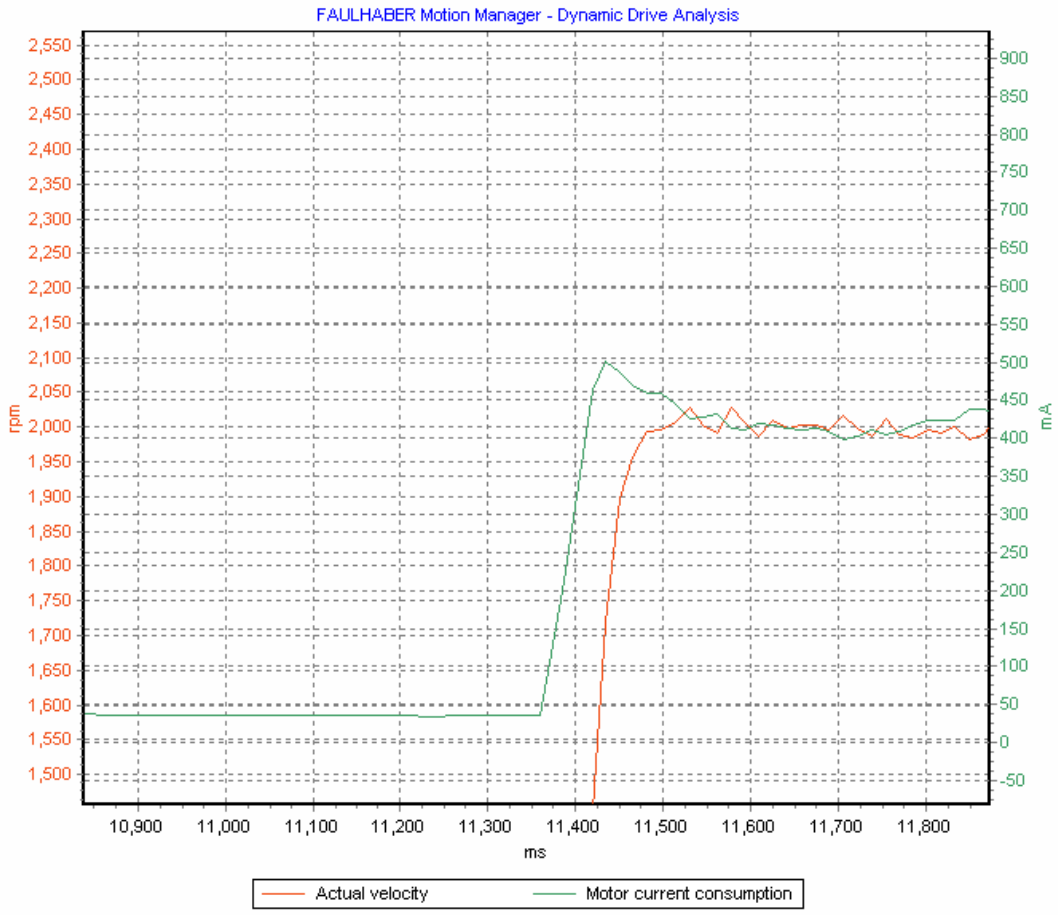

Figure 6-6: Plot of motor current consumption from user-interface at 2000rpm

This test was repeated for the stainless steel casing and the results are summarised in Table 6-3. From the test results, it can be clearly seen that there is a very substantial difference between the predicted values from the initial test results in Table 6-1 and the values obtained in this test. This can be attributed to slight misalignment due to tolerance of the input pistons and casing which results in a net moment about each piston that causes contact with the bore surface, heightening the friction between casing and piston. For the bronze insert, misalignment is a greater issue since there is an additional clearance between the casing and the insert. For the stainless steel casing, the hardness of the material allows the surfaces to be grounded to tighter tolerances, reducing the misalignment and the additional friction.

Table 6-3: Input assembly test

Casing	Predicted	Static	Kinetic
Aluminium with bronze insert	10	196.9	150.6
Stainless steel	14	142	118

Proceeding on with the test for the combined input and output friction, the test data for the steel output casing is presented in Table 6-4 and Figure 6-7. Similar to the results of the input piston friction test, average values of the peak and steady current consumption at the motor can be obtained to derive the combined static and kinetic friction of the input and output pistons

$$\text{Combined peak friction force} = 0.4\text{A} \times \text{K}_\text{t} \frac{\text{N}_\text{b}}{\text{N}_\text{e}} \frac{2\pi}{\text{L}} = 158\text{N} \quad 6\text{-}3$$

$$\text{Combined steady friction force} = 0.33\text{A} \times \text{K}_\text{t} \frac{\text{N}_\text{b}}{\text{N}_\text{e}} \frac{2\pi}{\text{L}} = 130\text{N} \quad 6\text{-}4$$

Table 6-4: Data from combined input and output pistons friction test

Motor rotational speed (rpm)	Peak current consumption (A)	Steady current consumption (A)
30	0.35	0.25
50	0.31	0.23
70	0.3	0.26
100	0.35	0.3
200	0.36	0.33
300	0.4	0.35
400	0.4	0.34
500	0.4	0.33
600	0.39	0.33
700	0.4	0.32
800	0.41	0.33
900	0.4	0.33
1000	0.39	0.34
2000	0.39	0.33
3000	0.4	0.32
4000	0.39	0.33
5000	0.39	0.33
6000	0.4	0.33

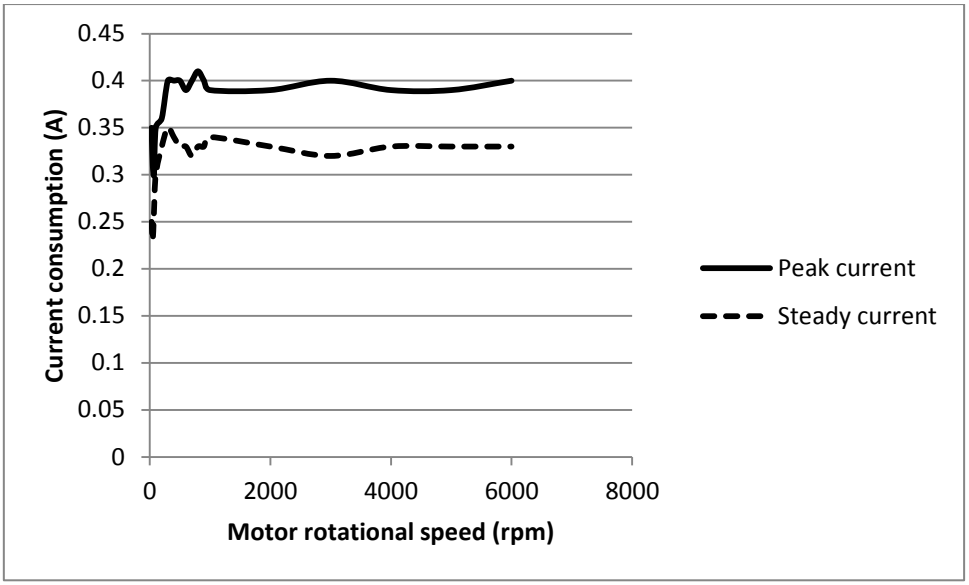

Figure 6-7: Plot of data from combined input and output pistons friction test

During testing, the aluminium casing with the bronze insert could not be tested as hydraulic fluid was leaking across the output piston between the insert and the aluminium casing. This reveals a practical flaw that rules out the aluminium casing with bronze insert as a feasible option. In order to obtain the friction on the output piston separately, the values for input piston friction in steel input casing from Table 6-3 are subtracted from the values for combined friction obtained in the previous equations

$$\text{Output piston peak friction force} = 158 - 142 = 16\text{N} \qquad 6\text{-}5$$

$$\text{Output piston steady friction force} = 130 - 118 = 12\text{N} \qquad 6\text{-}6$$

The lower friction from the output piston is a result of the absence of misalignment associated with multiple pistons moving in parallel that is the case with the input pistons.

Table 6-5: Average output speed test results

Test	Time (s)	Average velocity (ms^{-1})	Peak velocity (ms^{-1})
1	0.183	0.0923	0.186
2	0.18	0.0944	0.189
3	0.181	0.0939	0.188
Average			0.188

Maximum speed at the MEHA's output was found to be 0.188ms^{-1} (Table 6-5) This is slightly higher than the predicted output speed of 0.179ms^{-1} in Equation 4-12. With the designed lever arm length of 23.35mm, this translates into a rotational speed of 461°/s at the output, above the predicted 439°/s. This can be attributed to the limit on the motor's rotational speed imposed during the analysis in Section 4.7 to keep within the maximum rotational speed of the ballscrew shaft. A similar speed limit was electronically imposed on the motor via the user-interface during testing but the total mass inertia as seen at the motor shaft will result in a slight overshoot in the speed of the motor.

On to the maximum deflection test (Figure 6-9), the motor's current consumption while it is holding the load at the maximum deflection is shown in Figure 6-8. At about 1A, this is slightly below the current that the motor is expected to consume while the MEHA is operating against the maximum design load. The expected current consumption is calculated with the load of 4Nm at maximum deflection as follow

$$\frac{\mathrm{T_{max}}}{\mathrm{N}}\frac{1}{\mathrm{K_t}} = 1.16\mathrm{A} \qquad 6\text{-}7$$

This discrepancy between the predicted and experimental current consumption at maximum load deflection can be explained by the relatively high level of friction at the components of the MEHA's closed hydrostatic circuit, which aid in holding the load and result in less torque output required at the motor.

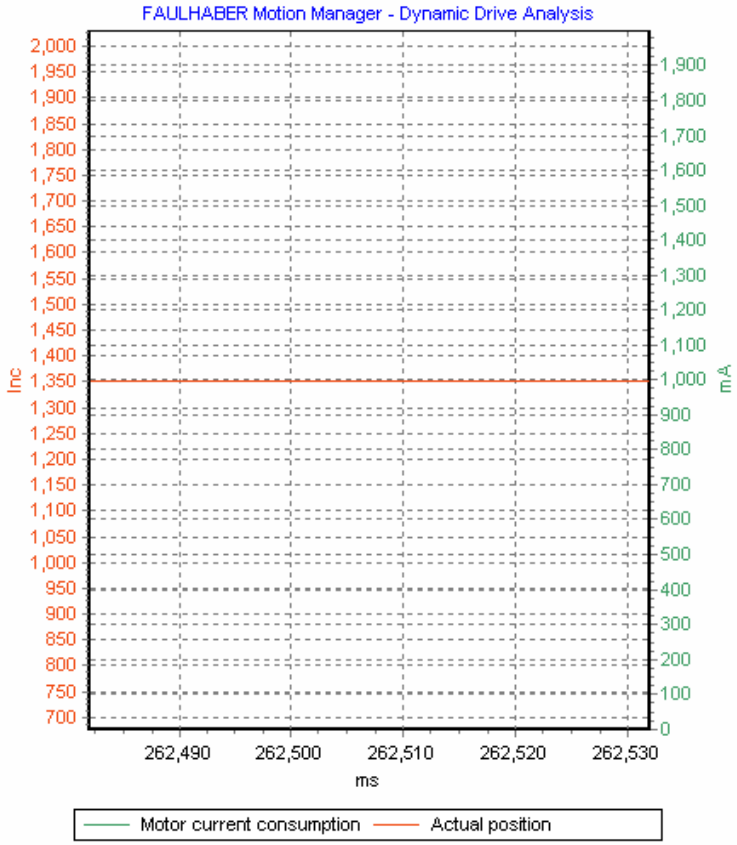

Figure 6-8: Motor current consumption during the maximum deflection test

Figure 6-9: MEHA test assembly load deflection

The calculated leakage rate for different pressure differences across the output piston are listed in Table 6-6, together with the measured output piston movement due to leakage as the load is being held. The average leakage coefficient is used in Section 5.5 to analyse the effect of leakage on the dynamic performance of the MEHA.

Table 6-6: Leakage test results

Pressure difference across output piston (MPa)	Change in linear stroke at MEHA output (mm)	Leakage rate (m^3/s)	Leakage coefficient ($m^3Pa^{-1}s^{-1}$)
2	0.07	4.12e-13	2.06e-19
4	0.13	7.66e-13	1.91e-19
6	0.2	1.18e-12	1.96e-19
8	0.27	1.59e-12	1.99e-19
Average			1.98e-19

The plot of the motor shaft motion during the step response test of the MEHA prototype is shown in Figure 6-10, while Table 6-7 compares the characteristics of the prototype's step response with that predicted by the simulation using the non-linear dynamic model in Section 5.5. The test results with the MEHA prototype show that the characteristics of its response to the step command is close to the prediction of the non-linear dynamic model.

Table 6-7: Comparison between step response of MEHA prototype and non-linear model

	MEHA prototype	Non-linear model
Rise time	50ms	43ms
Overshoot	159 increments	200 increments
Settling time	194ms	140ms

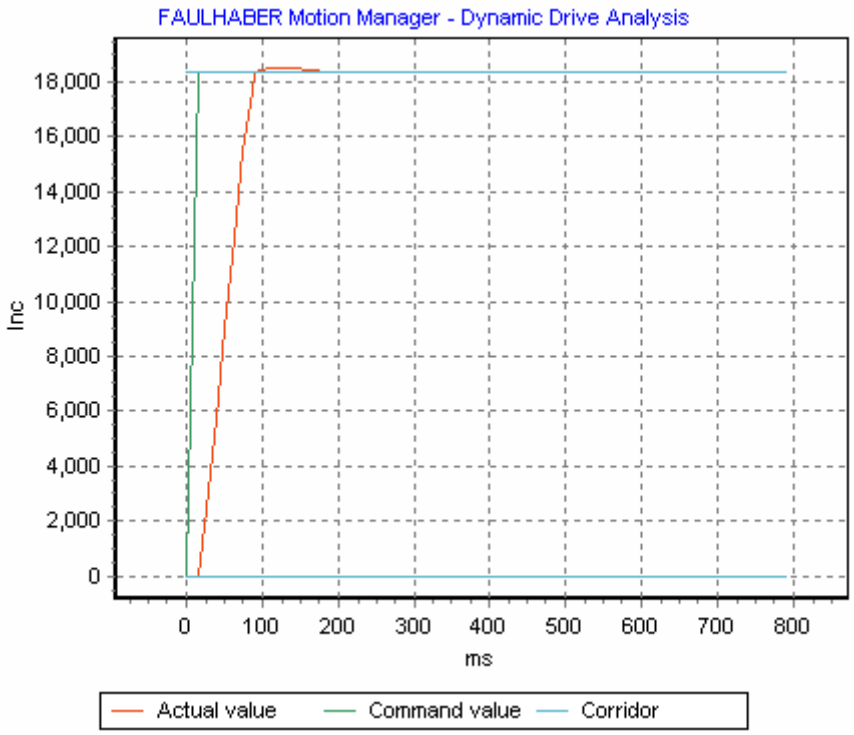

Figure 6-10: Plot of MEHA step response from user-interface

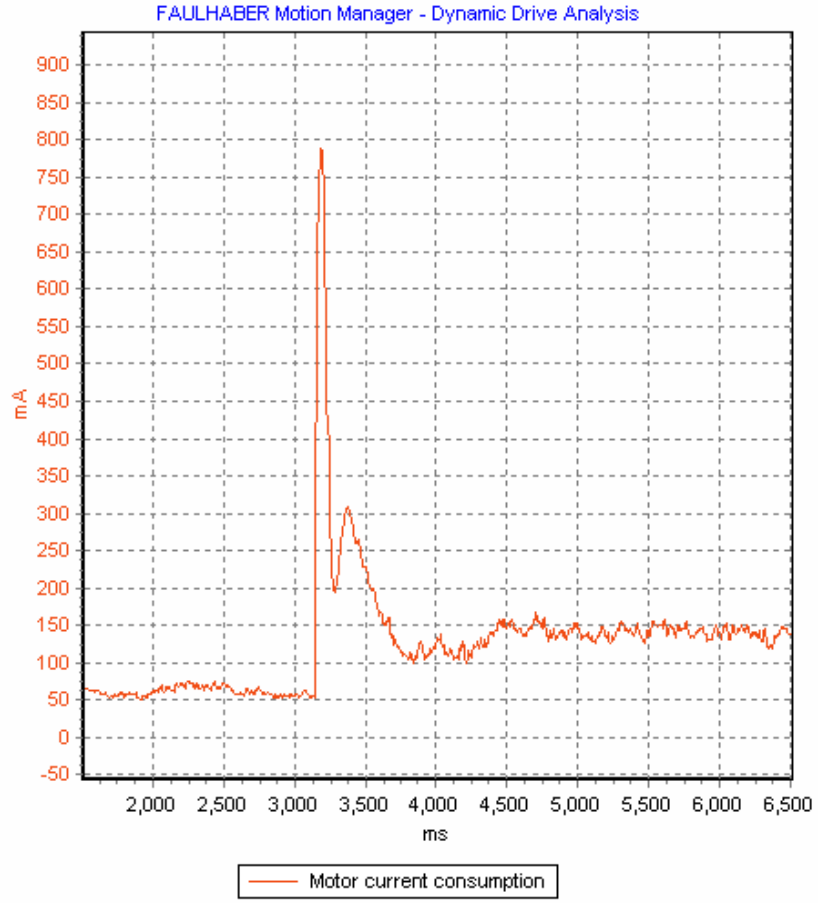

Figure 6-11: Plot of MEHA prototype current consumption during step response test

The motor's peak current consumption during the test with the prototype as shown in Figure 6-11 is slightly lower than the peak consumption predicted by the non-linear model (Figure 5-60). While the deviations of the MEHA's step response predicted from the non-linear model from testing with the prototype are small, they may be attributed to difference in tuning between the controllers in the non-linear model and in the prototype's motor controller.

6.3 Conclusions

In this section, the ability of the MEHA prototype to deflect the design load to the required deflection angle and its maximum speed have been proven. During testing, issues with the alignment of the input pistons led to higher than expected friction. The friction between different alternatives of piston and bore mating materials was compared and quantified, leading to the selection of stainless steel pistons and casings. It was also during testing when it was revealed the alternative with aluminium casing and bronze insert will lead to problems with leakage, ruling it out as a suitable solution. The quantified values for friction are used in Section 5.5 to determine their effects on the dynamic performance of the MEHA. Similarly, leakage coefficients were also quantified with tests in this section and their effects were determined in Section 5.5. The MEHA's step response was then shown to agree well with that predicted from simulation using the non-linear dynamic model in Section 5.5.

Table 6-8: Comparison between MEHA and EMA benchmark

	EMA benchmark	MEHA (active-active mode)
Maximum torque	25Nm	20.8Nm
No-load speed	160°/s	461°/s
Peak power output	17.5W	41.8W
Volume	7.81 X $10^{-4}m^3$ (132.9 X 56 X 104mm)	2X 1.45 X $10^{-4}m^3$ (64 X 40.5 X 56mm)
Power density	22409 W/m^3	143987W/m^3
Mass	875g	2 X 350g

Comparing the MEHA prototype developed in this work with the EMA benchmark in Table 6-8, it can be seen that while the maximum stall torque of the MEHA will be less than the EMA benchmark, its much higher no-load speed means that the MEHA's peak mechanical power delivered to the load will be also much greater. As a result of the optimisation performed in Section 4.2, the full power range of the motor is utilised while ensuring that the MEHA will be able to continue operating even in the worst case. While an actual bypass valve was not developed during the course of this work, the volume used in Table 6-8 takes into account the space reserved for any further implementation of the bypass valve. The compactness of the closed hydrostatic circuit compared to the elaborate gear train and brakes needed for the EMA benchmark accounts for the wide difference in the volume. However, due to the selection of stainless steel for many components of the MEHA, the mass of the MEHA will be close to that of the EMA benchmark. Some of this mass can be reduced by optimising the design of the stainless steel components or by resolving the issues of leakage between the bronze inserts and aluminium casing in future work.

7. Conclusions & Recommendations

A novel Miniature Electro-Hydrostatic Actuator (MEHA) was conceptualised and studied in this work. From the literature review and initial feasibility studies, it was found that the miniaturisation of current pump designs will not be able to yield a MEHA that is competitive against current state-of-the-art dual redundant EMAs. Gear pumps are limited in the pressure that they can deliver due to leakage across the face of the gears and between their gear teeth. The mechanical contact between gear teeth also limits the speed that a gear pump can rotate at. Miniature vane pumps have better pressure capacity than gear pumps due to the contact of the vanes with the pump casing but the wear of the vanes severely limits their maximum rotational speed. Miniature piston pumps have the greatest pressure capacity among current pump technologies but their maximum rotational speed is limited by the rate of wear between the swivel plate and the back of the pistons. With these limitations on current miniature pump technology, an attempt was made to develop miniature pump suitable for MEHA applications.

New miniature hydraulic pump designs were explored. Earlier efforts to realise a novel miniature high speed Axial Vane Pump (AVP) found substantial intractable problems with running friction and leakage. Fluid leakage paths become relatively large compared to the fluid displacement volume of miniature pumps, thus leakage between the ports of such pumps is more significant. At the same time, the small electric motors used in MEHAs produce substantially lower torque, thus the friction between the moving parts in miniature pumps can no longer be assumed to be negligible like in conventional hydraulic pumps. Together with the results of the literature review, it was concluded that miniature pumps cannot be expected to realise MEHAs that are competitive with EMAs as UAV actuators.

A novel MEHA that utilises a closed hydrostatic circuit to decouple the EMA from the output was subsequently conceptualised. This actuator is a new type of actuator that is distinct from the EMA used commonly in UAVs and from the electro-hydraulic and electro-hydrostatic actuators used in manned aircraft. Instead of using a pump to convert hydraulic power from mechanical power of the electric motor like in conventional hydraulic actuators, an efficient EMA has to be used in the MEHA to bypass the limitations of miniaturised pump technology. Distinct from conventional EMAs used in today's UAVs, the MEHA has a closed hydrostatic circuit to transmit power between the EMA and the UAV's control surface.

In order to realise the MEHA concept, the necessary analysis background and design process were developed. A non-linear dynamic model that incorporates non-ideal effects was developed in this work to study the consequences of these effects on the MEHA's dynamic performance, as well the MEHA's ability to perform in active-active and active-damped modes. Working with this model, it was shown that friction will be the single most important factor that affects the performance of the MEHA. These design and analysis processes and tools will be vital to ease future implementations of the MEHA. These were then applied to the prototype of the MEHA developed for this work.

In tests of the MEHA prototype, it was found to be able to deliver the design torque and speed. During tests to quantify the friction in the MEHA, it was discovered that when assembled into the input assembly, the friction of the pistons will be much higher than the simple sum of friction on individual pistons. This was attributed to misalignment due to tolerance between mating parts. The discovery that friction is the most significant factor to the dynamic performance of the MEHA shows the importance of practical testing to determine the friction of the whole assembly. It also highlights the specific parts of the

components where tight tolerance control will be required in any future implementation of the MEHA. Tests with the prototype also validated the non-dynamic model that was developed in this work. Compared with the benchmark used in this work, the MEHA prototype will offer significant improvement in power density and peak power output. However, this comparison also highlighted the need to reduce the mass of the MEHA in further development.

Recommendations for future work:

- Further explore the aluminium casing and bronze insert alternative for the input and output assemblies of the MEHA to reduce the mass of the MEHA
- Design a controller for the MEHA with closed-loop feedback from the UAV control surface's deflection angle and test its dynamic performance
- Conduct environmental testing on the MEHA to show its ability to operate under realistic conditions
- Improve design of input assembly to further reduce friction

BIBLIOGRAPHY

[1] S. C. Jensen, G. D. Jenny, B. Raymond and D. Dawson, “Flight test experience with an electromechanical actuator on the F-18 systems research aircraft,” in *19th Digital Avionics Systems Conference*, Philadelphia, 2000.

[2] E. Raymond and C. Chenoworth, Aircraft Flight Control Actuation System Design, SAE, 1993.

[3] A. Ludovic, “http://www.smartcockpit.com/data/pdfs/plane/boeing/B767/instructor/B767_Hydraulics.pdf,” [Online].

[4] Moog Inc., “System Integrator for Lockheed Martin F-35,” 2010. [Online]. Available: http://www.moog.com/markets/aircraft/military-aircraft/fighter-trainer/system-integrator-for-lockheed-martin-f35/.

[5] OSD, “Unmanned Aerial Vehicle Reliability Study,” Office of the Secretary of Defense, Department of Defense, 2003.

[6] S. Fine, US Navy, 10 February 2013. [Online]. Available: http://www.navy.mil/view_image.asp?id=143855.

[7] Aermech.In, [Online]. Available: http://aermech.in/iai-haropiai-harpy-2-attack-ucavdroneindian-army/.

[8] H. Wagner, G. Nikolov, A. Bierig and H. Spangenberg, “More-electric aircraft are not without challenges,” 8 Oct 2012. [Online]. Available: http://articles.sae.org/11465/. [Accessed August 2015].

[9] P. Wheeler and S. Bozhko, “The more electric aircraft: Technology and challenges,” *Electrification Magazine,* vol. 2, no. 4, December 2014.

[10] Y. He, J. Zhu, X. Yuan and Z. Huang, “Research on high-reliabile dual-redundancy electro-mechanical actuator controller,” in *Proceeding of the 11th World Congress on Intelligent Control and Automation*, Shenyang, China, 2014.

[11] J. Hemanth, S. R. Anas, G. Anish and M. S. P. Subathra, “A dual redundancy technique for electromechanical actuation system applied to launch vehicles,” in *Proceedings of ICETECT*, Tamil Nadu, 2011.

[12] J. Kudva, “Overview of the DARPA/AFRL/NASA Smart wing program,” in *SPIE Conference on Industrial and Commercial Applications of Smart Structures Technologies*, Newport Beach, California , 1999.

[13] P. Janker, “New actuators for aircraft and space applications,” *Actuator 2008, 11th International Conference on New Actuators, Bremen, Germany, 9-11 June,* 2008.

[14] D. P. Wang, J. D. Bartley-Cho, C. A. Martin and B. J. Hallam, “Development of high-rate, large deflection, hingeless trailing edge control surface for the smart wing wind tunnel model,” *Smart Structures and Materials 2001: Industrial and Commercial Applications of Smart Structures,* vol. 4332, 2001.

[15] R. Barrett, “Missile flight control using active flexspar actuators,” *Smart Material Structures,* vol. 5, pp. 121-128, 1996.

[16] R. Barrett, “Design, development and testing of a transonic missile fin employing PBP/DEAS actuators,” in *Industrial and Commercial Applications of Smart Structures Technologies*, 2008.

[17] D. v. d. Bossche, “The A380 flight control electrohydrostatic actuators, achievements and lessons learnt,” in *25th International Congress of the Aeronautical Sciences*, 2006.

[18] R. Navarro, “Performance of an electro-hydrostatic actuator on the F-18 systems research aircraft,” National Aeronautics and Space Administration, Dryden Flight Research Center, 1997.

[19] M. A. Davis, “High performance electromechanical servoactuation using brushless DC motors,” Moog Inc. , 1984.

[20] K. Kang, M. Pachter, C. Houpis and S. Rasmussen, “Modelling and control of an electrohydrostatic actuator,” in *Aerospace and Electronics Conference, 1995. NAECON 1995., Proceedings of the IEEE 1995 National*, 1994.

[21] B. Liu, J. Zhang, H. Jia and W. Ge, “Design and analysis of power system of micro-electromechanical actuator,” in *Industrial Mechatronics and Automation (ICIMA), 2010 2nd International Conference on*, 2010.

[22] G. L. Fleeman, Tactical Missile Design, AIAA, 2006.

[23] T. B. Bullock, “Servo basics for the layman,” June 1991. [Online]. Available: http://support.ctc-control.com/customer/elearning/registered/servoBasicsForTheLayman.pdf. [Accessed August 2015].

[24] M. V. Cook, Flight dynamics principles: A linear systems approach to aircraft stability and control, Elsevier Ltd, 2013.

[25] M. B. Tischler, “System identification methods for aircraft flight control development and validation,” NASA Ames Research Center, 1995.

[26] J. A. Franklin, M. W. Stortz, S. A. Engelland, G. H. Hardy and J. L. Martin, “Moving base simulation evaluation of control system concepts and design criteria for STOVL aircraft,” NASA, 1991.

[27] B. Mettler, Identification Modelling and Characteristics of Miniature Rotorcraft, Springer US, 2003.

[28] Autodesk Inc., [Online]. Available: http://www.instructables.com/id/Planetary-Gear/.

[29] SDP/SI, “Elements of Metric Gear Technology,” Stock Drive Products / Sterling Instrument, 2012.

[30] X.-h. Zhang, “A Research and Design of Entire Dual Redundancy Electro-Mechanical Actuator,” *Micromotors Servo Technique,* no. 2, 2006.

[31] W. J. Norton, “Advanced ElectroMechanical Actautor System (EMAS) flight test,”

Airforce Force Wright Aeronautical Systems Division, Ohio, 1986.

[32] J. M. Miller, “Hybrid electric vehicle propulsion system architectures of the e-CVT type,” *IEEE Transactions on Power Electronics ,* vol. 21, no. 3, pp. 756-767, 2006.

[33] J. Weiss, “Control actuator reliability and redundancy for long duration underwater vehicle missions with high value payloads,” in *Underwater Intervention 2014*, 2014.

[34] Muirhead Aerospace, “Actuators,” Ametek Aerospace & Defense, 2012. [Online]. Available: http://www.muirheadaerospace.com/motion-technology/actuators.html#SIngleActuator. [Accessed 2015].

[35] J. W. Bennett, B. C. Mecrow, D. J. Atkinson and G. J. Atkinson, “Safety-critical design of electromechanical actuation systems in commercial aircraft,” *IET Electric Power Applications,* vol. 5, no. 1, pp. 37-47, 2011.

[36] G. L. Nino, “"Hermes 450",” US Customs and Border Protection, [Online]. Available: http://www.cbp.gov/xp/cgov/newsroom/photo_gallery/archives/2004_newsphotos/0625_2.xm.

[37] MTC Industries, “ERSA-0311 Redundant Electrical Rotary Servo Actuator,” MTC Industries & Research Carmiel Ltd., 2012.

[38] J. T. Arters, “Preliminary design of piezo-actuated composite sandwich fins for projectile maneuverability,” *46th AIAA/ASME/ASCE/AHS/ASC Structures, Structural Dynamics & Materials Conference, 18-21 April, Austin, Texas,* 2005.

[39] D. P.Wang, “Development of high-rate, large deflection, hingeless trailing edge control surface for the Smart Wing wind tunnel model,” *Smart Structures and Materials 2001: Industrial and Commercial Applications of Smart Structures,* 2001.

[40] A. J. Schonecker, “Overview on Macro Fiber Composite applications,” in *Smart Structures and Materials: Active Materials: Behaviour and Mechanics*, 2006.

[41] M. Tryson, “Dielectric electro active polymers: Development of an industry,” in *Electroactive Polymer Actuators and Devices (EAPAD)* , 2010.

[42] A. Seow, “Shape memory alloy as actuator to deflect a wing flap,” in *16th AIAA/ASME/AHS Adaptive Structures Conference*, Schaumburg, IL, USA, 2008.

[43] Woodward, “Flight Controls Primary,” [Online]. Available: http://www.woodward.com/PrimaryFlightControls.aspx.

[44] J. Dopper, M. Clemens, W. Ehrfeld, S. Jung, K.-P. Kamper and H. Lehr, “Micro gear pumps for dosing of viscous fluids,” *J. Micromech. Microeng. ,* no. 7, pp. 230-232, 1997.

[45] A. Waldschik and S. Buttgenbach, “Micro gear pump with internal electromagnetic drive,” *Microsystem Technology,* no. 16, pp. 1581-1587, 1998.

[46] K. Deng, A. Dewa, D. Ritter, C. Bonham and H. Guckel, “Characterisation of gear pumps fabricated by LIGA,” *Microsystem Technologies,* no. 4, pp. 163-167, 1998.

[47] K. Nagamura, K. Ikejo and F. Tutulan, “Design and performance of gear pumps with a non-involute tooth profile,” *Proceedings of the Institution of Mechanical Engineers, Part*

B: Journal of Engineering Manufacture, vol. 218, 2004.

[48] H. Yanada, T. Ichikawa and Y. Itsuji, "Study of the trapping of fluid in a gear pump," *Proceedings of the Institution of Mechanical Engineers, Part A: Journal of Power and Energy,* vol. 201, 1987.

[49] N. D. Manring and S. B. Kasaragadda, "The theoretical flow ripple of an external gear pump," *Journal of Dynamic Systems, Measurement, and Control,* vol. 125, Sept 2003.

[50] K. J. Huang and W. C. Lian, "Kinematic flowrate characteristics of external spur gear pumps using an exact closed solution," *Mechanism and Machine Theory,* vol. 44, pp. 1121-1131, 2009.

[51] SDP/SI, "Technical Section," in *Handbook of Metric Drive Components*, SDP/SI, 2003.

[52] IDEX Corporation, "Micropump," 2015. [Online]. Available: http://www.micropump.com/default.aspx. [Accessed August 2015].

[53] NPTEL, [Online]. Available: nptel.ac.in/courses/112103174/module5/lec3/2.html.

[54] J. Watton, Fundamentals of fluid power, Cambridge University Press, 2006.

[55] Nachi-Fujikoshi Corp, "Nachi-Fujikoshi Corp," 2015. [Online]. Available: http://www.nachi-fujikoshi.co.jp/eng/web/h1000e/. [Accessed August 2015].

[56] D. Thomas, J. Dechow and R. Catterson, "30000rpm vane pump demonstration," Air Force Aero Propulsion Laboratory, Ohio, 1972.

[57] Design Aerospace LLC, “Pump, Hydraulic - Description,” [Online]. Available: http://www.daerospace.com/HydraulicSystems/PumpDesc.php.

[58] N. D. Manring and F. A. Damtew, “The control torque on the swash plate of an axial-piston utilising piston-bore springs,” *Journal of Dynamic Systems, Measurement and Control,* vol. 123, p. 471, 2001.

[59] Takako America Co., Inc, “Small Axial Piston Pump,” 2015. [Online]. Available: www.takako-us.com/. [Accessed August 2015].

[60] F. M. White, Fluid Mechanics, McGraw-Hill, 2003.

[61] R. Kang, Z. Jia, S. Wu and J.-C. Mare, “The nonlinear accuracy model of Electro-Hydrostatic Actuator,” in *Robotics, Automation and Mechatronics, 2008 IEEE Conference on*, Chengdu, 2008.

[62] M. G. Park, S. H. Park, J. S. Kim and H. G. Lee, “Modelling and control and Electro Hydrostatic Actuator Systems,” in *ICROS-SICE International Joint Conference 2009*, Fukuoka, 2009.

[63] E. Bilgen and R. Boulos, “Functional Dependence of Torque Coefficient of Coaxial Cylinders on Gap Width and Reynolds Numbers,” *Journal of Fluids Engineering,* pp. 122-126, March 1973.

[64] Solvay, “Torlon PAI Design Guide,” Solvay Specialty Polymers, Italy, 2014.

[65] Faulhaber Minimotor SA, “Faulhaber,” Faulhaber Minimotor SA, August 2015. [Online].

Available: http://www.faulhaber.com/en/global/. [Accessed August 2015].

[66] Steinmeyer GmbH & Co. KG, “Maximum Speed,” August 2015. [Online]. Available: http://www2.steinmeyer.com/content/cnt_cnt/docid_962/iso_en. [Accessed August 2015].

[67] B. Shangguan, Y. Z. Zhang, J. D. Xing, L. M. Sun and Y. Chen, “Study of the friction and wear of electrified copper against copper alloy under dry or moist conditions,” *Tribology Transactions,* vol. 53, no. 6, pp. 927-932, 2010.

[68] T. Sakurai, H. Okabe and I. Matsumura, “Wear rate of copper under boundary lubrication,” *ASLE Transactions,* vol. 14, no. 3, pp. 221-225, 1971.

[69] R. H. Perry and D. W. Green, Perry's Chemical Engineers Handbook, McGraw Hill, 1999.

APPENDIX A: DERIVATION FOR REDUCTION RATIO EQUATIONS

At the output piston of the closed hydrostatic circuit, the force due to the pressure difference across the piston produces a torque at the MEHA's output about the lever arm's pivot point.

$$\mathrm{T} = \Delta \mathrm{P} \mathrm{A} l_l \sin\theta \qquad \text{A-1}$$

While at the input piston of the closed hydrostatic circuit, the pressure difference across the piston is transmitted as a load torque on the ballscrew shaft

$$\mathbf{T_b} = \frac{\mathbf{\Delta P A_{ip} L}}{\mathbf{2\pi}} \qquad \text{A-2}$$

At the electric motor, the load torque on the ballscrew is transmitted through the spur gear as a load torque on the electric motor.

$$\mathrm{T_b} = \frac{\mathrm{N_b}}{\mathrm{N_e}} \mathrm{T_e} \qquad \text{A-3}$$

Combining the three equations,

$$\frac{\mathrm{T}}{\mathrm{A} l_l \sin\theta} = \frac{2\pi}{\mathrm{A_{ip} L}} \mathrm{T_b} = \frac{2\pi}{\mathrm{A_{ip} L}} \frac{\mathrm{N_b}}{\mathrm{N_e}} \mathrm{T_e} \qquad \text{A-4}$$

$$\mathrm{T} = 2\pi \frac{\mathrm{A}}{\mathrm{A_{ip}}} \frac{\mathrm{N_b}}{\mathrm{N_e}} \frac{l_l}{\mathrm{L}} \sin\theta \, \mathrm{T_e} \qquad \text{A-5}$$

The total reduction ratio is thus,

$$\mathrm{N} = 2\pi \frac{\mathrm{A}}{\mathrm{A_{ip}}} \frac{\mathrm{N_b}}{\mathrm{N_e}} \frac{l_l}{\mathrm{L}} \sin\theta \qquad \text{A-6}$$

Considering the output piston with original length, $\mathrm{x_o}$ and lever arm with length, l_l in the zero deflection centre position of the UAV's control surface, the angle, ϕ between the lever

arm and the hypotenuse connecting the centre of the output shaft and the furthest rotating point of the output piston can be found as follow.

$$\sin\phi = \frac{x_o}{\sqrt{x_o^2 + l_l^2}} \quad \text{A-7}$$

$$\cos\phi = \frac{l_l}{\sqrt{x_o^2 + l_l^2}} \quad \text{A-8}$$

When the output piston extends by $\Delta x_{extension}$ to deflect the UAV's control surface by the maximum deflection angle, δ_{max}, the extended length of the output piston can be derived from the angle between the deflected lever arm and the same hypotenuse.

$$(x_o + \Delta x_{extension})^2 = l_l^2 + \left(\sqrt{x_o^2 + l_l^2}\right)^2 - 2l_l\sqrt{x_o^2 + l_l^2}\cos(\phi + \delta_{max}) \quad \text{A-9}$$

$$x_o + \Delta x_{extension} = \sqrt{2l_l^2 + x_o^2 - 2l_l^2\cos\delta_{max} + 2l_l x_o \sin\delta_{max}} \quad \text{A-10}$$

The required extension of the output piston can then be found.

$$\Delta x_{extension} = -x_o + \sqrt{2l_l^2 + x_o^2 - 2l_l^2\cos\delta_{max} + 2l_l x_o \sin\delta_{max}} \quad \text{A-11}$$

The angle,$\theta_{extension}$ between the extended output piston's line of action and the deflected lever arm is derived from the output piston's extended length.

$$\frac{x_o + \Delta x_{extension}}{\sin(\phi + \delta_{max})} = \frac{\sqrt{x_o^2 + l_l^2}}{\sin\theta_{extension}} \quad \text{A-12}$$

$$\sin\theta_{extension} = \frac{x_o\cos\delta_{max} + l_l\sin\delta_{max}}{\sqrt{2l_l^2 + x_o^2 - 2l_l^2\cos\delta_{max} + 2l_l x_o\sin\delta_{max}}} \quad \text{A-13}$$

Similarly, when the output piston retracts by $\Delta x_{retraction}$ to deflect the UAV's control surface by the maximum deflection angle, δ_{max}, the retracted length of the output piston can be derived from the angle between the deflected lever arm and the hypotenuse.

$$(x_o - \Delta x_{retraction})^2 = l_l^2 + \left(\sqrt{x_o^2 + l_l^2}\right)^2 - 2l_l\sqrt{x_o^2 + l_l^2}\cos(\phi - \delta_{max}) \quad \text{A-14}$$

$$x_o - \Delta x_{retraction} = \sqrt{2l_l^2 + x_o^2 - 2l_l^2\cos\delta_{max} - 2l_l x_o \sin\delta_{max}} \quad \text{A-15}$$

The required retraction of the output piston can then be found.

$$\Delta x_{retraction} = x_o - \sqrt{2l_l^2 + x_o^2 - 2l_l^2\cos\delta_{max} - 2l_l x_o \sin\delta_{max}} \quad \text{A-16}$$

The angle, $\theta_{retraction}$ between the retracted output piston's line of action and the deflected lever arm is similarly derived from the output piston's retracted length.

$$\frac{x_o - \Delta x_{retraction}}{\sin(\phi - \delta_{max})} = \frac{\sqrt{x_o^2 + l_l^2}}{\sin\theta_{retraction}} \quad \text{A-17}$$

$$\sin\theta_{retraction} = \frac{x_o\cos\delta_{max} - l_l\sin\delta_{max}}{\sqrt{2l_l^2 + x_o^2 - 2l_l^2\cos\delta_{max} - 2l_l x_o\sin\delta_{max}}} \quad \text{A-18}$$